

HOMOGENEOUS LINEWIDTH AND SPECTRAL DIFFUSION
IN SEMICONDUCTOR NANOCRYSTALS

by

SASHA DAWN TAVENNER KRUGER

A DISSERTATION

Presented to the Department of Physics
and the Graduate School of the University of Oregon
in partial fulfillment of the requirements
for the degree of
Doctor of Philosophy

August 2006

“Homogeneous Linewidth and Spectral Diffusion in Semiconductor Nanocrystals,” a dissertation prepared by Sasha Dawn Tavenner Kruger in partial fulfillment of the requirements for the Doctor of Philosophy degree in the Department of Physics. This dissertation has been approved and accepted by:

Dr. Miriam Deutsch, Chair of the Examining Committee

Date

Committee in Charge: Dr. Miriam Deutsch, Chair
 Dr. Hailin Wang
 Dr. Mark Lonergan
 Dr. Heiner Linke
 Dr. Jens Nöckel

Accepted by:

Dean of the Graduate School

© 2006 Sasha Dawn Tavenner Kruger

An Abstract of the Dissertation of
Sasha Dawn Tavenner Kruger for the degree of Doctor of Philosophy
in the Department of Physics to be taken August 2006
Title: HOMOGENEOUS LINEWIDTH AND SPECTRAL DIFFUSION IN
SEMICONDUCTOR NANOCRYSTALS

Approved: _____
Dr. Hailin Wang

Semiconductor nanocrystals a few nanometers in extent exhibit unique electronic and optical properties. These properties depend on the size and dimensionality of the confinement potential. The optical absorption spectrum of nanocrystals generally features a zero-phonon line (ZPL). Its width indicates the coupling of the electron to the electromagnetic vacuum and to phonons. Electron-phonon interactions are one strong source of exciton decoherence. The ZPL linewidth yields the total decoherence rate.

This dissertation presents experimental studies of the decoherence rate in CdSe/ZnS core/shell quantum dots (QDs), nanorods, and PbS QDs. The spectroscopic work is accomplished by using high-resolution spectral-hole burning (SHB), which eliminates effects of inhomogeneous broadening due to nanocrystal size variations. SHB response-dependence on the measurement timescale is also used to probe spectral diffusion: random spectral shifts in the optical transition frequency due to a fluctuating local environment.

These studies provide important information on decoherence processes in nanocrystals.

SHB response obtained from spherical CdSe/ZnS QDs exhibits a sharp ZPL and discrete acoustic phonon sidebands due to phonon-assisted transitions. The suppression of effects of spectral diffusion in the SHB measurement leads to a ZPL homogeneous linewidth of 1.5 GHz, corresponding to a decoherence rate of 0.75 GHz, which is more than one order-of-magnitude smaller than that observed previously, still far exceeding the expected radiative linewidth. The observed acoustic phonon sidebands are in agreement with a theoretical estimate of the confined phonon modes in nanocrystals. No ZPL, however, was observed in the SHB response of PbS QDs, reflecting the strong electron-phonon interaction in these nanocrystals.

The 0-D to 1-D transition is of particular interest, and is examined by comparing decoherence rates in QDs to those in nanorods. SHB response obtained from nanorods reveals a sharp ZPL along with a broad background of acoustic phonon sidebands. A decoherence rate of 4.4 GHz was observed, which is greater than that of spherical nanocrystals. Phonon-assisted exciton migration between localization sites in the one-dimensional confinement potential is proposed as a possible mechanism for the large homogeneous linewidth in the nanorods.

CURRICULUM VITAE

NAME OF AUTHOR: Sasha Dawn Tavenner Kruger

PLACE OF BIRTH: Anchorage, Alaska, United States of America

DATE OF BIRTH: 01/21/1977

GRADUATE AND UNDERGRADUATE SCHOOLS ATTENDED:

University of Oregon
University of Washington
Everett Community College

DEGREES AWARDED:

Doctor of Philosophy, Physics, 2006, University of Oregon
Master of Science in Physics, 1999, University of Oregon
Bachelor of Science in Physics, 1998, University of Washington
Associates in Arts and Sciences in Physics, 1995, Everett Community College

AREAS OF SPECIAL INTEREST:

Quantum Confinement Effects in Semiconductor Nanostructures
Semiconductor Optics

PROFESSIONAL EXPERIENCE:

Research Assistant, University of Oregon, 1999-2006
Semiconductor Optics
International RA at University of Osaka at Toyonaka, Japan, 2003

Teaching Assistant, University of Oregon, 1998-2001, 2004-2006
Introductory labs, Electronics lab, Semiconductor lab, Optics

Research Assistant, University of Washington, 1996-1998
Oceanography

GRANTS, AWARDS AND HONORS:

Integrative Graduate Education and Research Training (NSF-IGERT) Fellow,
University of Oregon, 2003, 2004, 2005

IGERT International Travel Award to University of Osaka at Toyonaka, Japan,
2003

Departmental Honors, Physics Department, University of Washington, 1998

Distinguished Graduate Award in Physics, Everett Community College, 1995

PUBLICATIONS:

Phedon Palinginis, Sasha Tavenner, Mark Lonergan, and Hailin Wang,
Physical Review B, **67**, “Dephasing of zero-phonon line in semiconductor quantum
dots: effects of phonon damping,” 201307-1, (2003).

Sasha Tavenner Kruger, Young-Shin Park, Mark Lonergan, Ulrike Woggon, and
Hailin Wang, *Nano Letters*, “Zero-phonon linewidth in CdSe/ZnS core/shell
nanorods,” *accepted for publication* (7/17/2006).

ACKNOWLEDGMENTS

The list of people to whom I am indebted for the successful completion of my program and this dissertation would far exceed the number that I can list here. I wish primarily to thank my family (Peep! Queep! Quack! Yes, you know what I mean) and my husband, Mark, for their steadfast support and encouragement. The stubborn streak I inherited helped too. I also thank and am deeply grateful to my advisors, Hailin Wang in Physics and Mark Lonergan in Chemistry, for their guidance, assistance, support, and unwavering willingness to take the time to do what needed to be done. In particular, I wish to thank Hailin for his terrific patience and support during the time I was struggling with the qualifying exam, and Mark for his ingenious and approachable analogies for explaining chemical processes to a physicist. The time I have spent in the lab with my labmates has helped us become both friends and colleagues. To those various and sundry labmates, whose friendly presence made learning and doing experiments worthwhile and fun, thank you, and good luck! In particular I have spent many enlightening hours in conversation with Sherman Fan, Mark Phillips, Scott Lacey, Phedon Palinginis, Yumin Shen, Susanta Sarkar, Shannon O'Leary, Young-Shin Park, Yan Guo, and Andrew Cook, among others. Of the chemistry students who taught me how to use equipment and become an effective pseudo-chemist, I particularly wish to thank Calvin Cheng and Lei Gao. Their training helped me do my work efficiently and safely.

I also wish to thank Scott Sweeney for the use of absorption data on two batches of jointly-made CdSe/ZnS nanocrystals, and Andreas Stonas and Dave Scutt of Voxel for helpful conversations. During my internship in the lab of Dr. Itoh I had the opportunity to

learn new techniques, see a different way to accomplish scientific experiments, and to experience a new and interesting culture. I am particularly grateful to Dr. and Mrs. Itoh for their support and help. Other members of the Itoh lab, Dr. Ashida, Dr. Kapitonov, Wantanabe-san, and Miyajima-san, all contributed to the terrific experience I had there.

My Aikido senseis have been especially supportive. Without the outlet of Aikido and the understanding of my friends there I am not sure that I could have finished the program in the good spirits in which I find myself. To them: thank you for your friendship, and thank you for allowing me the freedom to come to class when I could, so that I could concentrate on school when I needed to.

Without the timely and always friendly work and help of all the Physics Department and Oregon Center for Optics staff, none of this would have gone smoothly or well! To Sandy, Bonnie, Jani, Patty, Patty, and Joy, and all the other folks who have made the Physics office go 'round for all these years, thank you for your support and all the things you have done for me. To Colleen, Janine, and Brandy, wow! The OCO staff rock! In particular, your invaluable expertise and spectacular professionalism have made being an optics student that much more successful and joyful.

The investigations undertaken for this dissertation were supported for the most part by an NSF-IGERT Fellowship and by grants from the NSF and DARPA. The grant from which I was paid for my first summer was funded by the NSA, which is a fun factoid. Thank you to Hailin for supporting me on GTFs when necessary, and thank you to the Department for providing me with TAs which afforded me pedagogical training.

Thank you, everyone; it's been fun.

TABLE OF CONTENTS

Chapter	Page
I. INTRODUCTION	1
Confinement and applications	3
Studies accomplished and method	5
Historical and fabrication notes	7
Material notes	9
Plan for the dissertation	9
II. ENERGY LEVEL STRUCTURE IN SEMICONDUCTOR NANOCRYSTALS	11
Bulk crystal band structure	11
Excitons	18
Atomic energy levels and the exciton analogy	19
Exciton varieties	21
Quantum confinement	28
Energy level structures in quantum dots	34
Splitting caused by hexagonal lattice structure	35
Splitting caused by nonsphericity of a QD	36
Effect of electron-hole exchange interaction	37
Net effect	38
How perturbations affect empirical exciton fine structure	38
Energy level structures in nanorods	39
III. NANOCRYSTAL AND NANOROD SYNTHESIS AND CHARACTERIZATION	44
Nanocrystal synthesis	44
Synthesis process	48
Nanocrystal batches	55
Synthesizing nanorods	56
Characterization of the brand-new nanocrystals	58
Absorption	59
Photoluminescence	60
TEM	64
IV. TRANSITIONS UNDER THE SPECTRAL HOLE BURNING TECHNIQUE	67
Phonons	68
Electronic transitions	71
QDs as two-level systems	73

Chapter	Page
Inhomogeneously broadened sample	75
Spectral Hole Burning and experimental setup	76
Dephasing.....	82
Absorption	85
Absorption in a homogeneously broadened media	86
Absorption in an inhomogeneously broadened system in the presence of two excitation beams	87
 V. EXPERIMENTAL RESULTS FOR QUANTUM DOTS	 94
Discrete phonons	95
Exciton-phonon interaction	99
Confinement of exciton-phonon interactions	102
Phonon-assisted transitions	104
Spectral diffusion	105
Observations	107
Intensity dependence	112
Temperature dependence	114
Self-assembled versus chemically precipitated quantum dots	119
Material Matters: PbS QDs vs. CdSe/ZnS QDs	121
 VI. EXPERIMENTAL RESULTS FOR NANORODS AND CONCLUSIONS	 125
Spectral diffusion	127
Power broadening	130
Temperature dependence	131
Conclusions	133
 VII. SUMMARY AND OUTLOOK	 138
 APPENDIX	
A. NANOCRYSTAL SYNTHESIS	141
B. NANOROD SYNTHESIS	161
 BIBLIOGRAPHY	 164

LIST OF FIGURES

Figure	Page
1-1. Semiconductor structures by dimension. Bulk is 3-D, quantum wells are 2-D, quantum wires are 1-D, and quantum dots are 0-D.	2
2-1. Folding of the extended zone which produces the reduced-zone scheme picture. The valence and conduction bands are visible in this diagram as the parabolas with the narrow energy gap between them in the center zone. The lowest state shown is the free electron dispersion.	12
2-2. (a) Wurtzite (hexagonal) structure and (b) zinc-blende (cubic) crystal structures. Figure from Reference 40 Fig 9.7. The roman numerals indicate charge density planes of interest in solid state physics. The wurtzite structure is aligned with the \vec{c} -axis along \hat{z} , while zinc-blende is oriented with the (1,1,1) direction pointing along \hat{z}	13
2-3. Wurtzite (hexagonal) lattice and unit cell drawing. This is the view along the \vec{c} -axis. Along (111), however, within each layer the atoms are the same species and alternate between Cd and Se.	14
2-4. Hexagonal (a) and cubic (b) conduction and valence band structures. Δ_{SO} is the splitting caused by spin-orbit interaction, and Δ_{CF} is the crystal field splitting caused by lattice-induced strain.	15
2-5. First three energy levels of E_n for hydrogenic atoms.	19
2-6. General energy diagram for insulators and semiconductors.	21
2-7. a) The single particle picture of an electron and hole in a semiconductor. The electron occupies the conduction band. b) The interaction two-particle picture showing exciton energy level structure in a semiconductor. E_n is the intrinsic band gap of the bulk material.	24
2-8. The path of a real electron as opposed to that of an effective electron in two dimensions in a triangular lattice.	26
2-9. Density of state graphs for different dimensions.	29

Figure	Page
2-10. Dispersion relations of electrons and holes for different dimensionalities. For all cases, the dispersions above the thick, horizontal zero energy line are for electrons, and the dispersions below are for holes. In the 2-D and 1-D cases, the dispersion shown is for the confined direction(s) only, while the 3-D dispersion can be used for the unconfined direction(s).....	30
2-11. (a) Discrete energy levels in a CdSe quantum dot. Wave functions are shown for the states shown. ^{9,12} The listed CdSe band gap is the intrinsic band gap value at room temperature. At low temperature the value is 1.84 eV. (b) Energy levels in a perfect square well with infinitely high potential barriers.	33
2-12. Size dependence of the exciton band edge structure in ellipsoidal hexagonal CdSe QD with ellipticity taken to be prolate, where the size dependent ellipticity function is determined empirically. Source: Reference 52. The dashed lines represent dark states, while the solid lines represent bright states. The numbers are total angular momentum values, and U and L mean upper and lower (related to the sign conventions of the mathematical expressions for the plotted states). The dot radius is denoted a . The important thing to notice is that the lowest energy exciton state is dark.	39
3-1. Colloidal nanocrystals nucleate out of a liquid solution containing precursor materials. Nucleation occurs at a high temperature and growth at a somewhat lower temperature to reduce the incidence of new nanocrystal formation after the initial nucleation stage.	46
3-2. a) Colloidal CdSe/ZnS core-shell nanocrystal with a ligand shell made up of trioctylphosphine oxide. The core has a wurtzite structure. b) Bandgaps of the core and shell materials.....	47
3-3. TEM image of CdSe/ZnS core/shell nanocrystals. TEM magnification used was 430 kx, and the voltage used was 120 keV. The scale bar represents 20 nm. Note that some crystals are slightly more prolate than others.	48

Figure	Page
3-4. The dashed line represents the actual energy landscape that a nucleating drop or crystal must transition through as it grows. There is an initial energy barrier that must be overcome in order for the nanocrystal to consistently grow, as opposed to dissolving back into the liquid. The critical radius, at which continued growth is nominally ensured, is denoted r_c on the figure.	50
3-5. Ostwald ripening demonstrated through absorption spectra of uncapped nanocrystals cooked at 280°C for (top curve) 30 minutes and (bottom curve) 110 minutes. Note that the peak moves to the red (larger crystals) with time. The size distribution also increases, as is evidenced by the broadening of the absorption. No additional injections of stock solution were made between these two aliquots of the sample. The vertical line is a guide for the eye.....	51
3-6. CdSe nanorods. TEM magnification was 340 kx and voltage was 120 keV. The scale bar represents 20 nm.....	56
3-7. Nanorods batch 7. Notice the forked appearance of some rods, and the scraggly, messy appearance of the total collection of rods. TEM magnification was 160 kx and voltage was 120 keV. Scale bar length represents 20 nm.	57
3-8. Absorption spectra for two batches of CdSe cores of diameters a) 3.9 nm and b) 5.0 nm. (The plot for (b) is an 11-point Savitzky-Golay average, which reduces low-level noise.) Notice that the absorption peak moves to the red as the size grows. The height of the absorption peak is directly related to the density of the material in the liquid-filled cuvette used while recording data.....	59
3-9. The absorption of the same batch of CdSe nanocrystal rods both without shell layer (solid line) and with shell layer (dotted line) of ZnS. The vertical line was added to guide the eye. Typically, it is difficult to discern any shift in absorption wavelength by sight alone for non-monodisperse batches. For very high monodispersity the core/shell dots are slightly red-shifted from their core-only precursors due to partial exciton leakage into the shell. ⁵⁹ The arrows show the same relative feature (the knee of the absorption, where it begins to fall once again) for the capped (with shell) and uncapped (without shell) samples.....	60

Figure	Page
3-10. PL of the same batch of nanocrystals taken at room temperature and 4 K. Notice that the peak location has shifted.	62
3-11. Nanorod PL at a) a variety of temperatures, and b) the same batch at a variety of excitation intensities. All spectra in (b) were taken at temperatures 11.5-13.3 K. For both series, exciting light was at 532 nm.	63
3-12. a) and b) show TEM images of nearly spherical QDs and prolate QDs, respectively. c) shows a large size distribution of nanocrystals, while d) presents a well size-selected batch with low size dispersity. Electron energies are 120 keV for all images.	66
4-1. u is atom displacement. Figure from Klingshirn Figure 9.13a-d. ³⁹ M , the mass of the larger atoms, is represented by the large open circles. M is greater than m , the lower-mass atoms, represented by the small solid circles.	68
4-2. Dispersion curves for acoustic and optical phonons described by Equations 4.1 and 4.2, for an isotropic material. See Table 4.1 for values for ω_1 , ω_2 , and ω_3 . The top curve is for optical phonons and the bottom curve is for acoustic phonons in an isotropic lattice.	69
4-3. Acoustic and optical dispersion curves from the degeneracy has been lifted by an anisotropic lattice. Figure from Klingshirn Figure 9.15. ³⁹ T stands for transverse, L for longitudinal, A for acoustic, and O for optical.	70
4-4. Level diagram for exciton states in CdSe QDs. $ c\rangle$ is the exciton ground state and a dark state. $ b\rangle$ is the lowest energy bright exciton state, and $ a\rangle$ is the system ground state, in which no excitons are present.	72
4-5. Calculated linear absorption spectrum for a single CdSe QD. The QD is self assembled and assumed square in shape. Although broadening of the ZPL is not included in the model, the relative contribution from the ZPL and the acoustic phonon assisted transitions to the zero <i>optical</i> phonon line (often called the acoustic phonon pedestal) is reproduced well.	74

Figure	Page
4-6. The arrow shows the location of the pump beam within the inhomogeneously broadened absorption profile of the sample. The dotted line shows the spectral window excited by the pump and outlines the absorption profile that the probe beam experiences.	77
4-7. SHB schematic. Temperature is typically held between 4 and 12 K.....	79
4-8. Spectral diffusion schematic. If measurements are made slowly compared to the transition energy diffusion rate, the linewidth we measure is wider than the actual decoherence-broadened linewidth homogeneous linewidth.	80
4-9. Overall SHB schematic. A stands for analyzer, B for beam splitter, D for detector, L for lens, P for polarizer, and WP for wave plate, in this case $\lambda/2$	81
4-10. Transmission, rather than absorption. Broad incoherent spectral hole with a sharp coherent <i>absorption</i> dip at zero detuning. γ is taken to be much greater than Γ ($\gamma = 20\Gamma$ for plotting purposes). Recall that for absorption, this picture would be upside-down, with the “base” at $\alpha = 1$, provided the graph is normalized by α_0	92
5-1. Absorption and spectral hole burning spectra with phonon sidebands. The absorption signal is calculated while the SHB signal is actual data from CdSe/ZnS QDs. In the SHB data, the tall, sharp peak is the ZPL, the two small flanking peaks are discrete acoustic phonon sidebands, and the large background peak consists of a large number of semi-continuous acoustic phonon sidebands.....	96
5-2. QD size dependence of lowest dephasing rate measured for each sample. T=4 K, modulation frequency=100 kHz.....	97
5-3. The calculated size dependence of the first acoustic phonon sideband, compared with the energy measured for four sizes of real QDs. Data taken at 10 K and 100 kHz modulation frequency. Intensities I_{pump} and I_{probe} are unknown to the author.....	98

Figure	Page
5-4. Electronic states coupled to discrete phonon states leads to a series of discrete transitions. Discrete transitions appear as peaks in both the absorption and SHB spectra. The ZPL is the $m=0$ to $n=0$ transition, and is represented by the vertical solid arrow. The vertical long-dashed line represents the energy of the lowest energy exciton. The number of phonons involved in an excitation is determined by the m and n values of a given transition. The short-dashed arrows show examples of non-ZPL transitions that could take place. Several assumptions are made: 1) The Franck-Condon principle holds. That is, the electronic transition is very fast compared with the motion of the lattice. 2) Each lattice vibrational mode is well described by a quantum harmonic oscillator. This has been calculated to be correct to a great deal of precision, but only at low temperature, by Gusev <i>et al.</i> ⁸² 3) Only the lowest phonon mode(s) are excited. For sufficiently low temperatures, this may be assumed correct. Our experiments reveal a manifold of phonons in the acoustic phonon pedestal, so the assumption is minorly inappropriate. Only a finite and small number of phonons are excited, however, so the model presented above is acceptable for understanding a single transition. 4) The interaction between the exciton and the lattice is the same in both the ground state and the excited state. The assumption is represented above by two equal harmonic oscillator potentials. The assumption is met due to the low Franck-Condon factors associated with CdSe.	101
5-5. Experimental differential transmission spectrum for quantum dots as a function of detuning. Note the relative energies of LO and acoustic phonon sidebands relative to the ZPL. This data was taken at 4.2 K.	103
5-6. ZPL of the same sample for pump modulation frequencies of, in order of decreasing peak intensity: 1, 10, 20, 50, and 100 kHz. See Figure 5-7 for conditions.	107
5-7. Exciton dephasing rate in QDs versus pump modulation frequency; the modulation frequency sets the measurement timescale. The data shown was taken by Phedon Palinginis on a quantum dot sample synthesized by Xudong Fan. Dot diameter=9 nm, $T=1.8$ K, $I_{\text{pump}}=1.0$ W/cm ² , and $I_{\text{probe}}=0.5$ W/cm ²	108
5-8. Power broadened ZPL spectra for, in order of increasing peak intensity, a pump power of 100, 200, 400, 800, 1600, 3600, and 5200 μ W. Notice that both the magnitude and width of the spectra increase with increasing power. $T = 5.5$ K.	112

Figure	Page
5-9. QD power broadening as a function of pump beam intensity. Data taken by Phedon Palinginis. Modulation frequency is 100 kHz. Note the use of logarithmic scale. The inset shows the same data on a linear scale.	114
5-10. The phonon pedestal expands and the LO phonon sidebands broaden as the temperature rises. Similarly, acoustic phonon sidebands disappear with rising temperature although they are not visible on this scale. These spectra, from lowest to highest pedestal intensity, are taken at T= 10, 20, 40, and 60 K respectively. The modulation frequency is 2 kHz and the pump is at 635 nm.	117
5-11. The ZPL width expands as the temperature increases. In order of increasing peak height, these spectra were taken at 23, 12, and 4 K respectively. The spectral weight of the ZPL shrinks relative to the acoustic phonon sidebands as temperature rises.	118
5-12. Temperature dependence of the dephasing rate of colloidal quantum dots. The line is a fit to the data using Equation 5.14. Data taken by Phedon Palinginis. Nanocrystal average diameter is 9 nm and the modulation frequency is 100 kHz. Graph from Reference 89.	118
5-13. Temperature dependence of the dephasing rate of self-assembled CdSe/ZnSe QDs. Data taken by Phedon Palinginis. The modulation frequency is 3MHz.	119
5-14. Spectral diffusion effects in self-assembled CdSe/ZnSe QDs. T=10 K.	120
6-1. Nanorod ZPL in the SHB response observed at, for decreasing peak intensity, modulation frequencies of 1, 20, 40, 60, 80, and 100 kHz, respectively. For each datum, T = 8 K, pump intensity = 3 W/cm ² , and probe intensity = 1 W/cm ²	128
6-2. Decoherence rate versus modulation frequency for both nanorods (squares) and quantum dots (triangles). T = 8 K, pump intensity = 3 W/cm ² , and probe intensity = 1 W/cm ²	129
6-3. Dephasing rate versus pump beam intensity. Nanorods (squares) broaden at a more gradual rate than spherical nanocrystals (triangles). Modulation frequency = 1 kHz, T = 8 K, probe intensity = 1 W/cm ²	130

Figure	Page
6-4. The pump beam intensity dependence for CdSe/ZnS nanorods (squares) and quantum dots (triangles) displayed on a log plot. Conditions are the same as in Figure 6-3.	131
6-5. Temperature dependence of dephasing rate in nanorods. Modulation frequency = 1 kHz, pump intensity = 3 W/cm ² , probe intensity = 0.3 W/cm ² . The line is a fit described by Equation 5.14.....	132
6-6. The same temperature data given above for nanorods. The fit on the left is a standard exponential fit. The fit on the right is a standard exponential fit for a temperature dependence of T ^{1.65} (see the text).....	134
A-1. Schematic of the TOP transfer cascade.	144
A-2. Schematic of synthesis glassware and other equipment.	153

LIST OF TABLES

Table	Page
2-1. Density of states in a semiconductor	28
3-1. Stock solution ingredients	49
3-2. CdSe amounts and temperatures for three batches	55
3-3. ZnS amounts and temperatures for three batches	55
3-4. Size versus PL for three batches	55
4-1. Anisotropic dispersion frequency values at Brillouin zone edge	71
5.1. Data taken by Empedocles, <i>et al.</i> ⁷³ for intensity dependence of the spectral diffusion of a single CdSe nanocrystal.	113

CHAPTER 1

INTRODUCTION

The desire to understand and exploit the evolution of bulk semiconductor structural and electronic properties beginning from the atomic or molecular scale drives much of the development of low-dimension semiconductor structures. Advancing synthesis techniques have yielded ever smaller and more controllable structures. Understanding the physics inherent in these structures leads both to more precise models of fundamental interactions in the quantum confinement regime, but also leads to applications unapproachable by conventional materials. The realm of so-called quantum dots, especially, lies between traditional chemistry and solid state physics; between atoms and solids. The form of a quantum dot is essentially that of a large molecule, consisting of hundreds to a few thousand atoms, which interacts with a light field as if it were a single atom. The electronic energy levels are discrete, rather than bulk semiconductor bands, and are describable as molecular orbitals.

As the size of a quantum dot approaches the Bohr radius of the bulk exciton, quantum confinement effects become pronounced and lead to considerable modification of the optical and electronic properties of the semiconductor material. The energy levels of excitons in quantum dots are blueshifted compared with excitons in the bulk due to quantum confinement. In addition, the nonlinear polarizability and transition oscillator strength are spectrally concentrated and increased in magnitude in the size regime of

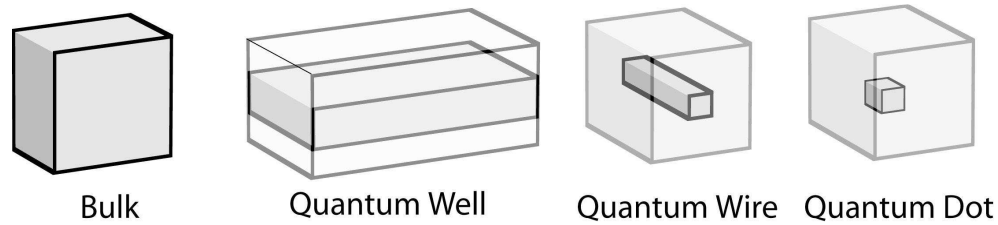


Figure 1-1: Semiconductor structures by dimension. Bulk is 3-D, quantum wells are 2-D, quantum wires are 1-D, and quantum dots are 0-D.

quantum dots. Light emission from quantum dots has a higher quantum efficiency than emission from bulk materials. These properties make quantum dots good candidates for a wide variety of applications, including biological labeling,¹⁻³ low threshold lasers,⁴⁻¹¹ and optical network components.⁹

Like bulk semiconductors, quantum dots (QDs) are crystalline and can support fundamental excitations such as plasmons, phonons, and excitons. Excitons, which are excited electronic states of the crystal, have, as described above, atomic-like (discrete) energy levels when confined at quantum mechanical scales. Thus, QDs are pseudo-atomic systems with the added benefit of ease of handling and study (compared to atoms), while the energy levels they contain are complicated by electron interaction with the material lattice via phonons. Device developers use quantum confinement effects for band gap engineering, which leads to materials with very specific electronic and optical properties.

Due to the practical and basic science benefits of studying low-dimension systems, semiconductor nanostructure technology has advanced at a very rapid pace over the past two decades. As knowledge of fundamental interactions in nanostructured materials grows, particular interest is directed at decoherence effects. The bulk of the work presented in this dissertation concerns itself with elucidating decoherence of excitons in both quantum dots and

elongated structures called nanorods. The word nanostructure refers to the typically few-nanometer size of the structures, which provides quantum confinement of charge carriers. So-called quantum wells, wires, and dots (2-D, 1-D, and 0-D, respectively, where D stands for dimension) have all been developed.

Confinement and applications

Confinement also leads to an increase in the effective band gap of the material. Confinement energy causes excited exciton states to move higher in energy as the structure size is reduced, just as energy levels move higher in an infinite potential square well as the well width is reduced. The dot size deeply affects energy levels and exciton fine structure through the strong size dependence of the exchange interaction and confinement energy.

The advantages inherent in using low-dimension systems for devices as opposed to using bulk materials are varied. They include, depending on the specifics of the system, improved efficiency, speed, gain, and noise reduction, as well as a reduced threshold current density and sensitivity to operating temperature. This last item is due to energy spacing in the strong confinement regime being larger than $k_B T$.^{9,12} Additionally, oscillator strength becomes more concentrated as dimension is reduced, just as absorption becomes spectrally discrete. Gain, therefore, is also repartitioned into discrete states. The transition rate per electron-hole pair stays the same even as dimension is reduced,¹³ which leads to very strong lasing capability.^{4,5}

The potential of quantum information processing has generated excitement for many years. Quantum dots have been investigated as integral parts of a variety of quantum information processing schemes.¹⁴⁻¹⁶ Despite the difficulty associated with using exciton states as qubits (quantum bits), some progress has been made. In general, exciton coherence in quantum dots is too fragile to be used for these schemes, although improvements in system design and dot fabrication may make quantum dots viable as components in the future.

Another potential application of particular interest has been the storage of light, or of information transmitted by light. A requirement for this application is a slow dephasing rate. So-called slow light has been demonstrated in GaAs quantum well systems using the coherence of excitons.¹⁷ Another demonstrated phenomenon using exciton coherence is electromagnetically-induced transparency (EIT). EIT based on exciton correlations was first observed in GaAs quantum wells.¹⁸ However, electron spin coherence is much more robust than exciton coherence since electron spin undergoes much slower dephasing than excitons.¹⁹ Excitons decohere too quickly in CdSe/ZnS QDs and nanorods, the materials discussed in this dissertation, to be used for this application.^{20,21} It remains an open question whether better synthesis methods can decrease the decoherence rate of excitons in quantum dots or nanorods enough to make either of the exciting technologies of EIT or slow light as feasible using exciton coherence as electron spin.

Specific physical processes are useful for particular applications. For example, absorption and recombination in bulk semiconductor is the critical process needed for the operation of photodetectors, amplifiers, lasers, and LEDs, among others. At low-

dimension, this same process is appropriate for making ultralow threshold lasers, and even two-dimensional laser arrays,⁶⁻¹¹ among other nonlinear photonic devices. Other uses investigated for semiconductor nanostructures include photonic network components, such as optical switches and modulators⁹ and light emitting diodes (LEDs).⁸

Studies accomplished and method

In the studies presented in this dissertation, we seek to clarify optical transitions in three systems: CdSe/ZnS core/shell QDs, PbS QDs, and CdSe/ZnS core/shell nanorods. Differing energy level structures and interactions in these systems affect the dephasing processes undergone by excitons. Analyzing the optical transitions available to excitons assists our understanding of the interactions that are taking place.

In order to probe the sources of dephasing in these samples we must parameterize our results. In particular, we study the temperature dependence, excitation intensity dependence, and the measurement timescale dependence of the homogeneous linewidths of the samples. Nonlinear optical theory provides a framework for understanding how each parameter is related to the optical transitions taking place in the sample, and what variety of information we can deduce based on our observations of these transitions.

The measurement timescale is important in determining (and reducing the effects of) spectral diffusion. When a microscopic local electric field fluctuates it causes the transition energies of the nanostructures to fluctuate too, causing *spectral diffusion*, but inhomogeneously since the local electric field is different in each part of the sample. If we measure the homogeneous linewidth of the sample on a slow timescale, the transition

energies have a chance to diffuse and we observe a broad transition linewidth. If we make measurements on a faster scale we can measure the linewidth before the transition energy has had a chance to diffuse. By measuring the linewidth at a variety of timescales, we delineate the effects of spectral diffusion on the observed linewidth.

Power broadening is caused by the saturation-level excitation of an inhomogeneously broadened sample, such as an ensemble of QDs. As the absorption tails of nanoparticles that are *not* resonant with the pump beam cause those nanoparticles to become excited, the measured linewidth broadens monotonically with pump beam intensity. We typically work at low intensities ($0.5\text{-}3\text{ W/cm}^2$) in order to minimize power broadening effects due to intensity-dependent spectral diffusion in the measured linewidth.

Temperature has a particularly potent effect on the homogeneous linewidths of the samples. Exciton-phonon coupling is temperature dependent, and nonradiative relaxation of excitons via interactions with phonons becomes much more efficient as the temperature increases. The number of phonons present also increases with temperature. Additionally, phonon spectra that are discrete due to quantum confinement become continuous as the temperature rises from liquid helium temperatures. Continuous phonon spectra lift certain electron-phonon interaction energy conditions, making interactions that cause decoherence more likely to take place. Increased exciton-phonon interaction due to these temperature-dependent effects leads to a greater exciton dephasing rate, which corresponds to a wider measured linewidth.

The technique we use to elucidate the optical transitions undergone by the excitons is high-resolution modulation frequency-dependent spectral hole burning (SHB). As a

continuous wave (CW) technique, it is unusual that it can be used to probe and eliminate the effects of spectral diffusion. The modulation frequency dependence is the key to this added utility. The technique also has an advantage over single nanocrystal spectroscopy and photon echo experiments. Each of these lacks sufficient sensitivity and requires high intensity, which leads to power broadening; additionally, neither can determine the effects of spectral diffusion. Modulation frequency-dependent SHB requires only very low excitation intensity, has nano-eV resolution, and circumvents nanocrystal size distribution broadening present in the sample by exciting only a subset of nanocrystals resonant with the pump beam. The most unique aspect of the technique is the aforementioned ability to delineate the effects of measurement timescale on the measured linewidth.

Despite minimizing the effects of spectral diffusion, and working at low temperature and excitation intensity, we find that the lowest measured decoherence rate (one fourth the SHB linewidth, or one half the homogeneous linewidth) of both QDs and nanorods far exceeds the expected radiative decoherence rate of 0.03 GHz. Therefore, our results are not yet lifetime limited. This means that sources of decoherence unrelated to lifetime dephasing, most likely due to electron-phonon interactions, remain active in all the samples studied.

Historical and fabrication notes

Initially, nanostructures were fabricated “from the top down” by growing or depositing one semiconductor on a substrate of a different semiconductor (most venerably, doped GaAs on undoped GaAs⁹) and then etching away extraneous material.

While this process could yield high-quality quantum wells, wires, and pillars (vertical wires) on a sub-micron scale, it introduced far too many optical-property-destroying defects to the QDs produced.

“Bottom up” fabrication methods are of interest both to improve the quality of the structures produced, but also to address the wastefulness of the “top down” method.⁸ Towards this end, more specific and controllable epitaxial growth techniques were developed, as well as chemical synthesis methods that yield different shapes. Epitaxial growth of self-assembled QDs allows for the production of a large number of uniform dots in a single process step.¹² QDs grown epitaxially are (often) pancake-shaped. Strain, surface energy, and interaction with surrounding dots determine the dot size, shape, and distribution.²² Strain-induced surface fluctuations between two layers of semiconductor can also act as QDs. Peculiar shapes, such as pyramids^{12,23-25} have been grown. Chemical precipitation methods in organic liquids or gels yield high-quality, colloidal, nearly spherical QDs^{26,27} and rods²⁸⁻³⁰ (which is the transitional state between 0-D and 1-D), amongst other shapes.³¹⁻³³ In contrast to epitaxially grown dots, however, precipitated dots always grow with a relatively large size distribution (although some part of the distribution may be removed from the batch using post-growth purification procedures). The advantage of chemically synthesized QDs lie in their nearly spherical shape and the fact that they can be functionalized and attached to a variety of surfaces or even molecules. Their density is also highly controllable.

Material notes

For optical applications, semiconductors such as CdSe, InP, GaAs, and Si are popular materials-of-choice.³⁴ This is so for the simple reason that the primary decay pathway of excitons is the production of light rather than heat in these (sp^3 -hybridized) materials. The reason for this is that the creation of an exciton does not distort the lattice much. This means the Franck-Condon factors are small. The exciton, once created, also experiences small Franck-Condon factors and therefore a very slow conversion to heat. This allows excitons to experience a sufficiently long lifetime so that radiative decay can take place.

Plan for the dissertation

As will be discussed in Chapter Two, several parameters play a role in the exciton energy level structure. The size of the nanostructures has the greatest effect. Other determining factors are the crystal field associated with the lattice structure, and the shape of the nanostructure. Our samples range from spheres to rods, so we are particularly interested in the effect of shape: how elongation of the structure in one direction, and the associated permanent electric dipole, affects the exciton-phonon interaction. We investigate energy level structures of the two morphologies.

These rod-shaped nanocrystals are promising for various applications due especially to the linearly polarized emission that they exhibit.^{35,36} The PL efficiency of nanorods is also shown to be higher than QDs,³⁷ and due to their charge transport properties, they are investigated as components in efficient solar cells.³⁸

In Chapter Three, the fabrication and characterization of the quantum dot and nanorod systems are discussed. Optical theory of spectral hole burning and the experimental setup, which is used to extract the dephasing time of excitons within the nanocrystals, is examined in Chapter Four. The following two chapters, Five and Six, document experiments made on nanocrystal dots (both core/shell CdSe/ZnS and core-only PbS), and experiments made on nanocrystal rods (exclusively core/shell CdSe/ZnS), seeking the parameterization of factors that influence the value of the homogeneous linewidth.

The final chapter, Chapter Six, also contains a summary of the results and a discussion of conclusions drawn from the experiments. We find that CdSe/ZnS nanorods exhibit a dephasing rate that is comparable to, but higher than, the rate in QDs. We also see that the effects of spectral diffusion on the measured linewidths of the samples are different in the two morphologies. The relative linewidth change over a given modulation frequency range is close to 75% for QDs, while it is only 54% for nanorods. Summaries of the effects of each parameter on the overall dephasing rate demonstrate a consistent picture of the types of exciton decoherence that can take place in semiconductor nanostructures. A mechanism for exciton migration is proposed that may account for some of the observed decoherence rate in excess of the expected radiative rate in nanorods. Appendices discuss detailed synthesis procedures for CdSe/ZnS nanorods and QDs.

CHAPTER 2

ENERGY LEVEL STRUCTURE IN SEMICONDUCTOR NANOCRYSTALS

Zero-dimensional, bulk, and intermediate semiconductor systems have different energy level structures. Energy level structure depends upon a variety of factors such as the density of states, the Coulomb interaction, and carrier-lattice interactions. This chapter discusses the energy level structures of optical transitions in semiconductor nanostructures. Due to the complexity of the calculations, the overview presented here is mostly qualitative in nature. The discussion begins with a general description of bulk energy bands and then continues with the effects of quantum confinement, hexagonal lattice structure, degeneracy of the valence band, and slight nonsphericity of the dots. These discussions lead to a reasonable picture of interband optical transitions in CdSe quantum dots. The chapter ends with an examination of nanorods, in which the prolateness of the dots is taken to an extreme.

Bulk crystal band structure

A crystalline lattice consists of atoms arranged in a regular, repeating pattern. A solid is crystalline if it has a periodic (translation invariant) structure. A variety of atomic species may make up the lattice. Periodicity is crucial as the source of many crystal properties. Periodicity allows the use of Bloch wave solutions to the Schrödinger

equation, and is the origin of energy band gaps. Clear examples of the origin of band gaps are worked out in a wide variety of solid state and quantum mechanics textbooks.

The gist of the solution is that Bloch waves are the proper eigenstates of a periodic potential. Corrections to the dispersion curve at the location of the reciprocal lattice vector cause discontinuities in energy (see Figure 2-1). When we switch to the reduced zone picture, these discontinuities clearly form the band gaps with which we are already familiar. It should be mentioned that the bands are not strictly parabolic. However, in wurtzite, direct, wide band gap semiconductors, the minimum of the conduction band, to a good approximation, is isotropic and parabolic near $k=0$.³⁹ We can neglect, therefore, the nonparabolicity of the conduction band in most cases considered here.

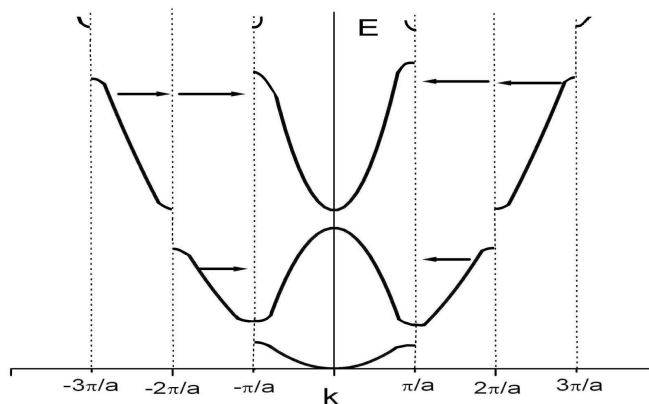


Figure 2-1: Folding of the extended zone which produces the reduced-zone scheme picture. The valence and conduction bands are visible in this diagram as the parabolas with the narrow energy gap between them in the center zone. The lowest state shown is the free electron dispersion.

The exact arrangement of atoms is an important consideration in analyzing the energy fine structure of excitons. The CdSe nanocrystals used in the studies described in Chapters Five and Six have a hexagonal lattice structure. A hexagonal lattice structure with a small crystal field splitting value may be described by a *quasicubic* model, since the wurtzite structure is a subset of cubic atomic arrangements. This is acceptable for CdSe since it has a crystal field splitting value of only 25 meV. Despite this similarity, hexagonal and cubic lattices have different physical structures (see Figures 2-2 and 2-3) and different energy bands (see Figure 2-4). Use of the quasicubic model means that calculations of energy level structure are performed for a cubic lattice structure rather than a hexagonal one. Corrections to the exciton fine structure provided by including the hexagonal structure are small enough that they may be treated as perturbations.⁴¹ An additional consideration for interpretation of exciton fine structure is the presence of defects in the crystal structure. Defects can trap charge, and,

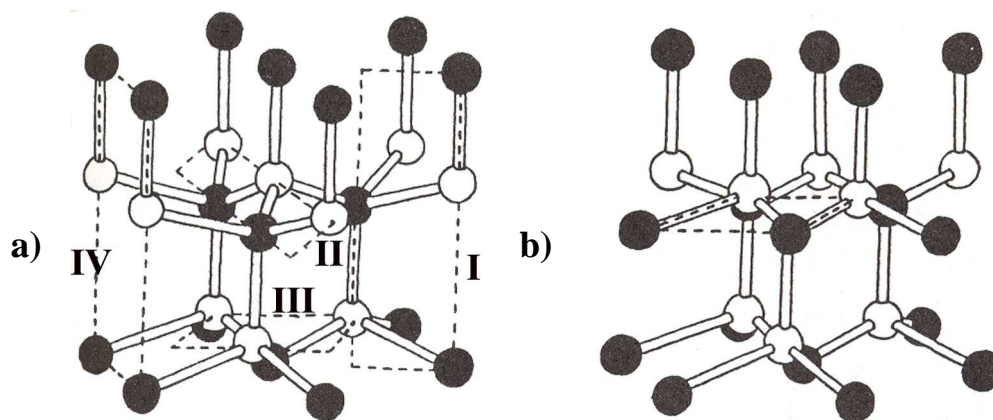


Figure 2-2: (a) Wurtzite (hexagonal) structure and (b) zinc-blende (cubic) crystal structures. Figure from Reference 40 Fig 9.7. The roman numerals indicate charge density planes of interest in solid state physics. The wurtzite structure is aligned with the \bar{c} -axis along \hat{z} , while zinc-blende is oriented with the (1,1,1) direction pointing along \hat{z} .

furthermore, always change the local potential energy environment that charge carriers experience. Sometimes defects are deliberately introduced (for example, by doping the crystal with a non-native atomic species) in order to test the assignment of certain energy transitions in the exciton fine structure. In contrast to some of the early conclusions about the origin of exciton fine structure in CdSe QDs,^{42,43} defects do not cause the most prominent differences in exciton fine structure between QDs and bulk crystal. In addition, the topic of defects is not important for appreciating the basic physics of confined excitons in QDs. Therefore, lattice defects will not be explored any further here.

The bottom of the conduction band (CB) in wurtzite-structure semiconductors has an s-like ($l = 0$) nature, and the top of the valence band (VB) has a p-like ($l = 1$) nature. Atomic orbitals overlap as the atoms are brought close together, which causes the eigenenergies of the electrons split and broaden into bands due to the overlap of their

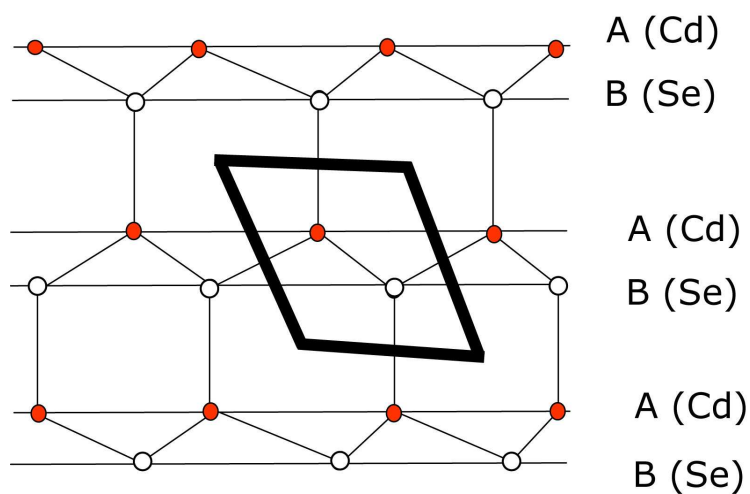


Figure 2-3: Wurtzite (hexagonal) lattice and unit cell drawing. This is the view along the \bar{c} -axis. Along (111), however, within each layer the atoms are the same species and alternate between Cd and Se.

wave functions. The reason for the p-like VB is different for ionic and covalent crystals.³⁹ For more covalent crystals, such as CdSe, the VB arises from the bonding state of the sp^3 -hybrid orbitals.

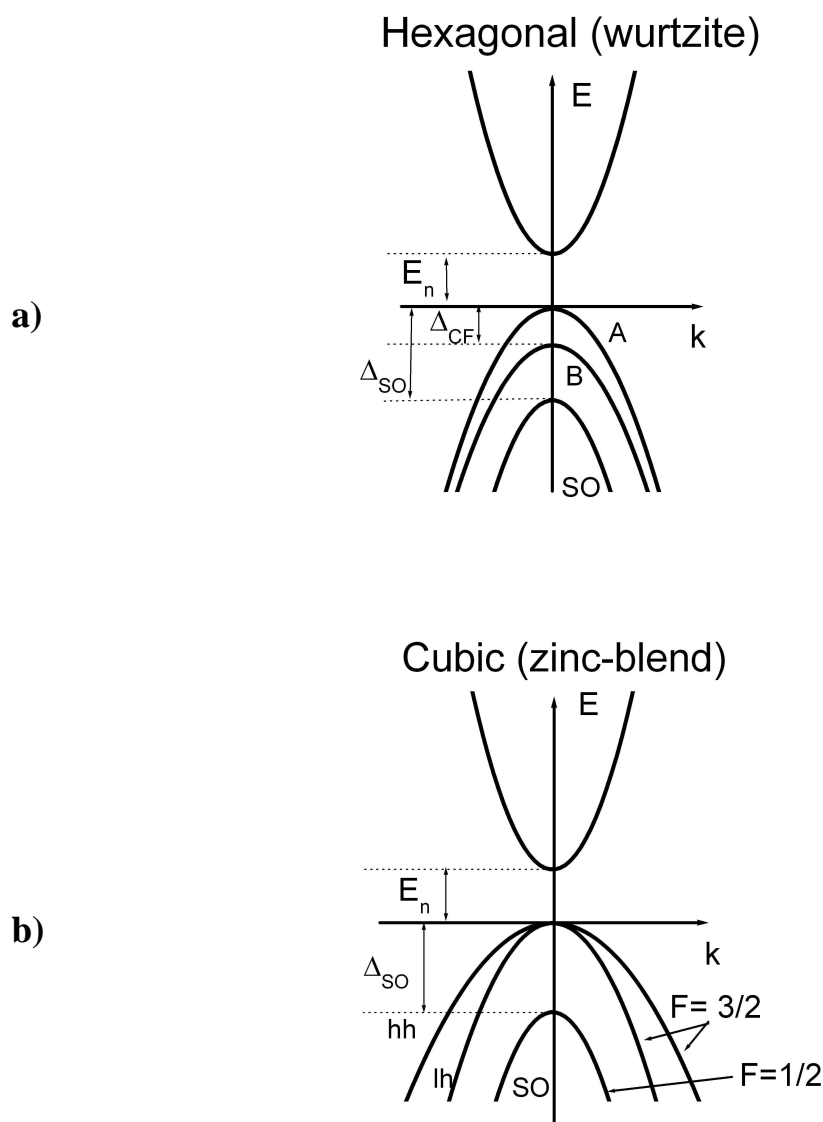


Figure 2-4: Hexagonal (a) and cubic (b) conduction and valence band structures. Δ_{SO} is the splitting caused by spin-orbit interaction, and Δ_{CF} is the crystal field splitting caused by lattice-induced strain.

The lowest CB comes from the lowest empty s-levels of the antibonding sp^3 -hybrid. We refer to it as $1S_e$, since electrons inhabit the CB. The numeral 1 indicates $n = 1$ and S refers to the $l = m = 0$ (lowest angular momentum) state. The first level of the VB is denoted $1S_{h,3/2}$.⁴⁴⁻⁴⁶

The CB is twofold degenerate, accounting for spin-up and spin-down states. Similarly, the VB is sixfold degenerate at the Γ -point (the Brillouin zone center) if spin is included. In a hexagonal structure, when the effects of spin-orbit coupling and the strain induced by the crystal field (due to the reduced symmetry in the hexagonal crystal structure) are included, three subbands split off. They are generally labeled A, B, and SO. SO stands for split off.

We now begin the investigation of QD band structure starting from a cubic, rather than hexagonal, picture. In zinc-blende crystals, the VB is also sixfold degenerate (including spin), which corresponds with the parent p-orbitals. The VB splits at $k=0$ into a fourfold degenerate band, the top of which is the highest VB point, and a twofold degenerate band, also called the split off band. The split off is caused by spin-orbit coupling.⁴⁷ The relatively strong spin-orbit coupling of the states with zero orbital angular momentum is reflected in the large energy shift of the SO band from the higher-lying bands. Away from $k=0$, the fourfold degenerate band splits into two twofold degenerate bands, called the heavy hole and light hole bands because of their difference in curvature. The dispersions of the heavy and light hole bands are described by the so-called Luttinger parameters: γ_1 , γ_2 , and γ_3 . These Luttinger parameters appear in the Luttinger Hamiltonian, which can be found in References 39 and 47. γ_1^{-1} describes the

average effective mass, and γ_2 and γ_3 describe the splitting into heavy and light hole bands, among other phenomena.

We consider total angular momentum, \vec{F} , which is the sum of the orbital (\vec{L}) and electron spin (\vec{s}_e) angular momenta. We take eigenstates $|F, F_z\rangle$, analogous to the atomic spin-orbit description. Recall that \vec{L} can be $0, \pm 1, \pm 2, \dots$, while electron spin, \vec{s}_e , may have values of $\pm 1/2$.

Within the quasicubic framework, VB states may be written

$$|F, F_z\rangle = \left| \frac{3}{2}, \pm \frac{3}{2} \right\rangle, \left| \frac{3}{2}, \pm \frac{1}{2} \right\rangle, \left| \frac{1}{2}, \pm \frac{1}{2} \right\rangle. \quad (2.1)$$

The aforementioned split off band is represented by the $\left| \frac{1}{2}, \pm \frac{1}{2} \right\rangle$ states. As can be seen in Figure 2-4, the SO band is sufficiently distant from the higher VB levels that it may usually be ignored in discussions of band-edge transitions. The diagonal matrix elements of the Luttinger Hamiltonian produce the VB dispersion of all three bands. Concentrating on the upper two bands, a basis of $|F, F_z\rangle = |3/2, \pm 3/2\rangle$ yields the heavy hole band, and a basis of $|3/2, \pm 1/2\rangle$ yields the light hole band.⁴⁸ In particular, the dispersions may be written

$$E_{HH} = -\frac{\hbar^2}{2m_0} \left[(\gamma_1 + \gamma_2)(k_x^2 + k_y^2) + (\gamma_1 - 2\gamma_2)k_z^2 \right] \quad (2.2)$$

$$E_{LH} = -\frac{\hbar^2}{2m_0} \left[(\gamma_1 - \gamma_2)(k_x^2 + k_y^2) + (\gamma_1 + 2\gamma_2)k_z^2 \right]. \quad (2.3)$$

The bands have cubic symmetry, which means that hole masses depend on the direction of \vec{k} relative to the crystal axis. In fact, in both cubic and hexagonal lattices, the effective masses associated with the VBs are strongly anisotropic, unlike the CB. The effective mass, m_{\perp} , of a particle whose wave vector, \vec{k} , is perpendicular to the polar crystallographic axis, \vec{c} , is usually much smaller than m_{\parallel} . The effective mass used for calculating the density of states is typically written

$$m_{DOS} = (m_{\perp}^2 m_{\parallel})^{1/3}. \quad (2.4)$$

The specific heavy hole and light hole effective masses are expressible in terms of the same Luttinger parameters used above:

$$m_{HH\perp} = \frac{m_0}{\gamma_1 + \gamma_2}, \quad m_{HH\parallel} = \frac{m_0}{\gamma_1 - 2\gamma_2}, \quad (2.5)$$

$$m_{LH\perp} = \frac{m_0}{\gamma_1 - \gamma_2}, \quad m_{LH\parallel} = \frac{m_0}{\gamma_1 + 2\gamma_2}. \quad (2.6)$$

Excitons

The band gap of a semiconductor is the energy difference between the top of the VB and the bottom of the CB, and is the energy necessary to create an *unbound* electron-hole pair. This assumes a direct semiconductor, in which the minimum of the conduction band and the maximum of the valence band both occur at the same k value. Two further assumptions are that the electron and hole are created at rest and far enough apart so that the Coulomb interaction between them is negligible. If one carrier approaches the other, they may form a bound state.⁴⁵ The bound state of the electron and hole is called an *exciton*. The binding energy reduces the

energy needed to form an exciton (carriers already correlated on creation) to just below the band gap.

Atomic systems, in particular, hydrogenic systems, provide a robust analogy for the exciton. A short review is in order.

Atomic energy levels and the exciton analogy

An exciton in a semiconductor consists of an electron that is promoted to the conduction band from the valence band, and the positively charged vacancy it leaves behind, called a hole. In analogy to hydrogen, in which an electron is bound to a positively charged proton, the electron and hole are bound by the Coulomb force and exhibit discrete energy bands. In contrast to the atomic system, the exciton system's lowest energy state consists of zero excitons present, and the first excited state is reached when an electron is sent into the conduction band and the lowest-energy exciton is created. In the atomic system ground state, the electron is already in its lowest energy orbital and excitation simply promotes it to a higher energy orbital. One more complication in the analogy is that excitons interact with the lattice.

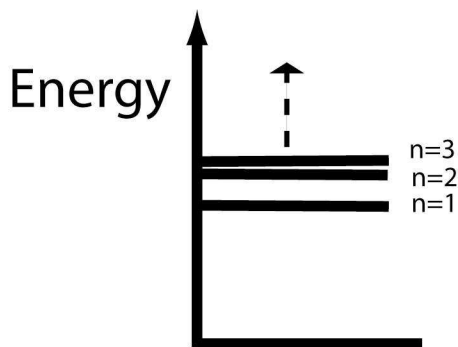


Figure 2-5: First three energy levels of E_n for hydrogenic atoms.

Despite the wrinkles in the analogy between excitons and hydrogen, the atomic case can still offer us insight. We offer here the solution of the Schrödinger equation in the atomic case, assuming a separable wave equation and a $1/r$ potential. The origin of atomic spectrum fine structure is largely the same as for excitons. It is found that, for atoms with one electron,

$$E_n = -\frac{1}{(4\pi\epsilon_0)^2} \frac{Z^2 e^4 m_r}{2\hbar^2 n^2}, \quad (2.7)$$

where Z represents the number of protons in the nucleus, m_r is the reduced mass, and n is the principal quantum number. Excellent reviews of this calculation can be found in most quantum mechanics and atomic physics textbooks.⁴⁹ The energy levels so derived are the main electronic levels of the atom. Further energy states are available, which are clustered around each main level and are splittings of that level. They have much smaller spacing from each other than the main electronic levels do. These energy states are called fine and hyperfine levels.

Fine structure arises from relativistic effects due to the interaction between the electric field of the nuclear charge (or the hole, in the case of excitons) and the relativistic orbital motion of an electron with spin. For all but the hydrogen atom (which has only one electron), the largest contribution to the fine structure is caused by the spin-orbit interaction. This is true also of excitons. Other effects are averaged out due to the presence of more than one electron in the material or surrounding the atom. Hyperfine structure is caused by the interaction of the nucleus' multipole moments of order two and higher with the electromagnetic field produced at the nucleus by the electrons.

Exciton varieties

There are different types of excitons—in particular, strongly bound, intermediately bound, and weakly bound. Material properties dictate the exciton properties and the energy level structure. We focus on covalently or ionically bound crystals. Insulating materials are more ionic in nature, while semiconductors are more covalent.

Both insulators and semiconductors have a Fermi level in the bandgap. Electrons surrounding the atoms are prevented from becoming excited to the conduction state unless they are excited with a high-energy photon or phonon. At $T=0$, the valence band is completely filled and the conduction band is completely empty. At finite temperature, some electrons populate the conduction band, and some holes populate the valence band.

Semiconductors and insulators are separated from each other by the size of their band gap. By convention,

$$\begin{aligned} \text{SC: } & 0 < E_n \leq 4eV \\ \text{I: } & E_n \geq 4eV \end{aligned} \quad (2.8)$$

Strongly bound excitons are known as Frenkel excitons, and are often found in solids

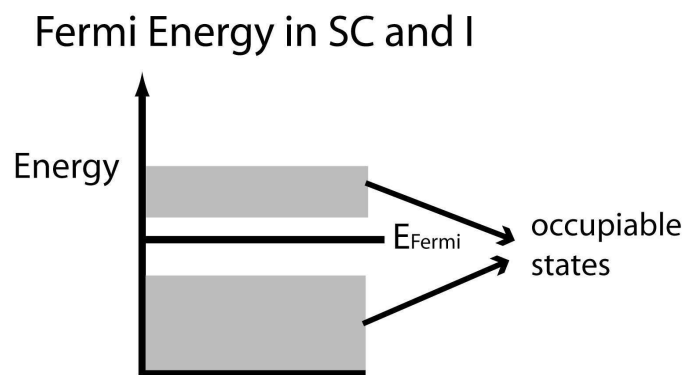


Figure 2-6: General energy diagram for insulators and semiconductors.

in which atoms only weakly interact with each other. This is the type of exciton typically found in insulators. The excitons could, in principle, travel a long way through the material before getting scattered. However, they are usually confined to a single unit cell.

Weakly bound excitons are called Wannier-Mott excitons (more commonly just Wannier excitons) and are found in materials for which the converse is true. These are the excitons most commonly found in semiconductors, which is to say, in more covalent crystals. The electron and hole can undergo many scatterings before they interact with each other. As a result, the exciton is formed out of an effective electron and hole interacting through a Coulomb potential screened by the material's large dielectric constant, which is due to strong charge screening by valence electrons. The curvature of the conduction and valence bands dictate the effective mass of the electron and hole, respectively.

Intermediately bound excitons are generally found in materials that have both some weakly and strongly interacting properties. In particular, the crystal exhibits a somewhat even mix of ionic and covalent bonding.

In this document we will concentrate on Wannier excitons since that is the type typically supported by wurtzite CdSe, the material used in the present experiments. As will soon become apparent, despite weak exciton binding in the bulk, the excitons are more strongly bound in the quantum dot size regime. The energy for strong binding arises from the considerable spatial confinement experienced by the excitons. Detailed examination of bulk exciton binding is warranted before we delve into understanding the effects of strong confinement on excitons.

Working in reciprocal space provides an intuitive picture for transitions in which momentum and energy are conserved. When, for example, a photon is absorbed by an electron in the VB, the momentum imparted by the photon is negligible. Therefore, the electron-hole system, newly created, must have a net momentum no different than the original VB electron.

The momentum of the excited electron is referred to as the crystal momentum, and is denoted as $\hbar\vec{k}$. It is a quasi-momentum for the reasons that it is conserved only for wave vectors in the reduced Brillouin zone, and that the Bloch waves are not proper eigenstates of the momentum operator.³⁹ In order to interpret the physical meaning of the crystal momentum, we need to understand the exciton motion and the effective mass.

Exciton motion is separated into two parts: center of mass (COM) motion, and relative motion. The COM behaves as a particle with a mass equal to the sum of the electron and hole masses.

$$M_{COM} = m_e + m_h. \quad (2.9)$$

The COM momentum is similarly (the \hbar is dropped for simplicity)

$$\vec{k}_{COM} = \vec{k}_e + \vec{k}_h. \quad (2.10)$$

The rotational motion reduced mass is m_r , where

$$\frac{1}{m_r} = \frac{1}{m_e^*} + \frac{1}{m_h^*} \quad (2.11)$$

and the related reduced momentum is

$$\vec{k} = \frac{m_e^* \vec{k}_e - m_h^* \vec{k}_h}{m_e^* + m_h^*}. \quad (2.12)$$

m_e^* and m_h^* are the effective electron and hole mass, respectively. Assuming that the

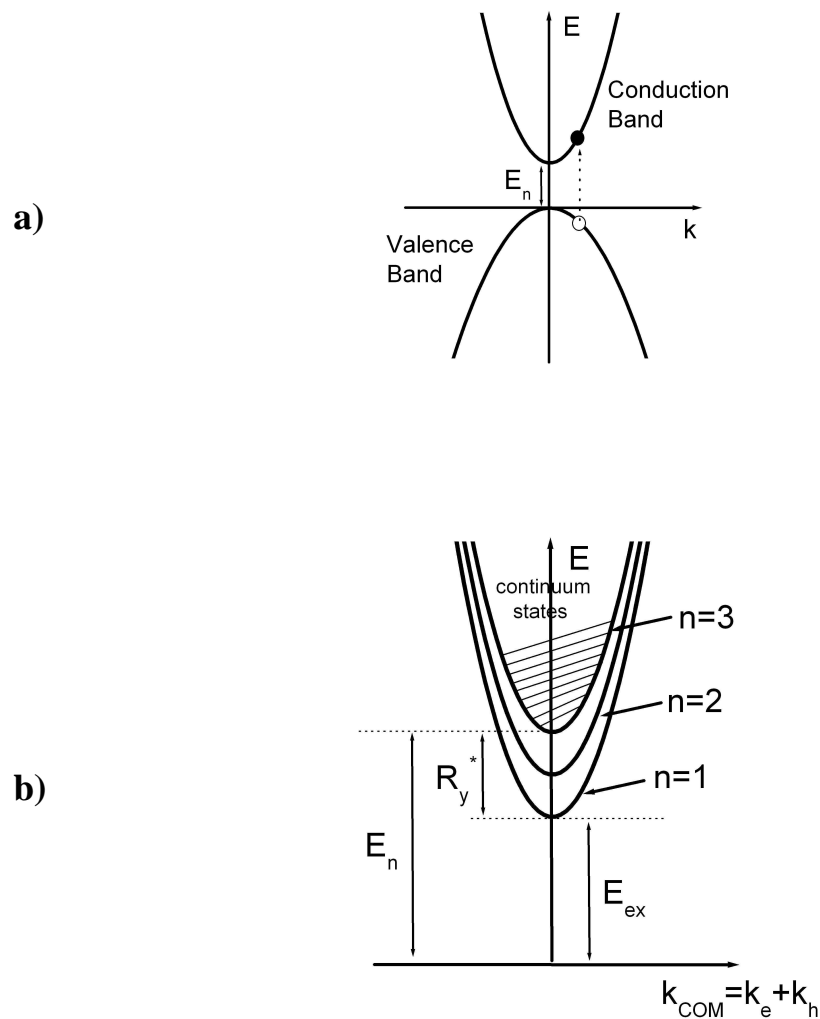


Figure 2-7: a) The single particle picture of an electron and hole in a semiconductor. The electron occupies the conduction band. b) The interaction two-particle picture showing exciton energy level structure in a semiconductor. E_n is the intrinsic band gap of the bulk material.

original valence electron is at rest when it is excited by a photon, $\vec{k}_{COM} = 0$ due to momentum conservation. Note that \vec{k} in Equation 2.12 is a two-particle quantity and differs from the \vec{k} discussed previously for an excited electron (pg. 23). In certain texts the two-particle momentum is denoted as \vec{K} but the majority of the literature uses \vec{k} .

A popular method for finding the energy levels of the system is called the $\vec{k} \cdot \vec{p}$ method, since the $\vec{k} \cdot \vec{p}$ term is eliminated from the Schrödinger equation for the exciton system.⁵⁰ The result is most appropriately applied to conduction band dispersion, since the valence band is complicated by degeneracies and splittings and is also anisotropic. Details of the method are widely available in standard quantum mechanics textbooks.

The result is essentially reduced to the hydrogen atom problem. The eigenenergies are

$$E_n(\vec{k}) = -\frac{m_r e^4}{2\hbar^2 \epsilon^2 n^2} + \frac{\hbar^2 k^2}{2(m_e^* + m_h^*)}. \quad (2.13)$$

Each energy (at each \vec{k}) is labeled by state n. Another way to approach the result is that the exciton energy dispersion is the band gap energy, minus the binding energy, plus any COM kinetic energy contribution that may exist. That is,

$$E_{ex}(n, \vec{k}_{COM}) = E_g - R_y^* \frac{1}{n^2} + \frac{\hbar^2 \vec{k}_{COM}^2}{2M_{COM}}, \quad (2.14)$$

where $n=1,2,3,\dots$ is the principal quantum number, and $R_y^* = 13.6eV * m_r / \epsilon^2$, which is the exciton binding energy. For typical semiconductors, R_y^* is usually much smaller than the width of the band gap.³⁹

In order to obtain a better physical picture of the crystal momentum, it is helpful to consider the effective mass, m^* . It is useful to compare a real electron traveling through a material to an effective electron. The real electron travels erratically among the atoms of the lattice, following a complicated trajectory. Its momentum changes frequently. Eventually, however, it works its way from some point A to some point B. If one draws a vector from A to B, the vector can be considered as the trajectory of the effective electron (see Figure 2-8).

The effective electron does not move as instantaneously fast as the real electron, but behaves in a billiards-like manner. It travels in a straight line with constant momentum, $\hbar\vec{k}$, the *crystal momentum*. The effective electron is unimpeded by the real atoms—it simply experiences an overall mean-field potential and dielectric constant. The effective mass is actually a tensor and depends on the direction in which the electron (or hole or exciton) moves. Defects in the lattice merely alter the potential the electron discerns. The main parameter of the effective electron's apparent motion is its effective mass.

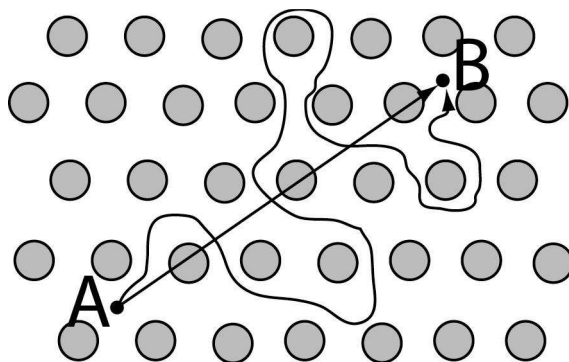


Figure 2-8: The path of a real electron as opposed to that of an effective electron in two dimensions in a triangular lattice.

The effective mass accounts for the consequences of the electron's existence in a potential. Therefore, the mathematics used to describe the effective electron are similar to those for a free electron, differing only in the use of the effective mass.

As mentioned previously, the bands of semiconductors tend to be reasonably parabolic near their extrema. Because the effective mass is set by the curvature of the bands, and the curvature is “flat” near the extrema, the effective masses of carriers are approximately *constant* in the region near the Brillouin zone center. Performing calculations near the zone center with the assumption of constant mass is referred to as the *effective mass approximation* (EMA), and is an appropriate description for Wannier excitons at the band edge of direct gap semiconductors. The use of the EMA is justified because the Bohr radius for an exciton in the material is larger than the lattice constant of the material. The orbits of the electron and hole around their common COM average over many unit cells. The excitonic Bohr radius is the hydrogen Bohr radius modified by the reduced mass and the dielectric constant (ϵ):

$$a_B^{ex} = a_B^H \epsilon / m_r. \quad (2.15)$$

Essentially, all forces from the other electrons and ions in the crystal are bundled into the periodic potential. Any externally applied forces cause the charge carrier, or carriers, to react with an effective mass.

The Hamiltonian for the bound state (Wannier exciton) in the bulk material can be described approximately by a hydrogenic Hamiltonian,⁴⁵

$$H = -\frac{\hbar^2}{2m_h^*} \nabla_h^2 - \frac{\hbar^2}{2m_e^*} \nabla_e^2 - \frac{e^2}{\epsilon |r_e - r_h|}. \quad (2.16)$$

The combination of small effective masses (m_e^* and m_h^*) and weak Coulombic attraction between the electron and hole causes the exciton wave function to extend over a large region. In terms of a hydrogen atom analogy, the band gap is the ionization limit of the hydrogenic electron-hole bound states. Absorption of a photon of sufficiently high energy can promote the exciton to the continuum states above the band gap, meaning that “free” electrons and holes are formed with excess kinetic energy.

Quantum Confinement

There are typical simplifying assumptions used to calculate the exciton energy structure in QDs. The first is to assume a cubic lattice in a perfectly spherical nanocrystal. In addition, only transitions near the band edge, which is to say, near the Brillouin zone center, are considered. Subsequent perturbations to this model based on the lattice

Density of States in a Semiconductor		
D	Prefactor	Energy Dependence
3	$(2m^*)^{2/3} / 2\pi\hbar^3$	$\sqrt{E - E_n} \Theta(E - E_n)$
2	$m^* / \pi\hbar^2$	$\Theta(E - E_n)$
1	$\sqrt{2m^*} / \pi\hbar^2$	$\frac{\Theta(E - E_n)}{\sqrt{E - E_n}}$
0	2	$\delta(E - E_n)$

Table 2-1: DOS for electrons in the conduction band of a semiconductor.⁵¹ D stands for dimension. The 2 in the zero dimension case is just the spin degeneracy, since the volume part of the prefactor no longer exists. $\Theta(E - E_n) = 0$ for $E < E_n$, and 1 for $E > E_n$.

structure and nonsphericity of the dots, among other things, are then included in the calculation to take into account a more realistic representation of the actual quantum dots. These perturbations help account for experimentally observed exciton fine structure.

An appropriate way to approach the subject of low-dimensionality is to explore the properties of the density of states (DOS), a quantity that dictates the oscillator strength of certain transitions. The DOS is derived from the number of states per energy per volume. This calculation is explicitly worked out in many modern solid state physics texts.⁵¹

Table 2-1 shows the DOS for zero to three dimensions. It must be noted that the energy across the gap to the bottom of the conduction band is E_n . The DOS for electrons substitutes $E-E_n$ for E . (For holes in the valence band, E is replaced by E_n-E .) The DOS is zero in the energy gap, so all results are only suitable in the proper region: $E>E_n$ (or $E<0$). The absorption coefficient is proportional to the DOS, which indicates that, as the

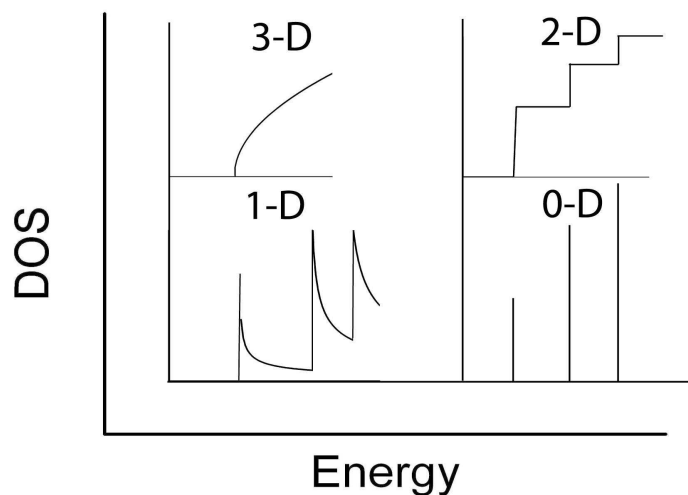


Figure 2-9: Density of state graphs for different dimensions.

dimensionality is reduced, both oscillator strength and absorption become more and more spectrally concentrated. In our case of interest, 0-D, absorption only occurs at very discrete energies. This contrasts sharply with the absorption of bulk materials where the oscillator strength density is uniform throughout k-space. In the bulk, absorption increases rapidly for energies above the band gap.⁴⁵

Exciton confinement may be approached in a qualitative way. The exciton is confined by the band gap difference between the material making up the quantum dot and the material surrounding the dot. The confinement strength for an exciton depends on the

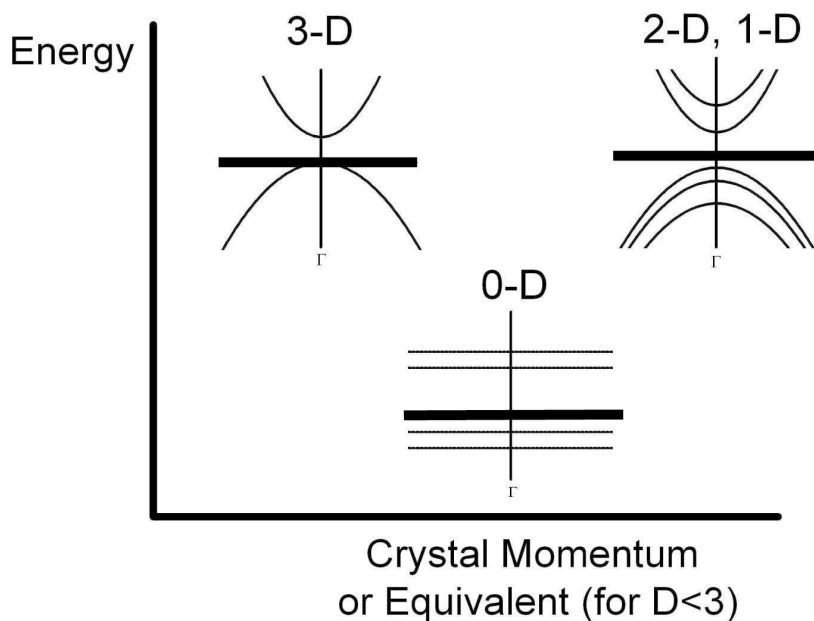


Figure 2-10: Dispersion relations of electrons and holes for different dimensionalities. For all cases, the dispersions above the thick, horizontal zero energy line are for electrons, and the dispersions below are for holes. In the 2-D and 1-D cases, the dispersion shown is for the confined direction(s) only, while the 3-D dispersion can be used for the unconfined direction(s).

Bohr radius of the same exciton in the bulk semiconductor, a_B^{ex} , in conjunction with the size of the dot. Confinement increases the energy difference between the excited and ground states.

Weak confinement occurs when the nanostructure diameter, $2R$, is much larger than a_B^{ex} . In this regime the confinement kinetic energy is smaller than the Coulomb interaction energy between the electron and hole.

When a_B^{ex} and $2R$ are comparable, the exciton exists in the intermediate confinement regime. This is the same as saying the confinement energy, arising from the exchange interaction, is of the same order of magnitude as the Coulomb energy. The intermediate confinement regime is the cross over to the so-called molecular limit.

Strong confinement is the case relevant to most of the samples examined in this dissertation. The electron-hole pair is strongly confined when $2R$ is smaller than a_B^{ex} . (In CdSe, a_B^{ex} is 5.6 nm.) In this regime both carriers are independently confined. The exchange interaction is very strong since the electron and hole wave functions overlap dramatically, and, in fact, the confinement energy is much larger than the direct Coulomb interaction (and opposite in sign). The Wannier exciton can no longer be said to exist since the Wannier Hamiltonian (Equation 2.6) is no longer reasonably accurate. Now an exchange interaction term must be included, and the direct Coulomb term may be neglected. Therefore, when we use the term “excitons” in quantum dots, it is a misnomer and really refers to correlated electron-hole pairs in quantum dots.

The exciton has a series of excited, discrete bound states approaching a bound-pair ionization limit (with increasing principal number n), corresponding to a positively charged nanocrystal and a free electron in vacuum (see Figure 2-7 (b)). However, it must be borne in mind that a nanocrystal is not large enough for the intrinsic material band gap to form; that is, to sustain non-interacting, Bloch-type plane wave electron and hole eigenstates at the band edges. Confinement causes a larger band gap and atomic-like discrete states (see Figure 2-11). Because the electron-hole pairs in CdSe are weakly bound, we consider the energy structure only near the band edges. This simplifies the mathematical description of the exciton energy levels.

In quantum dots, the exciton experiences the potential of a 3-D quantum mechanical square well. Because we overcoat our quantum dots with a larger band gap semiconductor the excitons are in a finite potential well and can experience a small amount of wave function leakage outside the core of the dot, leading to a larger effective dot size. Chapter Three contains more information about this phenomenon. As indicated in Figure 2-11, energy bands for electrons in the CB and holes in the VB break up into discrete, atomic-like levels in the 0-D case.

In a potential well with infinitely high barriers,

$$E_n = \frac{\hbar^2 \pi^2}{2m_{e,h}^* (2R)^2 n^2}, \quad n = 1, 2, 3, \dots \quad (2.17)$$

There are an infinite number of bound states. R is the half-width of the well (or the radius of the nanocrystal). In a real QD structure, there are a finite number of bound states. To a

good approximation, they still follow the n^{-2} law.³⁹ As $R \rightarrow 0$, E_n diverges. In a real structure, the states converge to the Bloch states of the barrier material; in our case those of ZnS.

Since the ground state energy is now larger than the intrinsic band gap, we can readily see that confinement increases the energy of the exciton system. The exciton experiences an enhanced Coulomb (attractive, in this case) interaction. In particular, the exchange interaction plays a very large role in the energy levels of strongly confined excitons.

The exciton energy level structure consists of the transitions between discrete quantum levels of the electrons and holes. The first approximation that we made, that CdSe is a zinc-blende material, has the result⁵² that multiband effective mass theory that takes VB degeneracy into account successfully describes most aspects of the spectra obtained spectroscopically. However, some of the excitation spectral features are not explained by this theory. In particular, the photoluminescence (PL) of CdSe QDs is redshifted relative to the excitation frequency. This Stokes shift (defined shortly) of the

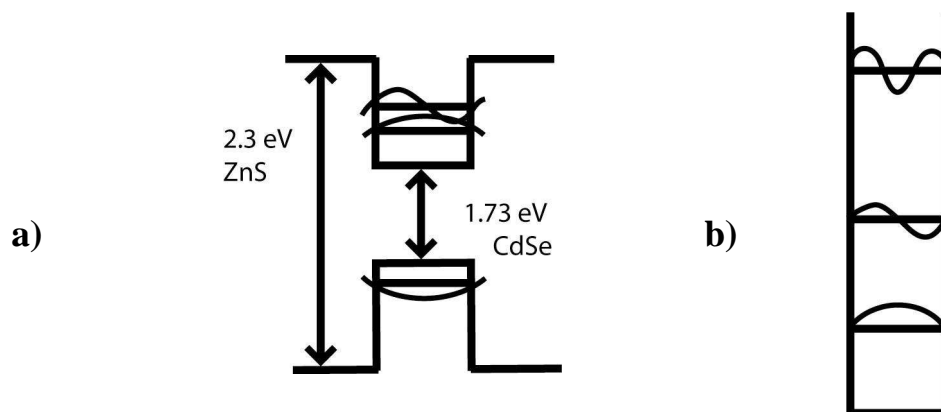


Figure 2-11: (a) Discrete energy levels in a CdSe quantum dot. Wave functions are shown for the states shown.^{9,12} The listed CdSe band gap is the intrinsic band gap value at room temperature. At low temperature the value is 1.84 eV. (b) Energy levels in a perfect square well with infinitely high potential barriers.

PL with respect to the first absorption peak is very large far from the band edge, while at the band edge (near the Γ -point) it is much smaller. Additionally, the exciton has an unexpectedly long radiative lifetime ($\sim 1 \mu\text{s}$ at 10 K) compared to the bulk ($\sim 1 \text{ ns}$).

In a resonant excitation experiment, where pumping takes place at the band edge energy, transitions associated with the lowest bright state ($|F| = 1$) are probed.⁴² As will be discussed in Chapter Four, we resonantly excite excitons in our sample while undertaking spectral hole burning experiments. Excitons formed in the lowest bright state thermalize to the exciton ground state, which is a dark (optically passive) state. This will be explored further shortly. The Stokes shift in this case is the difference in energy between the lowest active state and the dark ground state.⁵² The Stokes shift increases with decreasing size. However, in order to take luminescence data, we excite at an energy well above the band edge. This is the so-called nonresonant case. The nonresonant Stokes shift is the difference in energy between the lowest energy peak of the absorption and the peak of the full, inhomogeneously broadened photoluminescence (PL). The PL is inhomogeneously broadened because there is a contribution from every QD in the ensemble sample, which typically contains a variety of QD sizes.

Energy level structures in quantum dots

Let us set out the starting point to which we will introduce perturbations. We have a perfectly spherical CdSe QD. We use the quasi-cubic model to describe the lattice, and the structure size is small enough that excitons are in the strong confinement regime. The exciton ground state of the spherically symmetric dot is denoted $1S_e1S_{h,3/2}$, and is eightfold degenerate.

As intimated by the previous mention of optical transitions that lift an electron from the VB to the CB, dipole transitions between VB and CB are allowed. Dipole transitions are allowed due to the p- and s-type character of the VB and CB, respectively.

In the strong confinement regime, electron and hole wave functions are modified spherical harmonics. The carrier energy levels are similar to those discussed for the bulk material, except that they are proportional to the inverse square of the dot size, which emphasizes the effects of confinement energy. We also assume, in our first order approximation, that the VB is unaffected by k and k^3 terms arising from the inversion symmetry of the zinc-blende lattice, among other causes, and that both the CB and VB are parabolic. Throughout this section we rely heavily on Reference 52 as the description found there is exceptionally well-suited to our CdSe QD system.

Splitting caused by hexagonal lattice structure

The fact that the lattice is, in fact, hexagonal rather than cubic is a perturbation that helps split the fourfold degenerate hole state into two twofold degenerate states having angular momentum projections, $|L|$, of $\pm 1/2$ and $\pm 3/2$. Δ_{CF} in Figure 2-4 (a) shows the crystal field splitting associated with the hexagonal lattice. The value of the splitting as a perturbation is

$$\Delta_{\text{int}} = \Delta_{CF} \nu(\beta), \quad (2.18)$$

where $\Delta_{CF} = 25$ meV in CdSe and $\nu(\beta)$ is a dimensionless function that describes the strength of Δ_{int} as a function of the ratio of light hole to heavy hole effective masses. Δ_{int} does not depend on the QD size. $|L| = 3/2$ is the ground state.

Splitting caused by nonsphericity of a QD

The specific case of prolate nonsphericity is important for our eventual focus on nanorods. Prolateness means that the extent of the dot in the \vec{c} -axis direction is larger than the extent of the dot in the direction perpendicular to the \vec{c} -axis. A nanorod is an extremely prolate nanocrystal.

QD nonsphericity also has the effect of splitting the fourfold degenerate VB into two twofold degenerate bands. The nonspherical shape is modeled as an ellipsoid. The deviation from sphericity is defined as the ratio of the length of the major to minor axes, which equals $1+\mu$, where μ is the ellipticity. Nonsphericity gives rise to splitting

$$\Delta_{nonsph} = 2\mu u(\beta)E_{3/2}(\beta) \quad (2.19)$$

where $E_{3/2}$ is the $1S_{h,3/2}$ ground state hole energy for spherical crystals whose radius, R , is

$$R = (b^2c)^{1/3}. \quad (2.20)$$

The minor and major axis lengths are b and c , respectively. u is another function dependent on the ratio of light hole to heavy hole effective masses. u is negative in CdSe. Since $E_{3/2}$ is proportional to the inverse square of the QD radius, Δ_{nonsph} is sensitive to QD size. The net splitting decreases with increasing size in prolate ($\mu>0$) QDs.

The net splitting of the hole state is

$$\Delta_{hole} = \Delta_{nonsph} + \Delta_{int}. \quad (2.21)$$

Effect of electron-hole exchange interaction

The exchange interaction drastically alters the energy level structure in QDs from that of the bulk. The exchange interaction has two main consequences for the EMA theory: along with the nonsphericity and crystal field, it also breaks the eightfold degeneracy of the spherical band edge exciton, and, of particular import, it mixes different electron and hole states.

The Hamiltonian for the exchange interaction is written

$$H_{exch} = -\left(\frac{2}{3}\right) \varepsilon_{exch} a_0^3 \delta(\vec{r}_e - \vec{r}_h) (\boldsymbol{\sigma} \cdot \boldsymbol{J}) \quad (2.22)$$

where ε_{exch} is the exchange strength constant, a_0 is the lattice constant, $\boldsymbol{\sigma}$ is the electron spin-1/2 Pauli matrix, and \boldsymbol{J} is the hole spin-3/2 matrix.

In the cubic lattice EMA theory, in the bulk material, this exchange term alone splits the eightfold degenerate exciton ground state into a fivefold degenerate optically passive (dark) state with total angular momentum 2, and a threefold degenerate optically active (bright) state with total angular momentum 1. This splitting is expressed in terms of the bulk exciton Bohr radius a_B^{ex} as

$$\hbar\omega_{ST} = \left(\frac{8}{3\pi}\right) \left(\frac{a_0}{a_B^{ex}}\right)^3 \varepsilon_{exch}. \quad (2.23)$$

When the hexagonal lattice is included (in the bulk), this term instead splits into a triplet and singlet, separated by

$$\hbar\omega_{ST} = \left(\frac{2}{\pi}\right) \left(\frac{a_0}{a_B^{ex}}\right)^3 \varepsilon_{exch}. \quad (2.24)$$

In CdSe QDs, $\hbar\omega_{ST}=0.13$ meV and $\varepsilon_{exch}=450$ meV (for $a_B^{ex}=5.6$ nm).

Net effect

With all three effects taken into account, the hexagonal lattice, nonsphericity, and exchange interaction, the original eightfold degenerate exciton has been split into a total of five states. Each state is labeled by exciton total angular momentum projection, $F = L + s_z$. Figure 2-12 shows the size dependence of these levels. Both the exchange interaction and nonsphericity have size dependencies that play into the net picture.

How perturbations affect empirical exciton fine structure

Optical transition probabilities are strongly affected by exchange interaction-induced mixing of the electron and hole states. However, the optically passive $|F|=2$ exciton states are unaffected by this mixing. These states are passive in the optical transition (in the dipole approximation) because photons cannot carry an angular momentum of ± 2 . In the bulk this is the fivefold degenerate ground state.

In the strong confinement regime, the splitting of the exciton levels can be considered a perturbation to the exchange interaction, which grows as $1/R^3$. In this case, the wave functions of the $\pm 1^L, 0^L$, and ± 2 exciton states turn into the wave functions of the optically passive exciton with total angular momentum 2. The wave functions of the $\pm 1^U$

and 0^U exciton states become those of the optically active exciton states with total angular momentum 1. The active states carry nearly all the oscillator strength.

Optical recombination of the dark state is possible through the application of a magnetic field. The field mixes dark and light states. In zero field, the exciton lifetime is very long since the only recombination pathways are through LO phonon-assisted or spin-flip assisted transitions. Recall that in the dipole approximation the lifetime of the exciton in the dark state is infinite.

Energy level structures in nanorods

Nanorods are cylindrically shaped nanocrystals in which strong confinement is

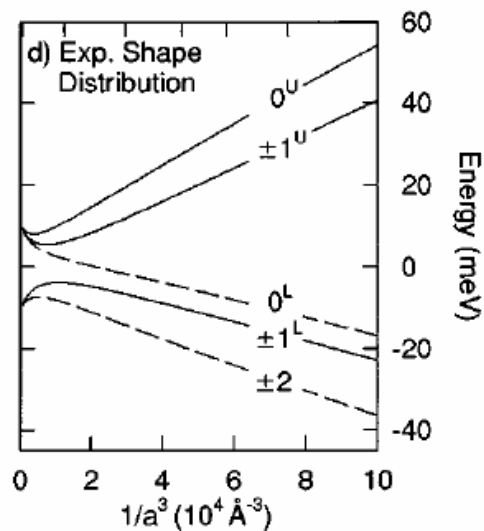


Figure 2-12: Size dependence of the exciton band edge structure in ellipsoidal hexagonal CdSe QD with ellipticity taken to be prolate, where the size dependent ellipticity function is determined empirically. Source: Reference 52. The dashed lines represent dark states, while the solid lines represent bright states. The numbers are total angular momentum values, and U and L mean upper and lower (related to the sign conventions of the mathematical expressions for the plotted states). The dot radius is denoted a . The important thing to notice is that the lowest energy exciton state is dark.

maintained in two directions. However, due to elongation of the third direction, confinement in that direction is weaker. Both radius and length can play a role in nanorod optical and electrical properties.⁵³ Nanorods are the experimental realization of the transition from 0-D to 1-D nanostructures. The most often explored nanorod energy level structure theories have been modified nanowire theories^{35,53-55}, and arise from either multiband effective mass theory or pseudo potential theory. The two approaches usually yield similar results.

Nanorods have different optical properties than spherical quantum dots, particularly: their emission is highly linearly polarized;^{35,54} their transitions (which control oscillator strength) are essentially dependent on 1-D excitons,^{35,36} their lifetimes are shorter;^{35,56} they have higher PL efficiency;³² they have an increased global Stokes shift;⁵⁴ they have a permanent electric dipole moment;³⁶ and, as we will see in Chapter Six, the zero phonon transition has different dependencies on spectral diffusion and pumping intensity than QDs. The linearly polarized emission property has garnered the most interest in terms of its applicability to low-power lasers and other devices.^{36,54,55}

Linearly polarized emission is largely attributable to the dominant presence of 1-D excitons in nanorods, a phenomenon which itself is promoted by dielectric confinement.³⁵ 1-D excitons form along the long axis of the nanorod.^{35,36,57,58} 0-D excitons, as are found in QDs, are less energetically favorable due to their higher confinement energy and so are less likely to form if the 1-D morphology is present. It is reasonable that in a non-ideal rod structure excitons experience some localization and location-hopping within the rod. This will be discussed in greater detail in Chapter Six.

In 1-D the band gap of CdSe is insensitive to the length of the rod. When the length is reduced until this sensitivity appears, the nanocrystal can no longer be considered identically one-dimensional. The transition takes place when the length of the rod and the Bohr radius of the 1-D exciton become comparable.⁵⁷

The presence of length insensitivity for a particular range of rod optical transitions has sometimes led to the conclusion that for most CdSe nanorods, radius is more important than length for determining exciton fine structure.⁵⁵ The presence of 1-D excitons, as opposed to 0-D excitons, actually has a larger overall effect. Additionally, there is a critical radius (3.7 nm, such that the diameter is a little larger than a_B^{ex}) above which the 1-D exciton ground state is dark, like in spherical CdSe nanocrystals, and below which the ground state becomes optically active.³⁶ This state switching phenomenon is based on the one-dimensional exchange interaction.

In the case of cylindrical quantum wires, the VB states are admixtures of $S_{h,1/2}$ and $S_{h,3/2}$ (light and heavy hole) states.⁵⁸ Recall that before any modifications are made, the VB of a cubic structure spherical QD is degenerate. Distorting the shape of the crystal into a flattened sphere shape breaks the degeneracy. Roughly, the heavy hole states move lower in energy while the light hole states move higher. If the oblate shape is now elongated along one direction, rotational symmetry is broken and the resultant shape may be used as a model for a nanorod. The elongation mixes the heavy hole and light hole ($F_z = \pm 3/2$ and $F_z = \pm 1/2$) states. The exchange interaction is the mechanism by which the fourfold degenerate ground $S_{h,1/2}$ state is broken (in the proper radial range) and is

represented by Equation 2.22 in conjunction with Equation 2.24. The ground state is the $S_{h,1/2} F_z = 0$ state below the critical radius, and is the $S_{h,3/2} F_z = \pm 2$ above it.³⁶ The $F_z = \pm 3/2, \pm 1/2$ states are split into two twofold degenerate bands by quantum confinement. Neglecting any coupling between electron states and the VB, the electron states are not modified by the shape distortion.

The heavy hole ($S_{h,3/2}$) exciton has split into an optically active ± 1 state and a forbidden ± 2 state, which is the ground state for $r > r_c$. All the states have a size dependence on the radial extent of the rod; the heavy hole-like states have the steepest dependence. At about (depending on the particular states) the critical radius, as r is reduced, the $S_{h,3/2} F_z = \pm 2, \pm 1$ states intersect the $S_{h,1/2} F_z = 0^U, \pm 1, 0^L$ states. This is the radius at which the ground state switches. Instead of $S_{h,3/2} F_z = \pm 2$, it is now $S_{h,1/2} F_z = 0$. The different ground state leads to longer decay times for PL from rods with radii below r_c , as observed experimentally.^{36,56} The angular momenta of the states are all projected along the long axis of the rod.

Shabaev and Efros describe the recombination of electrons and holes within the six-band model used for QDs.³⁵ They find that the *linearly* polarized emission is from the upper 1-D exciton sublevels. As these levels become depopulated at lower temperature, the PL is expected to become less polarized. Experimental studies published to date on linearly polarized emission from nanorods have not yet addressed this prediction.

The shorter radiative lifetime experienced by excitons in nanorods, as compared with QDs, can be ascribed to three different factors. These are: 1) an enhanced electron-hole Coulomb interaction that reduces the exciton's size (and increases the probability for recombination). 2) An exciton localized near a nanorod's center has an especially large oscillator strength. Localization near the center is an artifact of the ellipsoidal model used, in which the center of the rod has a larger radius than any other part of the rod. This variety of localization contributes to the recombination probability of the exciton. 3) Finally, there is a lack of dielectric screening for photons. If photons are not screened the emission of photons by dipoles parallel to the rod long axis is favored, which dovetails with the available transition states of 1-D excitons.

Next, we examine the fabrication of both dots and rods by chemical means. The experimental setup and saturation absorption spectroscopy are explained after that.

CHAPTER 3

NANOCRYSTAL AND NANOROD SYNTHESIS AND CHARACTERIZATION

This chapter gathers, discusses, and relays methods of growing and characterizing CdSe/ZnS core/shell nanocrystals. Many fine points are not covered here, but this chapter should provide a starting point on how to synthesize and characterize nanocrystals. Appendices A and B give extensive detail on the procedures of growing quantum dots and nanorods, respectively, and should be used for reference. They are written in a “teaching” format, in the event that another student wishes to produce nanocrystals themselves. The order to be followed begins with a synopsis of the fabrication of the CdSe stock solution followed by the procedure for fabrication of the ZnS stock solution. Next the synthesis of the nanocrystals is discussed, with the purification and size selection procedures explained in brief. This chapter, in keeping with the synthetic method, contains descriptions and uses of various characterization techniques such as absorption, photoluminescence, and Transmission Electron Microscope (TEM) imaging, while explaining the effects of different parameters on nanocrystal growth.

Nanocrystal synthesis

Semiconductor nanocrystals, used for the experiments discussed presently, are grown in a hot liquid solution. The resulting crystals are *colloidal* which means that they are within the nm to μm size range and are suspended in another media or a different phase

of the same material as the crystals. The crystallites nucleate at high temperature from liquid precursors. The advantages of colloidal nanocrystals over self-assembled dots are their dispersability and easy placement on many substrates or in a variety of matrices with any concentration of nanostructures. Additionally, through an annealing process and the presence of a shell, surface defects are reduced around the core of the nanocrystal.⁵⁹ Due to the crystals' spherical shape, the annealing process, and lack of wetting layer (a by-product of molecular beam epitaxy consisting of extraneous atoms in unintended locations) directly outside the dots, strains at the nanocrystals' surface are capable of being higher than in self-assembled QDs without detriment to the quality of the QD.

Nanorods, which are nanocrystals that have grown into a cylindrical rather than a spherical shape, are sensitive to similar defects. It has been demonstrated⁶⁰ that a shell layer covering the core of the nanorod elongates the decay time of higher energy states by a factor of 2.5 (200 fs versus 500 fs). The relationship between the presence of a shell and decay time is due to the remediation of unpassivated surface states that cause carrier trapping.

The radius and shape of nanocrystals are controlled by nucleation and growth temperatures, the monomer density, and by both the specific stock solution chemicals and growth medium. A variety of shapes can be synthesized^{31,61-63}, but spheres with radii between 2 and 4.5 nm and rods with *aspect ratios* in the range 2.2-9.17 have been the current focus.

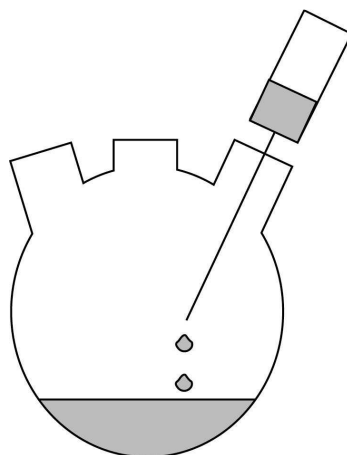


Figure 3-1: Colloidal nanocrystals nucleate out of a liquid solution containing precursor materials. Nucleation occurs at a high temperature and growth at a somewhat lower temperature to reduce the incidence of new nanocrystal formation after the initial nucleation stage.

The synthesis requires two stock solutions, one of which contains the precursor materials for the core of the nanocrystals (cadmium selenide, CdSe), while the other contains the materials for the shell of the nanocrystals (zinc sulfide, ZnS). The cores are grown first, and when completed, shells are grown on the outside to encapsulate the cores. The resulting crystals are nearly spherical with aspect ratios in the range 1.1-1.3, although larger crystals exhibit some prolateness and faceting.

Two elements of the synthesis specifically protect the quality of the nanocrystals. First, the synthesis of the nanocrystals is an air-free process that shields the materials from oxygen. Specific procedures are detailed in the Nanocrystal Synthesis section provided in Appendix A. The Schlenk line and glove box sections of a chemistry techniques manual provides further information on air-free techniques.

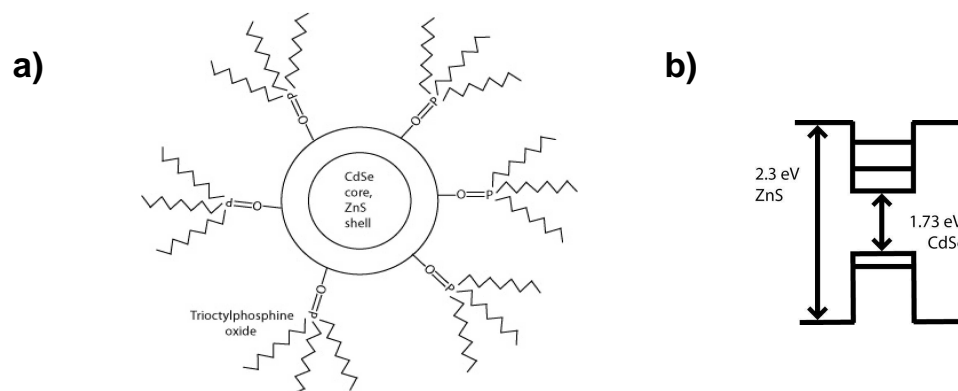


Figure 3-2: a) Colloidal CdSe/ZnS core-shell nanocrystal with a ligand shell made up of trioctylphosphine oxide. The core has a wurtzite structure. b) Bandgaps of the core and shell materials.

Second, the shell layer protects the nanocrystals after synthesis. The shell layer is not strictly necessary because the uncapped cores luminesce. Uncapped cores are usually referred to as “bare” despite the usual organic ligand shell. In our samples, this ligand shell is TOPO (trioctylphosphine oxide). The ligand shell prevents aggregation of the nanocrystals in the solvent. The semiconductor shell (in our case ZnS) is important for passivating core surface defects. The presence of the shell improves the quality (e.g., quantum yield) and the shelf life of the sample. The shell protects the core from the degrading effects of oxygen, and, once annealed, helps reduce the number of surface trapping states on the core. We choose to grow shells of a much larger bandgap semiconductor than the cores, reasoning that the shell’s optical behavior does not significantly affect the quantum dot core behavior, and that the shell provides an acceptably “stiff” wall for better confinement of charges (in the quantum mechanical potential well sense).

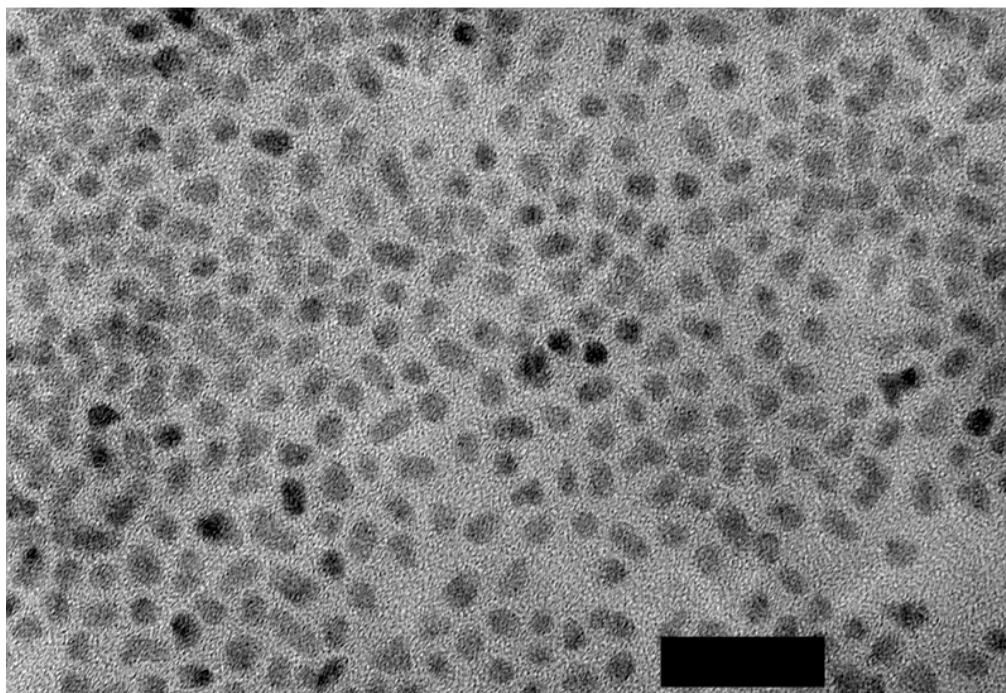


Figure 3-3: TEM image of CdSe/ZnS core/shell nanocrystals. TEM magnification used was 430 kx, and the voltage used was 120 keV. The scale bar represents 20 nm. Note that some crystals are slightly more prolate than others.

The synthesis procedures used in this study to produce spherical nanocrystals are similar to those developed by Xudong Fan and Mark Loneragan⁶⁴ who worked from earlier papers.^{26,59,65,66} Additionally, for this project, changes were made to the nanocrystal growth process (following Mokari and Banin²⁸), so that nanorods could be produced.

Synthesis process

The stock solutions are made at room temperature in an air-free environment. Table 3-1 lists the components of each stock solution. For each solution, some amount of TOP is transferred to the storage vessel, the other two ingredients are added, and then the remainder of the TOP is added. Finally, the solution is stored in a nitrogen-purged storage

vessel, at room temperature, in the dark in order to avoid photo-induced degradation or nucleation. Both air and light can degrade the solutions. In general, the CdSe stock solution degrades much faster than the ZnS stock solution. Precipitates form in it after a few days to weeks, depending on how well it has been stored. The remainder of the solution may still be used, but with lower quality results as time passes.

Nanocrystals are made using organometallic synthesis. As mentioned previously, the crystallites nucleate from liquid precursors at high temperature. The rate of growth and final size are controlled by temperature and the monomer density of the stock materials in the organic solvent. The nucleation process is dictated by the surface area to volume ratio. A free energy barrier must be overcome in order to form a stable, consistently enlarging, core (see Figure 3-4).

A lot of energy is associated with forming the first little bit of surface. In the growth process of a nanocrystal, an elevated growth solution temperature (typically about 360°C) is used to provide the energetic push needed to send the initial core stage over the free energy barrier that has a maximum at r_c , the critical radius. The crystallites formed at high

CdSe core stock solution ingredients	ZnS shell stock solution ingredients
24 mL trioctylphosphine (TOP)	24 mL trioctylphosphine (TOP)
0.2 g selenium	0.52 mL hexamethyldisilathiane
0.25 mL dimethyl cadmium	3.5 mL dimethyl zinc

Table 3-1: Materials used in stock solution fabrication.

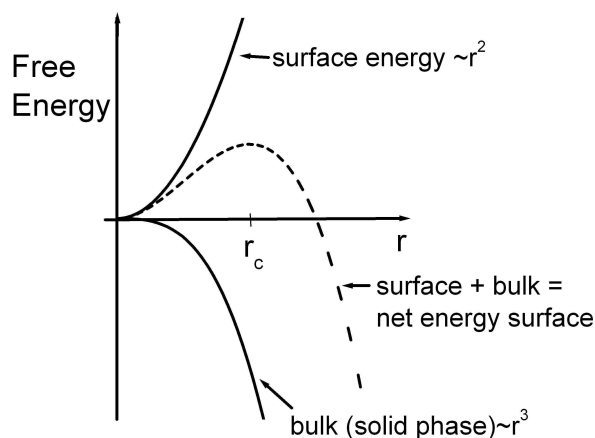


Figure 3-4: The dashed line represents the actual energy landscape that a nucleating drop or crystal must transition through as it grows. There is an initial energy barrier that must be overcome in order for the nanocrystal to consistently grow, as opposed to dissolving back into the liquid. The critical radius, at which continued growth is nominally ensured, is denoted r_c on the figure.

temperatures are larger than r_c , and so are more likely to accumulate atoms than to lose them. The temperature of the growth solution is lowered by 40-60°C after the initial injection of stock solution (for a temperature of ~300°C).

Our emphasis has been to grow larger, rather than smaller, nanocrystals that fluoresce more to the red. By doing so, we have ensured that the absorption curve of the nanocrystals is accessible to the lasers available in the lab.

If one were simply to inject all the core materials at once into the growth medium, then the growth rate of the nanocrystals would be quick at first, and then slow due to an exhaustion of the monomer (e.g., Cd and Se atoms) supply still free in the growth solution. Only large or small CdSe nanocrystals remain in the solution. Atoms are continually leaving and adhering to the surfaces of the nanocrystal cores at a rate dictated by the temperature. Larger crystals tend to capture (and keep) more atoms due to their greater surface area. At this stage, when there are essentially only large and small crystals

left in the solution, gaining and losing atoms from their surfaces, Ostwald ripening becomes the dominant growth process. Ostwald ripening is a thermodynamic competition between the growth of larger crystals and the dissolution of smaller (less stable) crystals.⁶⁷ In particular, the larger nanocrystals must cannibalize the atoms from smaller crystals in order to continue growing. Figure 3-5 provides an experimental demonstration of this effect. This type of growth of average nanocrystal size is a slow process. In order to hasten growth, Xudong Fan found that four equal injections of stock solution several minutes apart reduced the growth time of large nanocrystals considerably by providing fresh monomers.⁶⁴

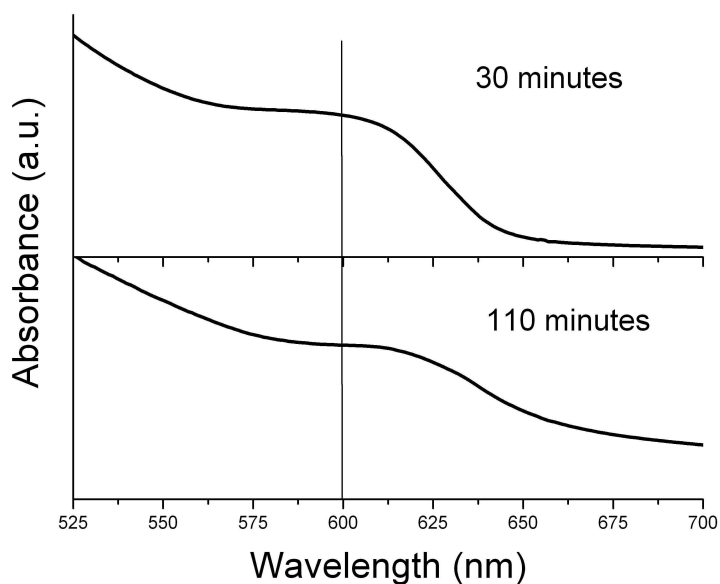


Figure 3-5: Ostwald ripening demonstrated through absorption spectra of uncapped nanocrystals cooked at 280°C for (top curve) 30 minutes and (bottom curve) 110 minutes. Note that the peak moves to the red (larger crystals) with time. The size distribution also increases, as is evidenced by the broadening of the absorption. No additional injections of stock solution were made between these two aliquots of the sample. The vertical line is a guide for the eye.

I have developed an even faster growth method. Instead of a few large injections, I inject one quarter, or less, of the material quickly, then inject the rest of the stock solution dropwise with one drop every ten seconds. The total process takes about 20 minutes, while the process developed by Dr. Fan took up to several hours and sometimes required overnight growth with frequent monitoring.

We usually have a particular luminescence wavelength in mind when we set out to grow a batch of nanocrystals. In order to grow a batch of nanocrystals that luminesce at approximately that value, we can manipulate the timing of stock solution injection, change the amount of solvent in which the nanocrystals are grown (in this case, trioctylphosphine oxide; this affects the monomer density), or we can alter the temperature. The size of the growing nanocrystals is monitored using a UV-vis spectrometer, which irradiates aliquots of the sample in the ultraviolet through visible range and collects the absorption spectrum. (Taking small samples from the growth batch for characterization is called “taking aliquots.”) As the crystals grow larger, the luminescence peak moves to the red. It is important to remember that absorption and photoluminescent emission are offset by an (approximately) 15-30 nm Stoke’s shift, and that photoluminescence will be to the red, the longer wavelength side, of absorption.

We can use the otherwise detrimental Ostwald ripening growth dynamic to our advantage in order to tighten the size distribution of the nanocrystals at the end of the growth process. To do this, we quickly inject a very small amount of stock solution (about 0.2 mL) and then lower the temperature to $\sim 280^{\circ}\text{C}$. This works well because small crystals can add radius (which is to say, volume) more quickly than large crystals with the same monomer availability, and during this stage, the size of the small crystals can catch up to the size of the large crystals.

The addition of a shell when the anticipated size is reached does not shift the absorption peak noticeably, and helps prevent further Ostwald ripening of the cores by removing access from the growth solution to the core atoms (see Figure 3-9). For very monodisperse samples there is a small redshift associated with the addition of the shell. It is caused by a little bit of carrier wave function leaking into the shell layer which results in an effective increase of the quantum dot's size.

For shell growth, the solution temperature is lowered by approximately 80°C from the core nucleation temperature. As already mentioned, this temperature is often 280°C. The shell stock solution is added dropwise, to prevent providing a stock-material monomer density high enough to cause new ZnS nanocrystals to form, even at a low temperature. Drops may be spaced closely in time, however, if the growth solution is rapidly stirred. The newly added Zn and S monomers find it energetically favorable to adhere to the outside of the already-formed CdSe cores in a process of heterogeneous nucleation. Thus, a shell layer is created that overcoats the core of the nanocrystal. The shell's outside surface is, in turn, passivated by TOPO molecules.

Finally, the solution is allowed to anneal at 100°C for one to two hours. This gives the atoms both the thermal energy and time to rearrange themselves into their most stable (lowest energy) states in relation to their surroundings. In particular, the strain and surface defects at the interface between the core and shell materials are reduced to their lowest levels.

The nanocrystals are subsequently purified in order to remove extraneous stock solution material and growth solution material before the batch is stored. The process is detailed in Appendix A.

Once growth is complete, the average size and size distribution of a nanocrystal batch is determined by using the UV-vis spectrometer to confirm the absorption peak, and by measuring the width and peak value of the photoluminescence (PL) spectrum. PL is preferred for analyzing the size distribution since its background noise levels are lower than in the absorption measurements. The width of the PL spectrum corresponds roughly to the size distribution width. At high nanocrystal density, dipole-dipole energy transfer between crystals can broaden the PL spectrum.⁶⁸ To reduce the size distribution, it is recommended that the nanocrystals are reprecipitated with methanol and subsequently centrifuged and redispersed with chloroform two or three more times. For best reduction in size dispersity, a similar amount of the two solvents should be used. (For example, a generally successful ratio is 1:2 (volume/volume) chloroform:methanol mixed vigorously in the sample vial.) During centrifugation, smaller crystals stay suspended in the chloroform longer than large crystals, so short centrifugation times will allow relatively small crystals to be removed from the batch while larger crystals are precipitated out of solution. The supernatant may be centrifuged much longer on its own to recover the smaller specimens from the batch. The nanocrystals may now be stored in chloroform, under an inert atmosphere, and in the dark to prevent photo-degradation.

Nanocrystal batches

The following are tables of the parameters used in the synthesis of a representative sample of spherical nanocrystal batches. It is instructive to note the relationship of the eventual size and PL peak location of the nanocrystals. The volumes of materials and the temperature at different steps are also important to note.

Batch	Amt. CdSe Stock Solution (mL)	Temperature of initial injection (°C)	Time between last stock and first shell injection
ST-119-1	1.2	302, dropped to 290	≈ 20 min
ST-115-2	1.0	{presume 320}	≈ 20 min
ST-119-2	1.2	320	≈ 10 min

Table 3-2: Parameters for representative batches of spherical nanocrystal cores.

Batch	Amt. ZnS Stock Solution (mL)	Temperature of initial injection (°C)	Annealing Time (min)
ST-119-1	3	230	70
ST-115-2	3.3	{presume ≈ 280}	120
ST-119-2	3	{presume ≈ 280}	75

Table 3-3: Shell growth parameters for representative batches of spherical core/shell nanocrystals.

Batch	Total Diameter (nm)	Room Temp. Absorption (nm)	Room Temp. PL (nm)	Low (Liquid He) Temp. PL (nm)
ST-119-1	5.0	610	643	640
ST-115-2	4.5	580	618	610
ST-119-2	3.9	565	595	592

Table 3-4: Size versus absorption and PL for a representative sample of spherical nanocrystals.



Figure 3-6: CdSe nanorods. TEM magnification was 340 kx and voltage was 120 keV. The scale bar represents 20 nm.

Synthesizing nanorods

Largely based on Mokari and Banin²⁸, we have synthesized CdSe/ZnS core/shell nanorods with a range of aspect ratios 2.2-9.17 (see Figure 3-6). The synthesis is very similar to that described earlier for spherical nanocrystals. One major and notable difference is that the core stock solution contains a much higher concentration of precursor materials. These materials, due to their high concentration, appear to start forming small, undirected molecules on their own within a few days of stock solution creation. Under nanoparticle growth conditions, these pre-formed molecules promote growth in several directions, but not uniformly, so that no well-shaped cylindrical cores are produced. These particles do not produce luminescence and appear black to the eye, while properly made nanorods appear brown or red to the eye under white light due to their colloidal size (and consistent size within the batch). TEMs of these malformed particles show a range of shapes, from knobby spheres to branching rods (see Figure 3-7).

The practical result of this tendency is that high-quality nanorods may only be grown using a freshly-made core stock solution. It appears that the limit on the amount of time the core stock solution may remain unused is about four to five days after production.

Two other major differences between nanorod and nanocrystal growth are the addition of a long-chain phosphonic acid to the TOPO solvent, which induces preferential growth along the c-axis of the nanocrystal, and a partial ligand exchange of the TOPO

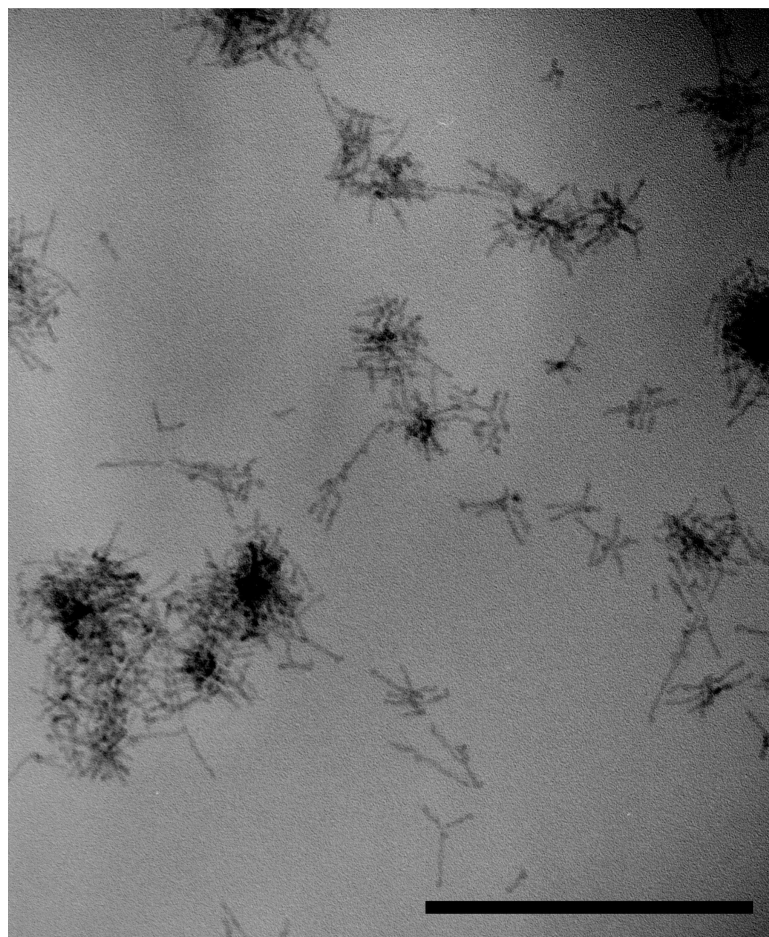


Figure 3-7: Nanorods batch 7. Notice the forked appearance of some rods, and the scraggly, messy appearance of the total collection of rods. TEM magnification was 160 kx and voltage was 120 keV. Scale bar length represents 20 nm.

with an amine ligand following core-growth and before shell growth. The ligand exchange helps produce a better quantum yield from the rods. Appendix B covers the list of ingredients for the nanorod core stock solution. It also provides a brief synopsis of the steps of the synthesis because they are a little different than those used for nanocrystal growth.

TEM images of NRs reveal cylindrically-shaped particles. The aspect ratio can vary within a batch, primarily in the length direction. PL profiles are typically broad for rods. This broadening may be ascribed to physical size-related inhomogeneous broadening due to variation in both rod dimensions (radius and length).

Characterization of the brand-new nanocrystals

Nanocrystals are characterized in terms of their size, shape, photoluminescence, absorption profile, and quality. A transmission electron microscope operating at 120 keV is appropriate for noting the size and shape, and, with proper focusing and astigmatism control, can reveal the actual crystal planes. Linear spectroscopy gives values of absorption and photoluminescence intensities versus wavelength (which indicates size as well) and quantum yield, which is an indication of quality. The size distribution is directly tied to the photoluminescence curve's FWHM. Quantum yield is defined as the ratio of the emitted photon flux to the incident photon flux. The quantum dots synthesized by the above method typically have a quantum yield approaching 100%.

Absorption

Figure 3-8 presents two nanocrystal absorption spectra. The graph on the top (fig. a) represents a batch of smaller nanocrystals than the graph on the bottom (fig. b).

The absorption of the sample is taken repeatedly during growth, so that the growth may be halted when the absorption peak reaches the desired value in wavelength. For studies described in Chapter Five, this method allowed the author to grow batches of a variety of sizes (see Table 3-2 for a sample), while maintaining absorptions within the range of available lasers. Once the shell layer is added, there is no change in the location of the absorption peak (see Figure 3-9).

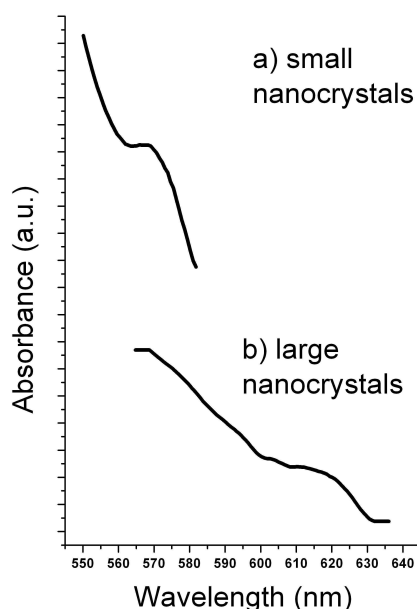


Figure 3-8: Absorption spectra for two batches of CdSe cores of diameters a) 3.9 nm and b) 5.0 nm. (The plot for (b) is an 11-point Savitzky-Golay average, which reduces low-level noise.) Notice that the absorption peak moves to the red as the size grows. The height of the absorption peak is directly related to the density of the material in the liquid-filled cuvette used while recording data.

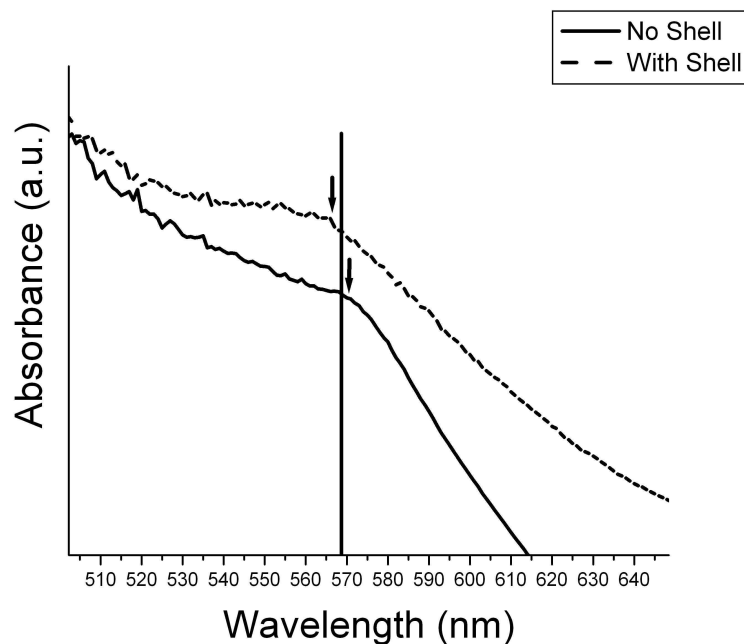


Figure 3-9: The absorption of the same batch of CdSe nanocrystal rods both without shell layer (solid line) and with shell layer (dotted line) of ZnS. The vertical line was added to guide the eye. Typically, it is difficult to discern any shift in absorption wavelength by sight alone for non-monodisperse batches. For very high monodispersity the core/shell dots are slightly red-shifted from their core-only precursors due to partial exciton leakage into the shell.⁵⁹ The arrows show the same relative feature (the knee of the absorption, where it begins to fall once again) for the capped (with shell) and uncapped (without shell) samples.

Photoluminescence

Photoluminescence (PL) is a linear spectroscopy technique that provides information on the quantum yield, size distribution, and exciton recombination energy of a nanocrystal batch (see Figure 3-10). PL intensity indicates the quantum yield (QY) and it follows that the brighter the PL, the higher the QY. The standard method for gaining a quantitative result is to characterize the PL intensity emitted from a sample of dye molecules at a particular concentration and excitation intensity. Starting from a dry

sample of nanocrystals, a solution of nanocrystals at the same concentration as the dye is made and excited. The QY is the PL intensity of the nanocrystals as a percentage of the dye intensity.

The peak location of the PL indicates the energy of band-edge recombination of an exciton, which is related to the size of the QD as relayed in Chapter Two. The full-width at half-maximum (FWHM) indicates, for an ensemble of QDs, the size-related inhomogeneous broadening of the sample. The reason that the broadening exists is that nanocrystals will not all grow to be exactly the same size. There is a distribution of sizes within an ensemble of nanocrystals that contributes to a distribution of exciton recombination energies, which gives rise to a broad PL signature. For a single nanocrystal, the PL will still possess some breadth above and beyond its unbroadened homogeneous linewidth, caused by inhomogeneous broadening of the energy transitions of the exciton, also referred to as spectral diffusion. Spectral diffusion is caused by local electric field fluctuations and will be revisited in future chapters. For CdSe dots capped with ZnS, the relationship of photoluminescence and size can be described as a linear fit in the parameter space of core diameter versus wavelength. In particular, in the case of CdSe cores overcoated with ZnS, the equation for the line is closely fit by⁵⁹

$$Diameter(\text{Angstroms}) = -88.6 + 0.228 * Wavelength(\text{nm}) \quad (3.1).$$

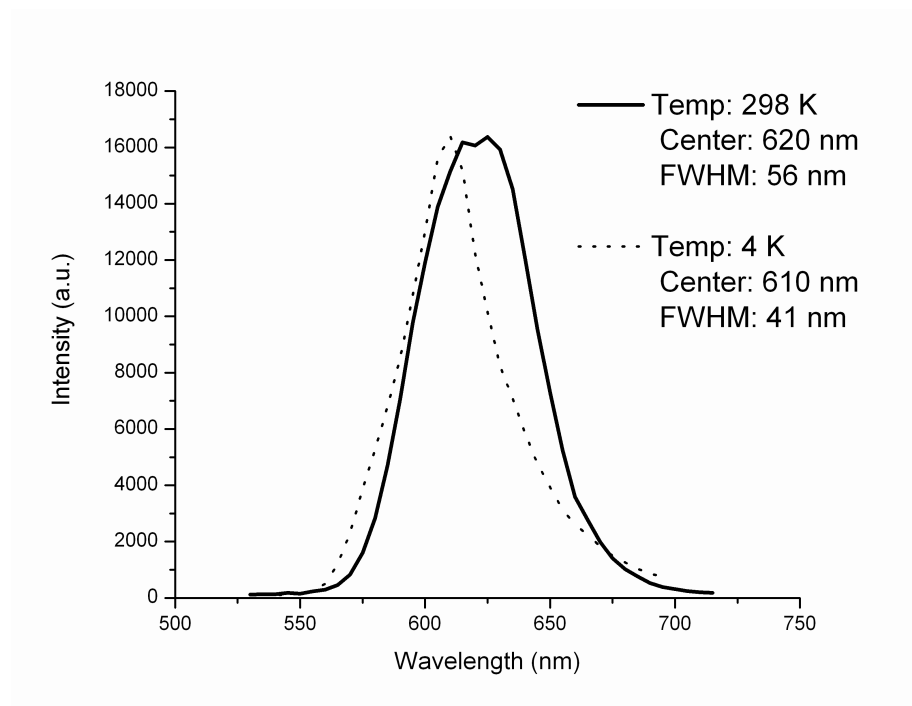


Figure 3-10: PL of the same batch of nanocrystals taken at room temperature and 4 K. Notice that the peak location has shifted.

PL taken at room temperature is shifted relative to that taken at low temperature. Low temperature reduces the number of phonons that may be present in the system. Figure 3-10 clearly illustrates the peak shift to the blue for low-temperature PL. This shift typically takes place near liquid nitrogen temperatures and above. The shift is related to the fact that when temperature decreases, the lattice contracts and the lattice constant is reduced. A change in lattice constant leads to a change in the band gap, where a smaller constant produces a wider band gap. A wider gap yields a higher energy PL peak. Nanorods display similar behavior to spherical nanocrystals (see Figure 3-11). Additionally, PL is the light emitted from the dark exciton state. At higher temperatures, the higher energy

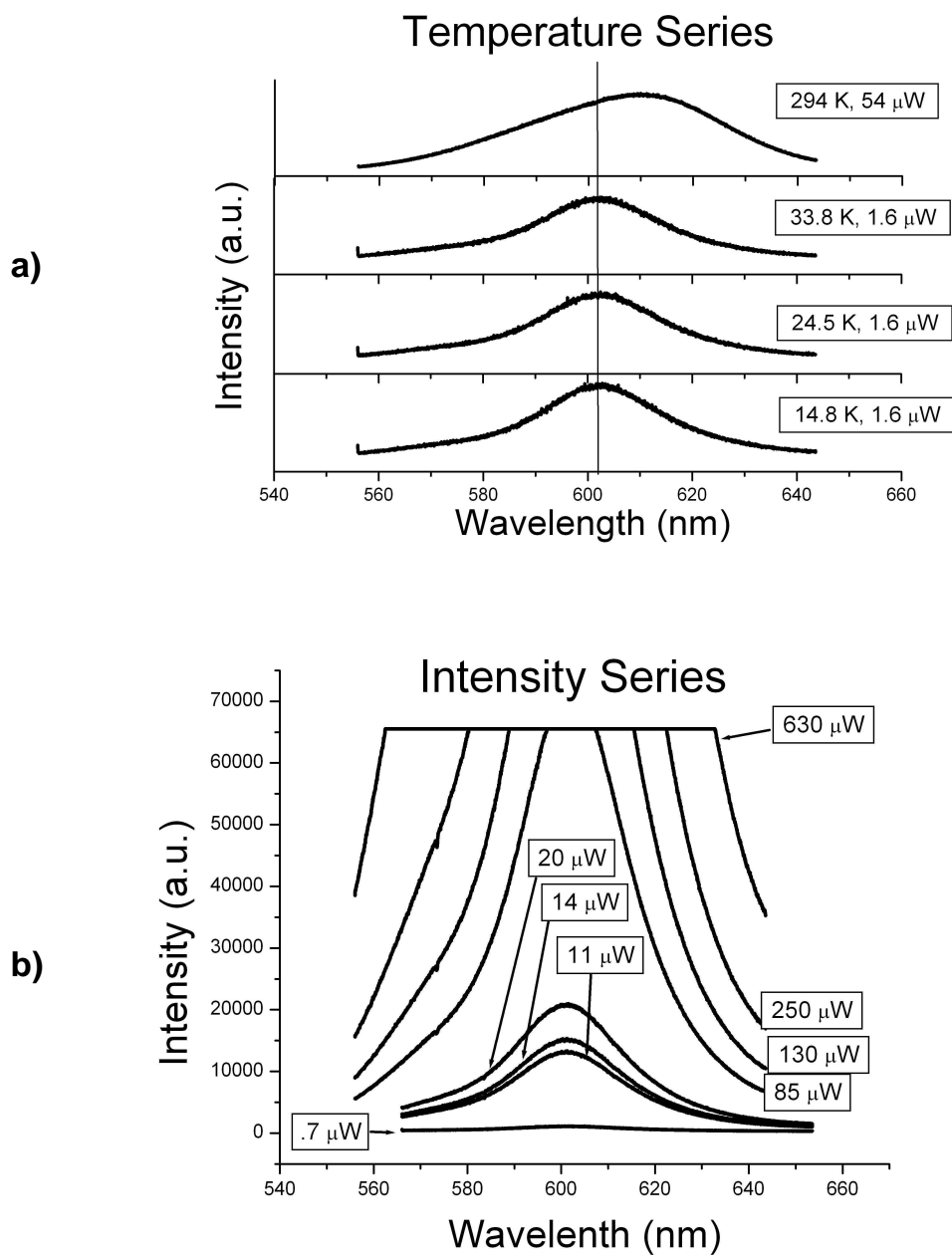


Figure 3-11: Nanorod PL at a) a variety of temperatures, and b) the same batch at a variety of excitation intensities. All spectra in (b) were taken at temperatures 11.5-13.3 K. For both series, exciting light was at 532 nm.

optically active $F_z = \pm 1$ state becomes populated. Light emitted from both the bright and dark states, therefore, cause a broad PL signature.³⁶

Two notable differences between rods and spheres, however, are exhibited in their temperature responses. First, the amount of the shift between room and low temperature is typically a little less for rods than for dots. Second, the FWHM does not change appreciably for rods at lower temperatures. Conversely, for spheres, the FWHM generally reduces at low temperature. Moreover, the FWHM values for rods are generally much less than that for spherical nanocrystals. Either the growth or size selection yields a more consistent batch, or excitons in the rods are much more consistently confined than the range of rod aspect ratios within one batch would suggest. In particular, if all rods from a batch are longer than the Bohr radius of the bulk exciton, the PL signature of 1-D recombining excitons should be very similar for every rod in the sample. Additionally, if some exciton localization takes place within the rods, the PL signature would not depend strongly on the specific length of the rod. Nanorod length beyond the Bohr radius does not effect the extent of the 1-D exciton appreciably, as also pointed out in Chapter Two.

TEM

Transmission Electron Microscopy (TEM) is a direct means of photographing the nanocrystals. The microscope works the same way as an optical transmission microscope, with the exceptions that the particles are accelerated electrons, the lenses are short solenoids, and “dark” on the image corresponds to electron density rather than optical opacity. Because a high resolution is needed, 120 keV (sometimes 100 keV) electrons are

typically used to image the nanocrystal samples. Samples are placed on a transparent carbon grid in a vacuum chamber and irradiated with a focused electron beam. The image is projected on a screen visible to the user. Once proper magnification, focus, and astigmatism control are achieved, the screen may be moved to accommodate a square of photographic film exposed to the electrons. The film is later developed, and the resultant image is scanned into a computer for data analysis and storage.

TEM is an excellent resource for checking on a sample's morphology, size distribution, absolute size, and even crystallinity. The phrase "absolute size" is used since there are no references in the literature to the electron beam-induced shrinking of CdSe or CdSe/ZnS nanocrystals. The resolution reached at the highest energy setting is sufficient to reveal the crystal planes of the nanocrystals.

Once each batch of nanocrystals has been characterized using the above methods of absorption, PL, and TEM, one can proceed to more insightful experiments such as spectral hole burning, which is described in the next chapter. Chapters Five and Six analyze the results of such experiments for two distinct morphologies of semiconductor nanocrystal—spheres and rods.

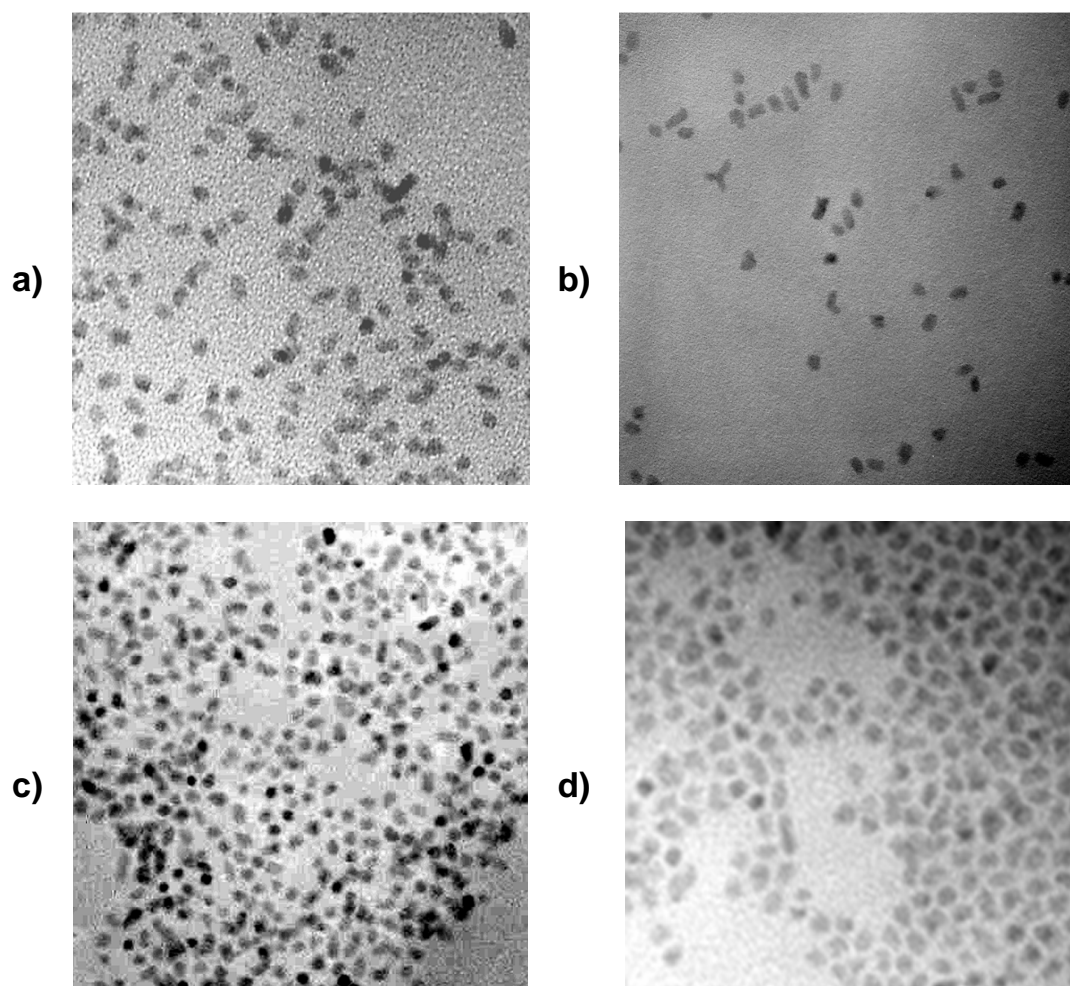


Figure 3-12: a) and b) show TEM images of nearly spherical QDs and prolate QDs, respectively. c) shows a large size distribution of nanocrystals, while d) presents a well size-selected batch with low size dispersity. Electron energies are 120 keV for all images.

CHAPTER 4

TRANSITIONS UNDER THE SPECTRAL HOLE BURNING TECHNIQUE

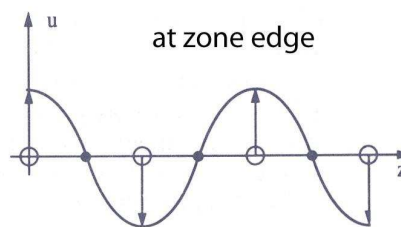
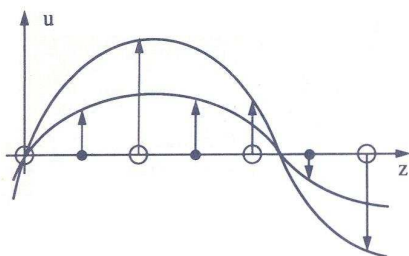
An incident light field excites excitons with a specific polarization. The loss of a well-defined phase relationship between this polarization with respect to the polarization of the light field is called *dephasing*. Excitons in nanocrystals experience two main sources of dephasing: spontaneous emission, which corresponds to a population relaxation back to the ground state, and pure dephasing, which does not change the population but does randomize the polarizations of the excited excitons. Dephasing of both types have many sources, but the one we will be chiefly concerned with is the interaction of excitons with the lattice. Exciton-phonon interaction dominates both population relaxation and pure dephasing processes. It is important to understand and quantify the effects that dephasing in general and electron-phonon interactions in particular have on exciton decoherence rates in order to determine whether quantum dots display the same nonlinear responses as atoms, and if not, how they differ. Measuring the effects of interactions in the quantum confinement regime help us explore the optical coherent properties of the samples. These properties are instrumental in determining the potential usefulness of exciton coherence in various applications.

In order to determine the effect that exciton-phonon interactions have on the samples, we need to perform experiments that reveal the transition linewidth of the first bright

exciton. The linewidth provides information about the dephasing rate in a way that we will discuss shortly. The first order of business in our quest for a cohesive physical picture of the meaning of the homogeneous linewidth is examining quantized lattice vibrations in QDs. We then visit the electronic structure of the QDs, and consider the QD (for the time being) as a two-level system coupled to phonons. We find that calculations partially replicate experimental results. Inhomogeneous broadening and the experimental method used to overcome it give us a picture of the optical conditions. We use this picture to discuss absorption in the sample.

Phonons

Acoustic branch



Optical branch

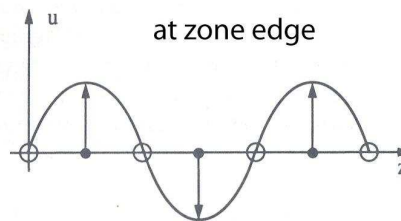
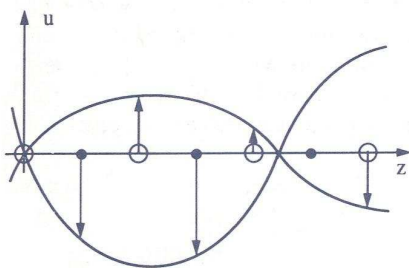


Figure 4-1: u is atom displacement. Figure from Klingshirn Figure 9.13a-d.³⁹ M , the mass of the larger atoms, is represented by the large open circles. M is greater than m , the lower-mass atoms, represented by the small solid circles.

Lattice properties of the QDs do not differ significantly from the bulk. This is because the size of the QD is much larger than the lattice constant. For the time being, let us discuss the lattice of a bulk system. The lattice in our case is diatomic. Independent normal modes of the lattice include two different mode types: acoustic and optical phonons. Acoustic modes correspond to in-phase motion of the two different types of atoms. That is, the entire unit cell moves cohesively. At the edge of the Brillouin zone only the more massive atoms oscillate. Optical modes, on the other hand, correspond to antiphase motion of the two types of atoms. The cation (Cd) and anion (Se) move with respect to each other within the unit cell. At the Brillouin zone edge only the less massive atoms oscillate. Figure 4-1 illustrates these two types of modes.

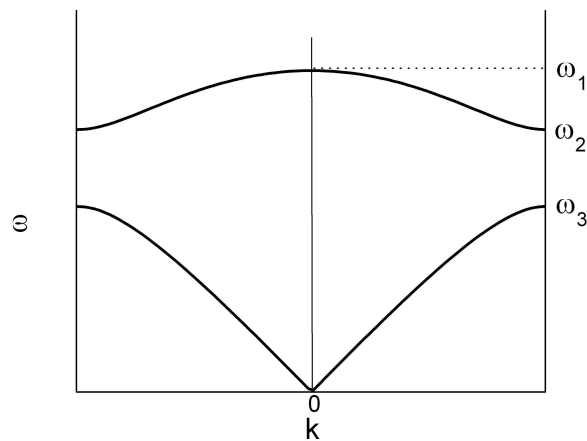


Figure 4-2: Dispersion curves for acoustic and optical phonons described by Equations 4.1 and 4.2, for an isotropic material. See Table 4.1 for values for ω_1 , ω_2 , and ω_3 . The top curve is for optical phonons and the bottom curve is for acoustic phonons in an isotropic lattice.

If the two atoms carry electric charge, that is, if the binding is at least partly ionic (true for CdSe), then the oscillation of the atoms is connected with an oscillating electric dipole. These transverse eigenmodes can be generated by photons via resonant absorption. This is why the oscillations are called “optical” modes. The ability to couple to the light field is why the optical branches do not vanish at $k=0$.

The dispersion laws for optical and acoustic phonons in an isotropic lattice are as follows:^{39,69}

$$\omega_{opt}^2 = \gamma \left(\frac{1}{m} + \frac{1}{M} \right) + \gamma \left[\left(\frac{1}{m} + \frac{1}{M} \right)^2 - \frac{4}{mM} \sin^2 ka \right]^{\frac{1}{2}} \quad (4.1)$$

$$\omega_{ac}^2 = \gamma \left(\frac{1}{m} + \frac{1}{M} \right) - \gamma \left[\left(\frac{1}{m} + \frac{1}{M} \right)^2 - \frac{4}{mM} \sin^2 ka \right]^{\frac{1}{2}} \quad (4.2)$$

The masses of the light and heavy atoms are m and M , respectively, while k is the wave

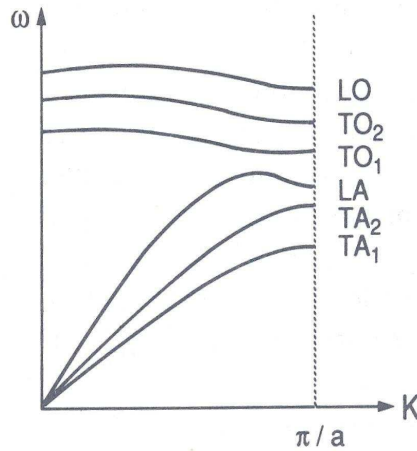


Figure 4-3: Acoustic and optical dispersion curves from the degeneracy has been lifted by an anisotropic lattice. Figure from Klingshirn Figure 9.15.³⁹ T stands for transverse, L for longitudinal, A for acoustic, and O for optical.

$\omega_1 = \sqrt{2\gamma\left(\frac{1}{m} + \frac{1}{M}\right)}$	Nonzero energy at $k=0$ becomes possible because in an optical mode different atoms are displaced antiphase.
$\omega_2 = \sqrt{2\gamma/m}$	Only light atoms oscillate at Br. zone edge.
$\omega_3 = \sqrt{2\gamma/M}$	Only heavy atoms oscillate at Br. zone edge.

Table 4-1: values for omegas noted in dispersion curve Figure 4-2.

number, a is the lattice constant, and γ is the effective force constant representing the harmonic character of oscillations in the balls-on-springs model we are using here.

Lattice anisotropy lifts the degeneracy inherent in the two branches. CdSe exhibits partly ionic binding, and is anisotropic. Therefore a more realistic picture of the dispersion is shown in Figure 4-3.

Electronic transitions

Considering only the lowest energy exciton, discussed in Chapter Two, our system nominally has a three-level Λ structure (see Figure 4-4). We can explain many of the nonlinear optical effects we observe with only a two-level system in conjunction with quantum-confined exciton-phonon interactions. As explained in Chapter Two, $|a\rangle$ is the true ground state of the system in which zero excitons exist, $|b\rangle$ is the first excited exciton bright state, and $|c\rangle$ is the exciton dark state, which is, as mentioned, optically passive since it is dipole forbidden from $|a\rangle$ (due to an angular momentum projection of ± 2).

The dipole-allowed transition $|a\rangle \leftrightarrow |b\rangle$ is coupled via the electric field ϵ_A . This electric field can be provided by a laser at the proper frequency. Once an exciton is excited into the bright state, $|b\rangle$, decay can take place back to $|a\rangle$ via nonradiative means or via coupling through the $|b\rangle$ state. In conventional spectroscopy, the limit of energy resolution between two levels $|a\rangle$ and $|b\rangle$ is governed by the sum of the decay rates out of these levels.⁷⁰ In our case, the decay rate from the ground state is zero. The decay rate for $|b\rangle$ will be discussed in detail later in the chapter.

Resonant excitation of an exciton causes an $|a\rangle \rightarrow |b\rangle$ transition. This is called the *bright exciton* transition. The exciton decays either back to $|a\rangle$ or to $|c\rangle$, where in a QD it exists for $\sim 1\mu s$. In bulk samples the lifetime is much shorter; about 1ns as discussed in Chapter Two. The long PL decay time in QDs is evidence that the dark state $|c\rangle$ exists. In the following we consider excitons to experience only a *two* level system, since the dark state does not actively participate in *absorption* processes. We consider only the resonant

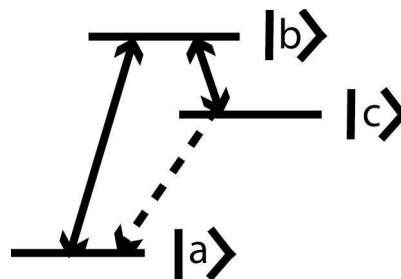


Figure 4-4: Level diagram for exciton states in CdSe QDs. $|c\rangle$ is the exciton ground state and a dark state. $|b\rangle$ is the lowest energy bright exciton state, and $|a\rangle$ is the system ground state, in which no excitons are present.

transition. We measure the absorption of the probe beam by the saturated sample. Other, higher energy, exciton levels are very far away from $|b\rangle$ due to the energy of quantum confinement. Therefore, a two-level description is appropriate in explaining most of the results of the saturation spectroscopy we perform. Some effects can only be explained when $|a\rangle$, $|b\rangle$, and $|c\rangle$ are all in play, and this case will be examined when it is needed. In the next section, we examine a general two-level system in the absence of a lattice.

QDs as two-level systems

We use a semiclassical approach in which the two-level system is treated quantum mechanically, while the field used to couple them is treated classically. It can be shown that a full quantum mechanical treatment of the field yields the same results as a semiclassical treatment.⁷⁰ The classical field induces electric dipole moments in the medium. In our case the dipole is between states $|a\rangle$ and $|b\rangle$, exciton versus no exciton.

A calculation by Goupalov, *et al.*,⁷¹ treats a two-level system coupled to phonons by only the deformation potential coupling and calculates the linear absorption cross-section. That is, the exciton is allowed to couple with only LA phonon modes. Chapter Five explains the different types of electron-phonon coupling in detail. The calculation yields a broad phonon spectral signature and a delta function-thin ZPL. The authors phenomenologically add a width, taken from experiments, to the ZPL. The calculation itself does not provide any broadening to the ZPL. We discuss linewidth and dephasing in detail later in this chapter. They find⁴⁶

$$\sigma(\omega) \propto \int_0^{\infty} dt (\text{Re}[U(t)] \cos(\omega - \omega_0)t - \text{Im}[U(t)] \sin(\omega - \omega_0)t). \quad (4.3)$$

The function $U(t)$ takes the form $U(t) = e^{K(t)}$. The transition energy of the two-level system is ω_0 . $K(t)$ contains two contributions. The first is the phenomenologic dephasing rate associated with the ZPL, and the second shows the deformation coupling effect on the width of the phonon sideband. Electron-phonon coupling enters via the Huang-Rhys factors (one per mode, each mode with a wave vector \vec{q}) $|A_q|^2 / \omega_q^2$.

$$K(t) = -\gamma_{\text{ZPL}} t + \frac{1}{V} \sum_q \frac{|A_q|^2}{\omega_q^2} \left((\cos \omega_q t - 1) \coth \frac{\hbar \omega_q}{2T} - i (\sin \omega_q t - \omega_q t) \right). \quad (4.4)$$

T stands for temperature, and V for the normalization volume. A graph from Reference 46 shows the linear absorption calculated above. This picture is not exactly the same as the data we find for QDs and nanorods (see Chapters Five and Six), but it at least

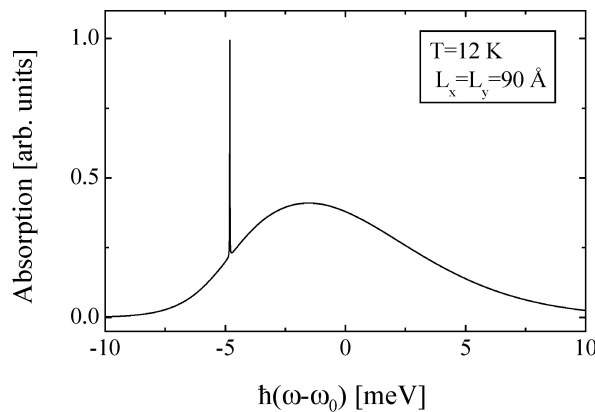


Figure 4-5: Calculated linear absorption spectrum for a single CdSe QD. The QD is self assembled and assumed square in shape. Although broadening of the ZPL is not included in the model, the relative contribution from the ZPL and the acoustic phonon assisted transitions to the zero *optical* phonon line (often called the acoustic phonon pedestal) is reproduced well.

gives confirmation that in the SHB signal the ZPL is a sharp resonance that rises from an acoustic phonon pedestal. The acoustic phonon pedestal is the result of exciton-phonon coupling. Real data also shows LO-phonon sidebands, which were explicitly neglected here.

Inhomogeneously broadened sample

There are several issues that must be addressed in order to make a SHB measurement that reveals the intrinsic homogeneous linewidth of a sample. These include, as we will see later, the effects of spectral diffusion and excitation intensity. First, however, we will examine the inhomogeneous broadening of the transition energy within the ensemble sample. A common difficulty with chemically synthesized nanocrystals is their size dispersion. Each crystal has a unique transition energy based on its size and local environment, and the transition itself can fluctuate.

Different methods exist to eliminate the effects of the nanocrystal size dispersion from the measured linewidth. One may take the spectroscopy of a single nanoparticle, or one may use a nonlinear optical technique such as spectral hole burning (SHB) or photon echo. Both single nanocrystal spectroscopy and photon echo have limited sensitivity and require large excitation intensity.⁷²⁻⁷⁵ Excitation intensity itself can cause broadening of the transition linewidth. Additionally, neither technique listed above is able to minimize the effects of spectral diffusion in the sample.

In order to achieve high sensitivity at low intensity, we use SHB. Unique modulation frequency dependence is added to the technique in order to correct for the effects of

spectral diffusion. This is achieved by changing the measurement timescale such that we take data faster than the diffusion rate of the nanocrystal band edge transition energy. Later we will see this is analogous to taking data at a lower photo excitation rate. By using a modulation frequency-dependent spectral hole burning technique to take differential transmission spectra of the samples, high resolution (nano-eV) at low excitation energy ($\sim 1 \text{ W/cm}^2$) is accomplished.

Under the proper conditions, which will be discussed later, differential transmission of a probe beam directly reveals excitonic transitions taking place in the sample. Size distribution broadening is circumvented by exciting only a particular subset of nanocrystals resonant with an excitation beam. The modulation frequency-dependence of our particular technique provides a mechanism for both probing and eliminating the effects of spectral diffusion in our measurement of the spectral hole linewidth of the samples.

Spectral Hole Burning and experimental setup

SHB is a nonlinear spectroscopic technique. Two excitation beams are used, called the pump and probe beams. The two continuous-wave beams are overlapped at the sample. The *pump* beam is typically more intense and stays locked at a particular frequency within the absorption profile of the sample. A weaker *probe* beam is scanned in frequency during the course of the experiment. The transmission of the probe is collected at a detector and plotted versus either frequency or detuning from the pump.

The pump causes transitions resonant with it to be saturated: that is, a significant fraction of the two-level systems are in the excited state, where they do not absorb the probe beam. In fact, the systems in the excited state increase the probe beam intensity via stimulated emission. Therefore, due to both reasons just listed, when the probe beam's frequency crosses the pump beam's spectral position, a transmission peak is observed in the transmitted probe intensity. This is an incoherent effect. Later, the specific conditions required to achieve an additional coherent contribution to the probe's absorption are discussed. In the absence of the pump, the probe's transmission is collected as a background signal. One way to describe the resultant differential transmission data is with the following equation where $\Delta\alpha$, the change of sample absorption caused by the pump, is small:

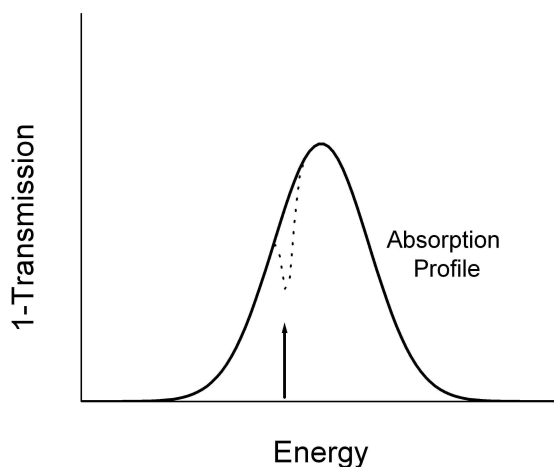


Figure 4-6: The arrow shows the location of the pump beam within the inhomogeneously broadened absorption profile of the sample. The dotted line shows the spectral window excited by the pump and outlines the absorption profile that the probe beam experiences.

$$\frac{\Delta T}{T} = \frac{e^{-(\alpha+\Delta\alpha)L} - e^{-\alpha L}}{e^{-\alpha L}} = e^{-\Delta\alpha L} - 1 \approx -\Delta\alpha L \quad (4.5)$$

Differential transmission of the sample is parameterized by laser detuning (in energy) between the two lasers. *Zero detuning* occurs when pump and probe frequencies overlap. As mentioned, a particular subset of nanocrystal sizes is resonantly excited. Very off-resonant crystals do not participate in the excitation, except at high pump intensity, in which case the absorption tails of off-resonant crystals begin to absorb energy in appreciable amounts and cause transitions in off-resonant crystals. This is one case of power broadening of the signal. Compared to PL and absorption, which are both linear spectroscopic techniques, SHB alleviates size distribution-related inhomogeneous broadening.

Figure 4-7 provides a small-scale schematic of the SHB experimental setup. As mentioned previously, both the pump and probe are continuous wave beams. The pump is modulated with an acousto-optic modulator (AOM) both for noise-reducing lock-in-detection purposes, and to vary the timescale at which the differential transmission measurements are made. This utility allows us to probe the effects of spectral diffusion. Spectral diffusion arises from small changes in the local electric field environment (including charge trapping in the nanocrystal) that alters the transition frequencies of the individual nanocrystals by random amounts. If a detection (which is to say, integration) timescale longer than the scale at which these fluctuations take place is used, the transition frequency we measure is smeared in energy. We say that the linewidth we measure is broadened (see Figure 4-8). If we increase our measurement rate by increasing

the modulation frequency of the pump, we minimize this broadening at the time scales we observe. Thus, we are able to measure a much narrower linewidth value simply by increasing the modulation frequency sufficiently. Varying the modulation frequency allows us to change the detection timescale, which allows us to both characterize and eliminate the effects of spectral diffusion.²⁰ Typical values of the frequency at which most spectral diffusion is eliminated are in the few hundreds of kilohertz; details are listed in Chapters Five and Six.

In order to access the resonances of a variety of sizes of nanocrystals (to test size-dependent trends), two mode-locked dye lasers were often used as the pump and probe. These were a Coherent-899 and -699, both ring cavity lasers, and each pumped with either a Coherent Verdi or a Spectra Physics Millennia Pro at 5.5 W and 532 nm. The dyes used were either Rhodamine 6G (for 565-610 nm) or Kiton Red (600-630 nm). For

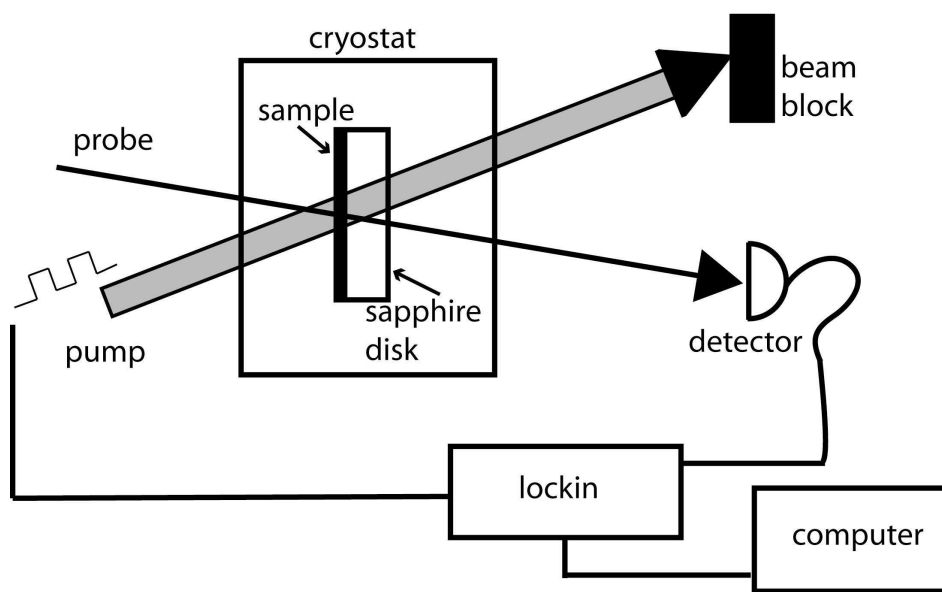


Figure 4-7: SHB schematic. Temperature is typically held between 4 and 12 K.

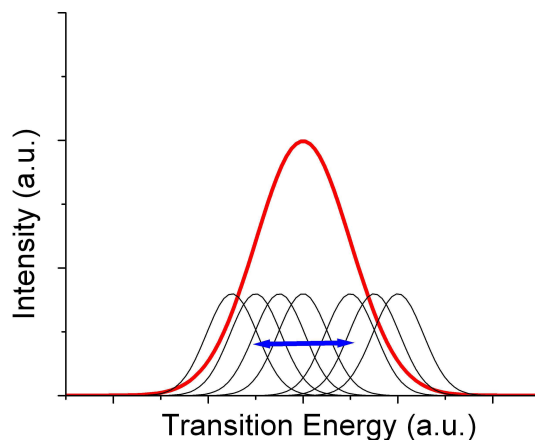


Figure 4-8: Spectral diffusion schematic. If measurements are made slowly compared to the transition energy diffusion rate, the linewidth we measure is wider than the actual decoherence-broadened linewidth homogeneous linewidth.

PbS nanocrystals the appropriate spectral range is in the far-red which allowed the use of a solid state diode laser (a Verdi New Focus laser with a range of 786-816 nm) in conjunction with a Coherent-899 ring Ti-Sapphire laser with a range of 780-820 nm, again pumped with a Coherent Verdi. The pump and probe linewidths were each narrower than $0.01 \mu\text{eV}$, or 2.5 MHz, in all cases.

The sample itself, whether quantum dots or nanorods, is dispersed in a polymer matrix, typically polystyrene, in order to produce a very low-scattering sample with a uniform nanocrystal concentration. The polymer-nanocrystal dispersion is drop-cast on a sapphire disk and allowed to dry into a smooth, thin film. Scattering must be kept low because the presence of scattering causes the signal to be quickly lost in a high background of pump noise.

The sample is held at low temperature (typically 4-12 K) in a cryostat in order to minimize electron-phonon interaction and thus reduce the total dephasing undergone by excitons, and to keep phonon modes discrete, as will be discussed later. This reduction in phonon impact allows us to resolve different transitions (both phonon-assisted and non-phonon-assisted) in the differential transmission spectrum.

We pump the sample on the low energy side of the absorption peak. This precaution aims to provide that we do not excite any more than the lowest energy bright exciton, the $1S_e 1S_{h,3/2}$ exciton. The intensities of the pump and probe beams are generally kept in the neighborhood of 1 W/cm^2 . Low excitation intensity helps ensure that the number of excitons created remains low, and that the excitons created are the lowest energy possible. This is important so that many-body effects such as biexcitons, trions, and other species are less prevalent. Ensuring that we probe only the lowest exciton state of each dot limits the inhomogeneous broadening inherent in the optical measurement. Additionally, low

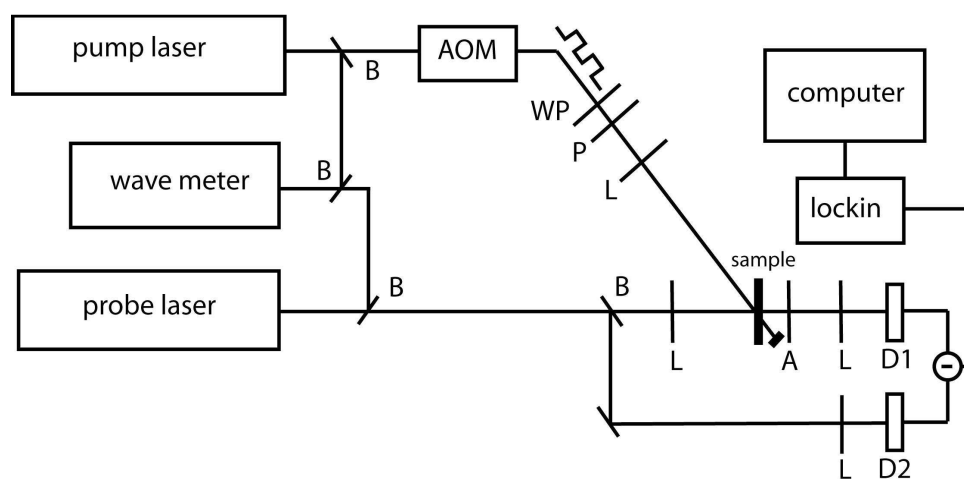


Figure 4-9: Overall SHB schematic. A stands for analyzer, B for beam splitter, D for detector, L for lens, P for polarizer, and WP for wave plate, in this case $\lambda/2$.

excitation intensity prevents substantial power broadening. The SHB linewidth increases monotonically with excitation intensity. Power broadening will be elaborated on later.

The pump couples to the zero-phonon line and the probe couples to different transitions in the manifold of phonon-assisted optical transitions, giving rise to sidebands and the broad acoustic phonon pedestal in the SHB response. The spectral range of acoustic phonons that can couple to the optical transition determines the linewidth of the acoustic phonon pedestal.

We now switch our attention to the exciton transitions themselves. The nonlinear optical effects inherent in a two-level system pumped at saturation are introduced, as are phonons and electron-phonon interactions. We eventually add a third level back into the system.

Dephasing

There are two important times associated with the optical processes discussed here. T_1 is the *lifetime* (or population decay time), which is to say, the decay time for the population difference for the number of systems in $|b\rangle$ minus the number of systems in $|a\rangle$. T_2 is the so-called *dipole* decay time, and is the time it takes a single exciton (dipole) to randomize its polarization from its initial state. It has been shown experimentally that for CdSe/ZnS QDs, the population lifetime is ~ 10 ns, while the dephasing time is ~ 1 ns.⁴⁶ *Dephasing* is a process by which coherences, or optical polarization, of a population of excited two-level systems is lost. There are two different types of dephasing, as indicated by T_1 and T_2 . The first is population relaxation, in which the population can decay either

radiatively or nonradiatively. This type of dephasing requires a real, state-changing transition to take place. We define

$$1/T_1 = \Gamma = \Gamma_{rad} + \Gamma_{nonrad}. \quad (4.6)$$

The population in the excited state decays in an exponential fashion: $\rho_{bb} \sim e^{-\Gamma t}$.

Nonradiative decay may involve phonon-assisted transitions.

The second source of dephasing is termed *pure* dephasing. In this process the phases of individual excited two-level systems are randomized from one another. The rate is named $\gamma = 1/T_2$. Pure dephasing processes do not change the excited state population but can involve *virtual* phonon-assisted transitions. We will see that electron-phonon interaction in quantum mechanically confined systems leads to both population and pure dephasing.

Throughout this dissertation the words dephasing and decoherence are used largely interchangeably. It is important to realize, however, that in the literature dephasing is usually reserved for lifetime or total dephasing, while decoherence refers to pure dephasing.

The phase relaxation rate of excitons in nanocrystals can be described in terms of a number independent processes characterized by these respective time constants. That is,

$$\Gamma_{total} = \frac{1}{2T_1} + \sum_i \frac{1}{T_{2i}}. \quad (4.7)$$

$1/\Gamma_{total}$ is the total dephasing time (also known as the transversal relaxation time). T_1 is still the population lifetime, and T_{2i} characterizes purely dephasing processes without

energy deviation, indexed by process type. As an example, electron-phonon interactions alone contribute three processes that cause pure dephasing.⁷⁶ These will be explained in Chapter Five. The total dephasing rate sets the linewidth measured using nonlinear optical techniques. For semiconductor nanocrystals it is reasonable to assume a frequency-independent dephasing rate at a given temperature. For a constant dephasing rate, Γ_{total} , a given excited state lineshape is Lorentzian.

Spontaneous emission alone yields $\Gamma_{total} = 1/2T_1$. This may be considered reasonable if the population of the excited state does not affect the dephasing rate. However, this is not the behavior exhibited by QDs. Along with spontaneous emission, exciton-phonon interactions are a strong source of exciton dephasing in semiconductors, as evidenced by the measured linewidths presented in Chapters Five and Six. These linewidths are much broader than expected for purely radiative decay.

For $T \rightarrow 0$, the ground state is expected to possess purely radiative decay lifetime broadening, which is the basic minimum linewidth limit. For finite and increasing temperature the optical transition experiences monotonic broadening due to the phonon-assisted scattering to and from the excited state. In other words, at extremely low temperature, dephasing is only made up of population decay. As the temperature increases, the pure dephasing rate becomes significant and increases much faster than the population decay rate.⁷⁷

The above shows that pure dephasing processes are dominant at finite temperature. Pure dephasing mechanisms include exciton-phonon interaction, carrier-carrier or

exciton-exciton interactions, scattering by defects, and spectral diffusion. We will also discuss an exciton localization and migration mechanism for rods in Chapter Six. We have already addressed spectral diffusion and will add more detail in Chapter Five. Carrier-carrier and exciton-exciton interactions are negligible at low excitation intensity, due to the very low carrier or exciton population density per dot. (The optimal values are zero or one exciton per dot.) Our nanocrystals are of excellent quality, as evidenced by the very high quantum yield they display, so we can safely assume defects are rare and that scattering by defects plays a negligible role in the dephasing rate of excitons. Therefore, the temperature dependence and shape of the measured linewidth are largely determined by exciton-phonon interactions. Dephasing by exciton-phonon interactions takes place because of stochastic fluctuations of exciton energy due to lattice vibrations. Exciton-phonon interactions and the manner in which they cause dephasing will be explored in detail in the next chapter.

Absorption

The ensemble of QDs contains many variations: size, shape, defects, and local environment. These variations lead to inhomogeneous broadening of both the absorption and emission spectra of the ensemble sample. Inhomogeneous broadening leads to certain properties and phenomena observable in atomic physics as well: spectral hole burning, fluorescence line narrowing under selective excitation, and a decay time distribution are all examples.⁶⁹ We concentrate on the behavior of inhomogeneously broadened two-level media. The optical transitions of *homogeneously* broadened systems are treated in a

number of text books.⁷⁸ We will briefly describe the absorption in a homogeneously broadened medium and then introduce the effects of inhomogeneous broadening. Detailed calculations of population and coherence expressions, their relationship to polarization, index of refraction, susceptibility, and the subsequent arrival at an expression for the absorption coefficient, α , are best left to the many excellent books that cover those topics.^{70,78,79}

Absorption in a homogeneously broadened media

The SHB technique described in this chapter is continuous wave. Therefore, steady state relations may be used to derive absorption relations. We note that QDs are *saturable absorbers*. This means that absorption is intensity dependent. The presence of the pump beam leads to a change in the absorption coefficient of the sample. The intensity-dependent absorption (where intensity, I , is expressed in units of W / cm^2) is written

$$\alpha(\omega_0, I) = \frac{\alpha_0(\omega_0)}{1 + I / I_{sat}}, \quad (4.8)$$

where the saturation intensity $I_{sat} = \hbar\omega_0 N(\alpha_0 T_1)^{-1}$. N is the total number of two-level systems. The energy difference between levels $|a\rangle$ and $|b\rangle$ is $\hbar\omega_0$. α_0 is the absorption coefficient for the case when the incident intensity is zero; it is the maximal value of the absorption. An alternate expression is $I_{sat} \approx \hbar\omega / \sigma T_1$, where $\hbar\omega$ is the photon energy and σ is the absorption cross section. For CdSe QDs, T_1 has been estimated to be ~ 10 ns.⁴⁶

The absorption spectral line shape of a homogeneously broadened sample is determined by dephasing dynamics. If the dephasing time is constant, the shape of the absorption is Lorentzian:

$$A(\omega) = A_0 \frac{\Gamma^2}{(\omega - \omega_0)^2 + \Gamma^2}. \quad (4.9)$$

Γ is the half-width of the homogeneous absorption. The absorption has intensity-dependent amplitude and width. The intensity dependent absorption is denoted

$$\alpha(\omega, I) = \frac{\alpha_0(\omega_0)}{1 + I/I_{sat}} \frac{\Gamma_0^2 (1 + I/I_{sat})}{(\omega - \omega_0)^2 + \Gamma_0^2 (1 + I/I_{sat})}. \quad (4.10)$$

$\Gamma(I) = \Gamma_0 (1 + I/I_{sat})^{1/2}$ is the half-width, and Γ_0 is the *homogeneous linewidth*. This linewidth is due exclusively to homogeneous lifetime broadening.

Absorption in an inhomogeneously broadened system in the presence of two excitation beams

The introduction of inhomogeneous broadening is subsequently seen to cause the appearance of the *spectral hole* we measure in our experiments. The width of this hole, 2γ , is dephasing-dependent. Recall that $\gamma = 1/T_2$ is the dipole dephasing rate of the two-level system, which does not include lifetime broadening. Dephasing in an inhomogeneously broadened system, γ_{inh} , is greater than in a homogeneously broadened system, γ . We now examine the inhomogeneously broadened ensemble of two-level systems. In a sample such as ours, the presence of a pump beam leads to the selective absorption saturation of systems resonant with the pump (see Figure 4-1). That is, only a

subset of nanocrystals is resonantly pumped. As the intensity of the pump increases, the depth and width of the spectral hole increases. This type of power broadening results from the increasing contribution of systems whose absorption tails overlap the excitation frequency. An additional effect is that of intensity-induced spectral diffusion, which also acts to broaden the spectral hole.

If we include a probe beam as well as a pump, the very tunability of the probe (along with its weaker intensity) provides that it does not change the excited state population. The two beams cause an interference pattern when they are both present at the sample. This pattern contributes to the total electric field. The interaction of the two beams in the sample causes the probe absorption coefficient to be more complex than just the probe Lorentzian multiplied by a population difference saturated by the pump. The interference pattern causes *population pulsations* which contribute to the probe's absorption coefficient and contribute a coherent piece to the probe absorption, as we will show shortly.

Population pulsations occur at the beat frequency between pump and probe:

$$\Delta_{beat} = \nu_{pump} - \nu_{probe}. \quad (4.11)$$

They arise from the populations of the upper and lower levels responding to the superposition of pump and probe modes nonlinearly. Since the probe does not saturate the sample, the pulsations occur only at the beat frequency $\pm\Delta_{beat}$. The pulsations act to put sidebands in the medium's response to the pump mode. One sideband falls on the probe beam's frequency. This contribution corresponds to the coherent scattering of the

pump into the probe beam. As intimated, this generates the coherent part of the probe's absorption coefficient. A property of the probe's absorption coefficient is that the area under the curve is independent of the coherent contribution. That is, the population pulsations redistribute the absorption as a function of $\pm\Delta_{beat}$, but do not modify the medium's broadband absorption.⁷⁸

In SHB, the probe is used only to read out the population created by the pump beam, as described earlier. The pump creates the absorption profile that the probe encounters. This profile is written as the sum of an incoherent contribution to the absorption plus the coherent contribution:

$$\alpha_{probe} = \alpha(\omega, I) = \alpha_{incoherent} + \alpha_{coherent} . \quad (4.12)$$

In the case of strong inhomogeneous broadening, a saturating pump beam, and a non-saturating probe beam, the probe's transmission reveals a broad spectral hole (due to the incoherent part of the absorption) with a sharp coherent dip at zero detuning between pump and probe. It is necessary that $T_1 \gg T_2$ (that is, $\Gamma \ll \gamma$) in order for the sharp dip to be present. The coherent dip forms because when the level lifetimes are long compared with the dipole lifetimes ($T_1 \gg T_2$), the population inversion is unable to follow a pump-probe beat frequency much larger than its decay rate. The coherent contribution to the probe absorption coefficient falls off as the beat frequency is increased (that is, detuning increases from zero.)

Figure 4-6 illustrates the probe differential transmission profile in the presence of strong inhomogeneous broadening, a saturating pump, and $T_1 \gg T_2$. The shape of the

incoherent part of the spectral hole burned into the inhomogeneously broadened absorption spectrum is:

$$\alpha_{incoherent}(\omega, I) = \alpha_0(\omega) \left(1 - \left(1 - \frac{1}{(1 + I/I_{sat})^{1/2}} \right) \frac{\Gamma^2(I)}{(\omega - \omega_0)^2 + \Gamma^2(I)} \right) \quad (4.13)$$

where $\alpha_0(\omega)$ is the initial absorption spectrum of the sample without incident radiation and $\Gamma(I) = \Gamma_0 \left(1 + (1 + I/I_{sat})^{1/2} \right)$ now describes the half-width of the burned hole within the inhomogeneous absorption profile. As can be seen in the expression above, the hole is Lorentzian in shape with an intensity-dependent width. In the limit of small intensity, as is the case in our experiments, $I/I_{sat} \ll 1$,

$$\Gamma(I) \rightarrow 2\Gamma_0. \quad (4.14)$$

Recall that $\Gamma(I) = 2\Gamma_0$ is the *half*-width. This leads to the relationship between the measured spectral hole width and dephasing rate that we use to analyze the data obtained via SHB. That is,

$$\text{hole width (FWHM)} = 4\Gamma_{total} = 4(\Gamma + \gamma), \quad (4.15)$$

which is to say, the spectral hole width is four times the exciton dephasing rate. In our system, $\gamma \gg \Gamma$, so we usually consider the hole width to equal 4γ . In this context we usually call γ the decoherence rate.

More general expressions exist as well. The total complex absorption takes into account the differences in frequency between a given two-level system resonance and both the pump and the probe. If we consider our pump to be on resonance with the set of nanocrystals it excites,

and the detuning (δ) of the probe from the resonance (and the pump, in this case) to be just the beat frequency discussed earlier, we can write down a complex absorption expression:

$$\alpha = \frac{\alpha_0 \gamma^2}{(\gamma^2 + I)(\gamma - \delta)} \left(\frac{2 - I \left(\frac{\Gamma}{\Gamma + i\delta} \right)}{2 + I \left(\frac{\Gamma}{\Gamma + i\delta} \right) \left(\frac{\gamma}{\gamma - i\delta} \right)} \right). \quad (4.16)$$

Our particular case of inhomogeneously broadened QDs obeys this rule. The observable absorption is just the real part of the above expression. It includes both the coherent and incoherent spectral holes. We also take $\gamma \gg \Gamma$, as mentioned above. The spectral hole width arises from the fact that the convolution of two Lorentzians (the probe beam profile and the power-broadened spectral hole shape) is itself a Lorentzian with a width equal to the sum of the individual widths.⁷⁸ This says the probe absorption displays a spectral hole twice as wide as that burned into the population difference, under the proper intensity condition. At ω_0 (at resonance with the two-level transition),

$$\alpha(\omega_0, I) = \frac{\alpha_0(\omega_0)}{(1 + I/I_{sat})^{1/2}}, \quad (4.17)$$

which differs from the homogeneous case by a factor of $(1 + I/I_{sat})^{1/2}$.

These calculations do not take factors such as spectral diffusion or exciton-phonon interactions into account. These two phenomena cause our hole width equal to 4γ relationship to break down. Spectral diffusion is known to broaden the spectral hole even more. Experimental demonstrations of this effect are found in subsequent chapters. The particular modulation frequency-dependent SHB technique used for our experiments addresses this

problem by increasing the rate at which measurements are taken until it is more rapid than the timescale at which transition energy diffusion takes place. To account for intensity-induced spectral diffusion, we also take data at very low excitation intensity.

As will be discussed in Chapter Five, we cannot probe spectral diffusion above a particular frequency. There may be high spectral diffusion effects in our data that we are unable to quantify. However, we are able to reach an asymptotic value of the ZPL linewidth well before the end of our frequency range.

The width we actually measure is significantly larger than $4\Gamma_0$, even after we have reduced spectral diffusion to a minimum at the timescales we operate in. The difference is attributable to lattice-induced dephasing effects; in particular, interactions of the two-level system with phonons.

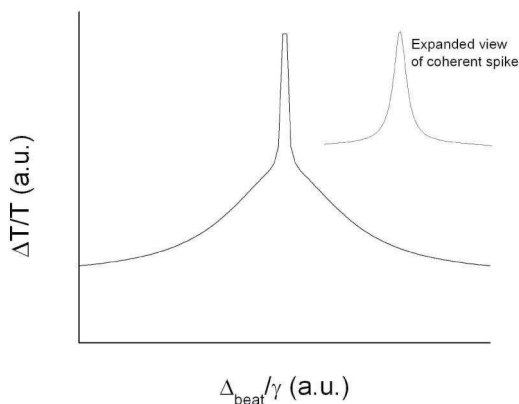


Figure 4-10: Transmission, rather than absorption. Broad incoherent spectral hole with a sharp coherent *absorption* dip at zero detuning. γ is taken to be much greater than Γ ($\gamma = 20\Gamma$ for plotting purposes). Recall that for absorption, this picture would be upside-down, with the “base” at $\alpha = 1$, provided the graph is normalized by α_0 .

Exciton-phonon interactions are a very important aspect of the studies presented in this dissertation. The interactions, the effect of confinement on the spectra of phonons, and the relationships of temperature, excitation intensity, QD size, and modulation frequency on the measured linewidth are all discussed in the following chapter. Chapter Five presents data for CdSe/ZnS QDs and offers interpretations of the data based on electron-phonon interactions.

CHAPTER 5

EXPERIMENTAL RESULTS FOR QUANTUM DOTS

As explained in previous chapters, it is of significant interest to elucidate the details of optical transitions in low-dimension semiconductor nanostructures. It is especially important to understand dephasing and its effects on the measured linewidth. The dephasing rate exceeding the expected radiative decoherence rate of ~ 0.0165 GHz (corresponding to a radiative lifetime of 10 ns) is a direct measure of the level of exciton dephasing caused by electron-phonon interactions. Here, we present data that illuminates the way parameters such as spectral diffusion, excitation intensity, and temperature affect the measured zero phonon linewidth. We explain that exciton-phonon interactions are the likely cause of many of the effects we observe. CdSe/ZnS core/shell QDs provide the bulk of the data; however, for completeness these results are compared with measurements made on PbS QDs and self-assembled CdSe/ZnSe QDs, both provided by collaborators. Certain properties of these samples cause the SHB spectra they produce to be different in predictable ways from that of our QDs.

We first investigate the confinement of phonons in QDs and the resultant phonon sidebands in the SHB spectra. Following this, exciton-phonon interactions are classified and examined. We then analyze data which delineates the effects of a variety of

parameters on the width of the ZPL. Finally, we compare CdSe/ZnS QDs to PbS dots, and explain the differences in the spectra obtained for each. Chapter Six follows, and contains the data for CdSe/ZnS nanorods.

Discrete phonons

Acoustic phonons in nanocrystals become discrete because of the finite size of the lattice. In our samples, the QDs are considered “free-standing,” with so-called free boundary conditions due to the elastic properties of the surrounding polymer matrix. Discrete acoustic phonons are standing waves, reflecting at the boundaries of the QD. The coupling of discrete phonons to excitons leads to phonon sidebands in both absorption and spectral hole burning spectra. These sidebands are a series of peaks corresponding to discrete phonon-assisted transition energies with the same energy spacing as the discrete phonon modes themselves.

Acoustic properties of an elastically isotropic spherical nanocrystal can be described in terms of two kinds of eigenmodes, namely torsional and spheroidal modes.⁸⁰ Spheroidal modes are radial “breathing modes” while torsional modes are twisting modes of the QD. The lattice distortion, $\vec{u}(\vec{r})$, is described by the Navier equation which characterizes the propagation of lattice vibrations in an elastic medium. In nanocrystals, vibrational modes are mixtures of longitudinal and transverse components, which give rise to the spheroidal and torsional modes mentioned above. Namely,

$$\vec{u}(\vec{r}) = -\left(\frac{v_{long}}{\omega}\right)^2 \vec{\nabla} \Lambda + \left(\frac{v_{trans}}{\omega}\right)^2 \vec{\nabla} \times \vec{\Gamma}, \quad (5.1)$$

where Λ is a scalar field describing the longitudinal mode, $\vec{\Gamma}$ is a vector field describing the transverse mode, and $v_{long/trans}$ is the sound velocity (also called elastic constant) associated with the longitudinal/transverse component. Additionally,

$$\left[\nabla^2 + \left(\frac{\omega}{v_{trans}} \right)^2 \right] \vec{\Gamma} = \vec{0} \quad (5.2)$$

and

$$\left[\nabla^2 + \left(\frac{\omega}{v_{long}} \right)^2 \right] \Lambda = 0 \quad (5.3)$$

must be satisfied. These expressions (Equations 5.2 and 5.3) are Helmholtz equations.

The eigenvalue solutions yield *discrete* energies indexed by l , m and n , the angular momentum, angular projection, and radial mode number, respectively. In a spherical QD the total angular momentum must be conserved.⁶⁹ The solutions are degenerate in m , which is now omitted from the description of the phonon modes.

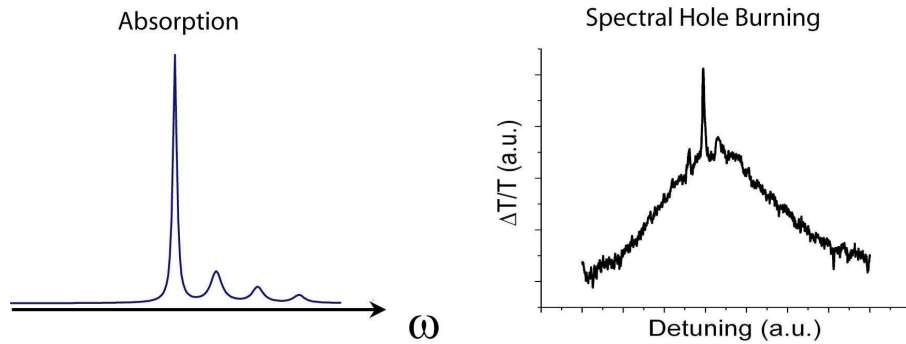


Figure 5-1: Absorption and spectral hole burning spectra with phonon sidebands. The absorption signal is calculated while the SHB signal is actual data from CdSe/ZnS QDs. In the SHB data, the tall, sharp peak is the ZPL, the two small flanking peaks are discrete acoustic phonon sidebands, and the large background peak consists of a large number of semi-continuous acoustic phonon sidebands.

We ask if the size of the QD changes either the width of the ZPL or the energies at which the discrete acoustic phonon sidebands occur. We address the question of ZPL linewidth first. Figure 5-2 compares four different QD sizes with average diameters 4, 5.3, 6.2, and 8.9 nm, respectively. Recall that the dephasing rate listed on the y-axis is one fourth the SHB linewidth, as discussed in Chapter Four. It is evident that the size of the spherical QD has little to no bearing on the dephasing rate measured at high modulation frequency.

The energy distance of the first order acoustic phonon from the ZPL does show size dependence, however. The solutions of the equations above are inversely proportional to the dot diameter. The energies found in the solution are the phonon mode energies, indexed by mode, and hence are the same as the sideband energies in our spectra.

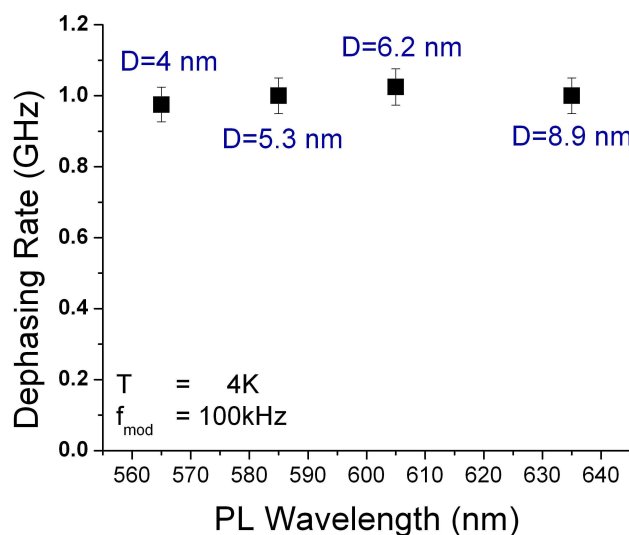


Figure 5-2: QD size dependence of lowest dephasing rate measured for each sample. $T=4\text{ K}$, modulation frequency= 100 kHz .

Discrete energies broaden and eventually become continuous as either dot diameter or temperature increases. The main assumption of the sideband energy calculation is that the nanocrystal is perfectly spherical with no defects. The calculation for various l, n values are the solid lines in Figure 5-3. A plot of experimentally measured sideband energies for the four QD sizes mentioned above is found to compare well to the calculated size dependence of the $l=2, n=1$ acoustic phonon mode. ($l=0$ is a totally symmetric breathing mode, while $l=2$ corresponds to a so-called ellipsoidal mode: breathing occurs first along one direction, and then orthogonal to it.) The difference between the calculated mode and the data at large QD diameter is attributed to the model being applicable to a totally spherical QD. A real QD becomes more prolate and faceted as it grows larger, providing a reasonable explanation of the small deviation at large sizes between the data and the calculated phonon energy.

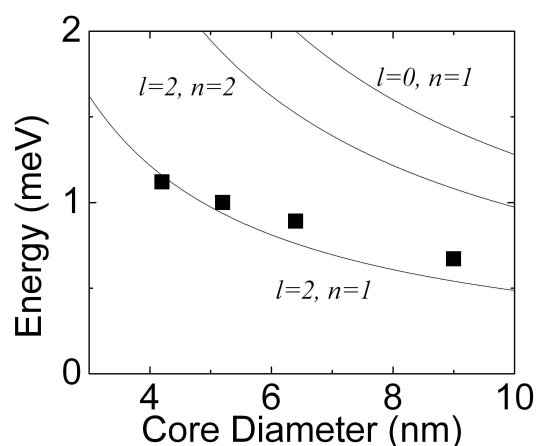


Figure 5-3: The calculated size dependence of the first acoustic phonon sideband, compared with the energy measured for four sizes of real QDs. Data taken at 10 K and 100 kHz modulation frequency. Intensities I_{pump} and I_{probe} are unknown to the author.

Exciton-phonon interaction

The exciton-phonon interaction is of considerable importance in semiconductor optics. The interaction dominates the pure dephasing and population relaxation processes in nanocrystals. Therefore, electron-phonon interactions determine the nonlinear absorption linewidth and the luminescence Stokes shift in our samples. In our differential transmission data, phonon sidebands associated with LO and acoustic phonons are clearly represented. Figure 5-5 shows these sidebands. We explain in this section how they arise.

Coupled electron-phonon (or exciton-phonon) states are eigenstates of the system. Figure 5-4 shows a schematic representation of electron-phonon coupling. Phonon emission is proportional to $(N_{ph} + 1)$ and the absorption of phonons is proportional to N_{ph} , where N_{ph} is the phonon occupation number of the respective mode.

The electron-phonon interaction mechanisms fall into two categories. The first is *deformation potential (DP)* coupling and the second is polar coupling. Polar coupling is generated by two distinct mechanisms, *piezoelectric (PE)* and the Fröhlich interaction.

DP coupling arises from the lattice distortions caused by acoustic phonons traveling through the crystal.^{39,48,81} LA phonon modes cause stretching and contraction of the distance between atoms. As mentioned previously, when the distance between atoms changes, the local potential and band gap change. A LA phonon can be considered a periodic deformation of the band gap. Both the electron and hole are influenced by the resulting modulation of the band structure. The energy associated with DP coupling is proportional to the strain tensor:

$$H_{DP} = D_{e/h} \vec{\nabla} \cdot \vec{u}_{ac}(\vec{r}) \quad (5.4)$$

where $D_{e/h}$ is the electron/hole DP coupling constant, and $\vec{u}_{ac}(\vec{r})$ is the displacement field caused by *acoustic* phonons (see Equation 5.1).

Polar coupling depends on interactions involving electric fields. The two polar coupling mechanisms, PE and Fröhlich, derive from acoustic and optical phonons, respectively. Only polar crystals can support polar interactions.

PE coupling is the result of an electric field polarization caused by strain in the crystal. Again, phonons produce a periodic modulation of the lattice parameters, which produces a varying electric field due to the ionicity of the atoms that make up the crystal itself. The electric field of the electron interacts with the electric field produced by the acoustic phonon.³⁹ The Fröhlich interaction arises between the polarization associated with LO phonons and the electric field of the electron. Exciton coupling to LO phonons mediated by the Fröhlich interaction is usually described in terms of the Huang-Rhys factor, S , which determines the linewidth and the luminescence Stokes shift,

$$2\Gamma_0 = 2S^{1/2} \hbar \omega_{LO}, \quad \Delta_{Stokes} = 2S \hbar \omega_{LO}. \quad (5.5)$$

These polar interaction mechanisms are strongly distance-sensitive. The energy associated with both the PE and Fröhlich interactions is

$$H_{polar} \sim \int d^3 r \vec{\nabla}_r \left(\frac{1}{|\vec{r} - \vec{r}_e|} \right) \vec{P}(\vec{r}). \quad (5.6)$$

$\vec{P}(\vec{r})$ is the polarization associated with acoustic phonons (both LA and TA) in the case of PE coupling, and LO phonons in the case of the Fröhlich interaction.

The general Hamiltonian for a coupled electron-phonon system interacting via a linear interaction (harmonic oscillator phonon modes) can be written in the following way:⁷⁶

$$H = \sum_{\lambda} E_{\lambda} c_{\lambda}^{\dagger} c_{\lambda} + \sum_{\vec{k}} \hbar \omega(\vec{k}) \times \left[a_{\vec{k}}^{\dagger} a_{\vec{k}} + \frac{1}{2} \right] + \sum_{\vec{k}} V_{\vec{k}} \left[a_{\vec{k}} \rho(-\vec{k}) + a_{\vec{k}}^{\dagger} \rho(\vec{k}) \right] \quad (5.7)$$

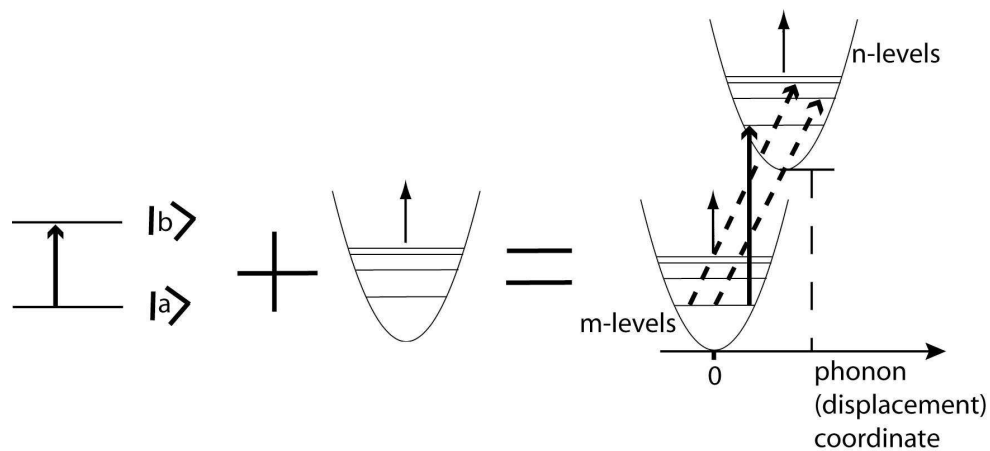


Figure 5-4: Electronic states coupled to discrete phonon states leads to a series of discrete transitions. Discrete transitions appear as peaks in both the absorption and SHB spectra. The ZPL is the $m=0$ to $n=0$ transition, and is represented by the vertical solid arrow. The vertical long-dashed line represents the energy of the lowest energy exciton. The number of phonons involved in an excitation is determined by the m and n values of a given transition. The short-dashed arrows show examples of non-ZPL transitions that could take place. Several assumptions are made: 1) The Franck-Condon principle holds. That is, the electronic transition is very fast compared with the motion of the lattice. 2) Each lattice vibrational mode is well described by a quantum harmonic oscillator. This has been calculated to be correct to a great deal of precision, but only at low temperature, by Gusev *et al.*⁸² 3) Only the lowest phonon mode(s) are excited. For sufficiently low temperatures, this may be assumed correct. Our experiments reveal a manifold of phonons in the acoustic phonon pedestal, so the assumption is minorly inappropriate. Only a finite and small number of phonons are excited, however, so the model presented above is acceptable for understanding a single transition. 4) The interaction between the exciton and the lattice is the same in both the ground state and the excited state. The assumption is represented above by two equal harmonic oscillator potentials. The assumption is met due to the low Franck-Condon factors associated with CdSe.

where

$$\rho(\vec{k}) = \sum_{\lambda, \lambda'} c_{\lambda'}^\dagger c_{\lambda} M_{\lambda', \lambda}(\vec{k}) \quad (5.8)$$

$$M_{\lambda', \lambda}(\vec{k}) = \int d^3x e^{-i\vec{k} \cdot \vec{x}} \bar{\phi}_{\lambda'}(\vec{x}) \phi_{\lambda}(\vec{x}). \quad (5.9)$$

The electron eigenfunctions are $\phi_{\lambda}(\vec{x})$ with associated eigenvalues E_{λ} and creation operators c_{λ}^\dagger . \vec{k} is the phonon quasimomentum, while a_k^\dagger is the phonon creation operator. The electron-phonon interaction is denoted by V_k . Simplifications and assumptions can be made that reduce the complexity of this Hamiltonian. See, for example, Reference 76.

Confinement of exciton-phonon interactions

The relative strengths of the two types of coupling (DP and polar) are size-dependent.⁷⁷ In the case of DP coupling, the size dependence of the dephasing rate scales as R^{-2} , where R is the quantum dot radius. In the case of PE coupling the size dependence obeys R^{-1} behavior. Electron interaction with the deformation potential provides an explanation of the temperature-dependent homogeneous linewidth. The Huang-Rhys factor that describes the Fröhlich interaction systematically increases with decreasing nanocrystal size. This will be discussed in detail later.

Experimentally, the sidebands are observed when one beam (the pump) couples to the ZPL while the other beam (the probe) couples to the phonon-assisted transition. The

sidebands rest on a large acoustic phonon pedestal (see Figure 5-5). The broad pedestal is caused by semi-continuous leaky acoustic phonons from all other available acoustic phonon modes in the nanocrystal.

Optical modes are modified by confinement in a different way. Along with the optical modes present in the bulk, surface modes appear that depend on the dielectric function of both the nanocrystal and the surrounding medium. In particular, the most prominent mode corresponds to a uniform polarization over a spherical particle and is called the Fröhlich mode. Fröhlich modes cause LO phonon sidebands. These sidebands have high energy compared to the acoustic phonons and do not couple to the ZPL. Therefore, they do not offer us much insight into the transition dephasing that we are interested in.

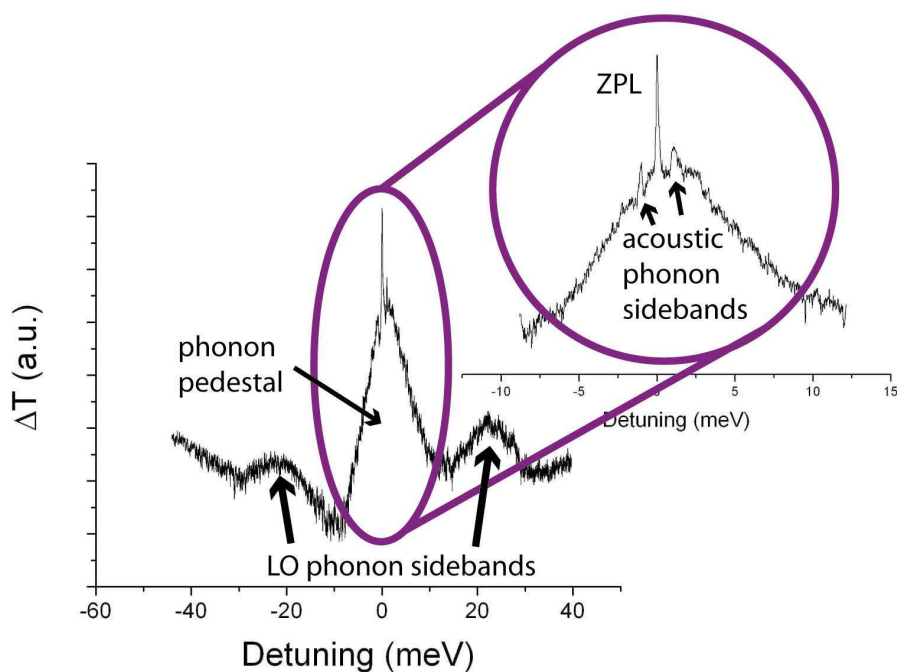


Figure 5-5: Experimental differential transmission spectrum for quantum dots as a function of detuning. Note the relative energies of LO and acoustic phonon sidebands relative to the ZPL. This data was taken at 4.2 K.

The zero-phonon line (ZPL) width is the spectral hole width discussed previously. The width of the spectral hole demonstrates the intrinsic upper limit for decoherence. We measure the incoherent part of the spectral hole, as was described in Chapter Four.

Phonon-assisted transitions

Typical phonon energies are much lower than the energy between excited exciton levels in a QD. Exciton relaxation from one state to another is possible via the emission of optical and acoustical phonons. (Absorption of phonons for excitation to a higher state is also possible.) In nanocrystals, the relaxation process via phonons is expected to be less efficient than in the bulk due to the discrete excitonic levels in QDs and the fact that optical phonon energies are constrained to specific material-dependent values. If an optical phonon is to be involved, the condition

$$\Delta E = nE_{LO} \quad n = 1, 2, 3, \dots \quad (5.10)$$

must be met, where ΔE is the energy difference between the two levels and E_{LO} is 26 meV in CdSe. This effect, in which LO phonon-assisted transitions are constrained, is called the *phonon bottleneck*. Due to the bottleneck effect, electron-phonon interactions contribute primarily to pure dephasing through the virtual absorption and emission of phonons that do not change the exciton population.⁸³ Therefore, the effect of the phonon bottleneck is not particularly strong, as evidenced by the efficient band edge PL we observe.

Acoustic-phonon assisted transitions are constrained not only by the discrete electronic levels of the exciton, as in the LO phonon case, but also by the discrete nature

of their own spectrum (see Figure 5-4). Nevertheless, in small nanocrystals multiple emissions of acoustic phonons appear to be the main relaxation mechanism between excited states. In the bulk, emission of LO phonons is the dominant mechanism.

At low temperature, low energy acoustic modes should dominate, as per their Bose-Einstein distribution. The modes cannot exceed the size of the crystal, or acoustic phonon-assisted transitions are inhibited as well. As temperature is raised, the acoustic phonons regain a continuous energy spectrum which increases the efficiency of phonon-related relaxation. At these higher temperatures exciton scattering by acoustic phonons destroys coherence.

The net effect of the electron-phonon interaction is that decoherence rates for excitons in semiconductor nanostructures are increased from the radiative lifetime limit. The phonon spectrum is restricted due to the system size, which reduces the efficiency of the electron-phonon interaction, but raising the temperature can destroy the discreteness of the phonon modes. Finally, experimentally observing the SHB linewidth provides a direct way to measure the dipole dephasing rate of excitons in the sample.

Spectral diffusion

It has long been known that spectral diffusion takes place in semiconductor QDs, as well as in optically active molecules of many sorts. Recently, spectral diffusion in quantum dots has engendered new interest.⁸⁴⁻⁸⁷ In particular, reducing spectral diffusion in these structures is seen as a necessary step for integration into a variety of applications.

Spectral diffusion is, in our context, the fluctuation of the transition energy of the two-energy-level nanocrystals. Spectral diffusion is closely linked with a phenomena called *blinking* in which a single nanocrystal, continuously pumped and observed over time,¹⁰⁶ exhibits dark and bright periods. During the bright period the nanocrystal continuously absorbs and emits without interruption. Dark periods indicate nonradiative decay, and often last much longer than 100 ms. It is observed that the transition energy of a single nanocrystal typically shifts during a dark period so that when a bright period resumes we say that spectral diffusion has taken place. It is thought that the mechanisms that cause blinking also cause spectral diffusion. These mechanisms are either the charging of the nanocrystal, or the trapping of one of the charges of the exciton. Each of these processes, as nonradiative decay takes place, causes a slight reformation of the energy landscape of the crystal, which leads to a modified transition energy.

We find that as we take measurements on shorter and shorter timescales we observe a narrowing of the measured linewidth. Measuring at shorter timescales is equivalent to integrating over fewer excitation events. We now present the data, and then explain the observed trend of decreasing ZPL intensity as a function of modulation frequency. We will find that it is necessary to stop ignoring $|c\rangle$, the dark state, as part of the excitonic electronic structure in order to explain the data.

Observations

As the timescale of the measurements we make is altered, we find a very strong relationship between measurement timescale and the measured linewidth (see Figures 5-6 and 5-7). We express the y-axis of much of our data in terms of dephasing or decoherence rate, rather than SHB linewidth, in order to relate our results to a more meaningful physical quantity. The overall amplitude of the ZPL decreases (see Figure 5-6) as the modulation frequency is increased. This causes the signal-to-noise ratio to be reduced. The low S/N makes it difficult to measure ZPL widths at high modulation frequencies. This places a practical limit of approximately two MHz on the frequency range of spectral diffusion that we can study.

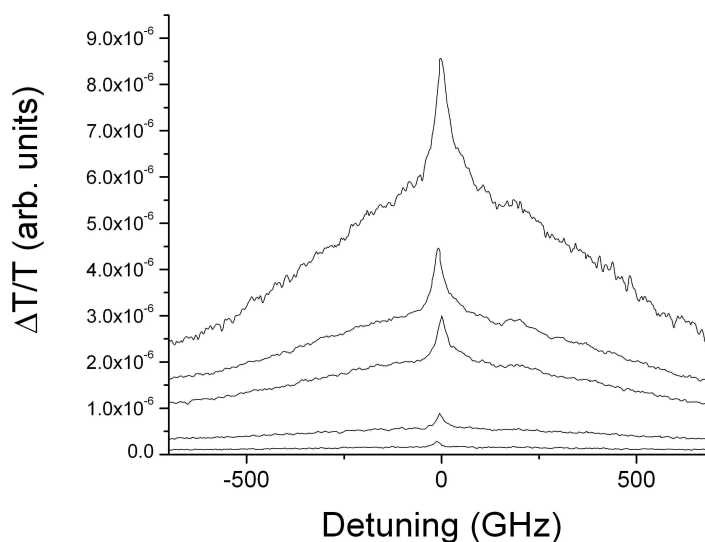


Figure 5-6: ZPL of the same sample for pump modulation frequencies of, in order of decreasing peak intensity: 1, 10, 20, 50, and 100 kHz. See Figure 5-7 for conditions.

The fact that the ZPL magnitude decreases as the modulation frequency increases is indicative of a slow decay of the SHB response. If there were no delay over time, the ZPL magnitude (though not the width) would be unaffected by the integration time of the measurement. Systems trapped in state $|c\rangle$ cannot respond at the rate of the pump modulation frequency. Therefore, states emitting from $|c\rangle$ do not emit at the frequency we lock-in to, and we do not measure those emissions. (An analogy is an electronic low-pass filter.)

In Chapter Four we discussed saturation spectroscopy. The higher the excitation intensity used, the broader the spectral hole. However, in order to avoid power broadening (see the next section) we use very low excitation intensity. We are not causing much *saturation* hole broadening. Instead, the incident radiation causes spectral

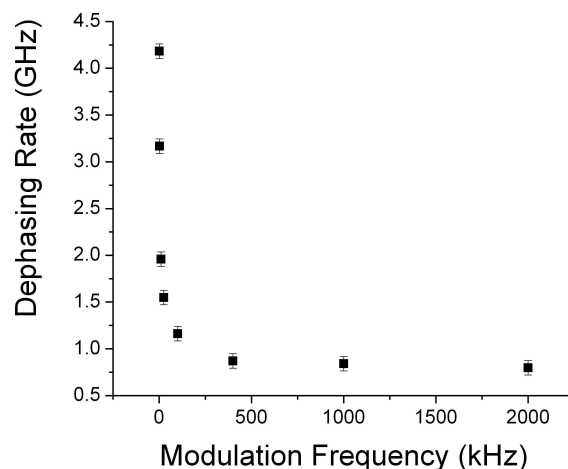


Figure 5-7: Exciton dephasing rate in QDs versus pump modulation frequency; the modulation frequency sets the measurement timescale. The data shown was taken by Phedon Palinginis on a quantum dot sample synthesized by Xudong Fan. Dot diameter=9 nm, $T=1.8$ K, $I_{\text{pump}}=1.0$ W/cm², and $I_{\text{probe}}=0.5$ W/cm².

diffusion which itself leads to broadening. Based on the timescales at which the ZPL falls to an asymptotic value (see Figure 5-7), we gather that the effects of intensity-induced spectral diffusion for $I_{\text{pump}} = 1 \text{ W/cm}^2$ and $I_{\text{probe}} = 0.5 \text{ W/cm}^2$ are most pronounced at timescales greater than $\sim 2 \mu\text{s}$.

The ZPL linewidth depends on the number of excitation events taking place within the measurement time. We find that decreasing the measurement time or reducing the excitation intensity both reduce the linewidth. Charge trapping, as in a long-lived dark state, accounts for the long decay time of the SHB response.

Four-wave mixing (FWM) experiments^{20,46} verify that the mechanism underlying the SHB response does feature a very long lifetime. The relaxation time of the coherent contribution to the nonlinear response is more than two orders of magnitude greater than the expected radiative lifetime. Let us reexamine the electronic transition landscape (see Figure 4-4).

Absorption only promotes electrons to $|b\rangle$, since $|a\rangle \rightarrow |b\rangle$ is the only dipole-allowed transition from $|a\rangle$. Excitons may decay either to $|c\rangle$ or back to $|a\rangle$. Evidence for excitons quickly decaying to $|a\rangle$ is in the time-resolved PL measurable in the samples.⁴⁶ Evidence for slow decay from $|c\rangle$ is in the FWM measurements mentioned earlier.

The nonlinear saturation spectroscopy that yields the spectral hole depends on a large fraction of the available systems being excited. Saturation is determined by the population difference between $|b\rangle$ and $|a\rangle$. The key aspect of this process is that the systems are not in the ground state and hence are not able to absorb the probe beam.

Decay of systems in $|b\rangle$ to $|c\rangle$, rather than back to $|a\rangle$, maintains depopulation of the ground state relative to the bright state. Saturation of $|b\rangle$, therefore, is determined in large part by the lifetime of excitons trapped in $|c\rangle$.

Saturation causes a nonlinear signal based on *both* the population of $|b\rangle$, and the depletion of $|a\rangle$ due to the long-lived population in $|c\rangle$. The lifetime we measure in the nonlinear response in SHB depends on the time it takes excitons trapped in $|c\rangle$ to return to either $|b\rangle$ or $|a\rangle$, and the time it takes some of the excitons in $|b\rangle$ to return to $|a\rangle$ directly. Direct recombination time is just the radiative lifetime, and is three orders of magnitude faster than the decay time from $|c\rangle$.

$|c\rangle$ can vary from nanocrystal to nanocrystal, based on the size of the QD or nanorod. Within a single nanocrystal it is possible for defect states near the excitonic level $|c\rangle$ to provide a manifold of dark states. The ZPL homogeneous linewidth is characterized by $2\Gamma_c$, for $T_c \gg T_b$ ($\Gamma_c \ll \Gamma_b$). (Here, $\gamma \sim \Gamma_c$.) For a manifold of dark states the Lorentzian shape of the spectral hole is modified to a non-Lorentzian shape.

Due to the very long lifetime associated with state $|c\rangle$, we conclude that the spectral hole burning signal we observe is, in fact, persistent hole burning as opposed to transient hole burning. Dark state trapping occurring at a rate faster than the radiative recombination rate provides a robust explanation for the long times associated with exciton decay. ZPL linewidth depends strongly on the decay time from the dark state.

The relative change in dephasing rate for QDs over the modulation frequency range that we can access is approximately 75%; we will see that this is a greater value than for nanorods. By a modulation frequency of about 1 MHz, the effects of spectral diffusion have been reduced to a minimum at the timescales we measure. In order to minimize the effects of spectral diffusion on the data, at least at the timescales we use, it is recommended that the pump beam be modulated at approximately 0.6-1 MHz. It is possible that further reduction of the dephasing rate is achievable by modulating at still higher frequencies. We have been unable to test this possibility due to the signal to noise issue discussed earlier.

Spectral diffusion is an effect seen in QD structures but not in the bulk semiconductor material; nor is it observed in quantum wells or quantum wires. Quantum dots are susceptible to the effects of spectral diffusion due to the size of the structures.⁶⁹ Each dot responds individually to its local electric field environment, induced especially by nonradiative decay processes, while in all higher-dimensional structures the transition energy results from the energy levels of the whole-structure, which do not respond efficiently to very localized perturbations. This may be reversed if charge localizations take place in these higher-dimensional structures.

Intensity dependence

Excitation intensity dependence of the ZPL linewidth is demonstrated in Figures 5-8 and 5-9. Higher intensity leads to a broader ZPL, and increases the ZPL magnitude as well. Intensity dependence comes from two sources: first, saturation, and second, power-induced spectral diffusion.

Saturation power broadening has been mentioned in Chapter Four. Recall Equation 4.13, and the fact that the absorption profile depends on the intensity of excitation. Physically, a particular size of quantum dot is resonantly excited by the saturating pump beam. The absorption tails of nonresonant QDs also overlap the spectral position of the

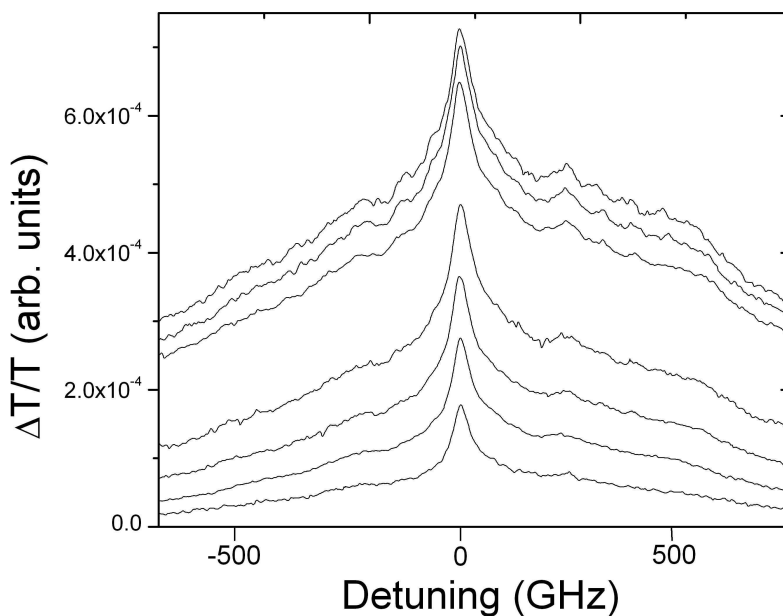


Figure 5-8: Power broadened ZPL spectra for, in order of increasing peak intensity, a pump power of 100, 200, 400, 800, 1600, 3600, and 5200 μW . Notice that both the magnitude and width of the spectra increase with increasing power. $T = 5.5 \text{ K}$.

pump. As the pump intensity is increased, these nonresonant absorption tails increase their response (until they, too, reach saturation). Thus, we expect the SHB linewidth, and therefore the dephasing rate, to increase monotonically with pump beam intensity. The data matches the expectation and is shown in Figure 5-9.

The second source of intensity dependence is light-induced spectral diffusion. This spectral diffusion is due to a higher intensity of incident light exciting more charges in the nanocrystal, leading to blinking events and the attendant spectral diffusion. For example, in single CdSe QDs,⁷³ it has been observed that both the rate and extent of spectral diffusion is highly intensity-dependent. Table 5-1 shows the intensity and diffusion amount cited in Reference 73. For sufficient integration time, the diffusion appears as a power broadening. Many of the effects of this spectral diffusion have been discussed in the previous section. This form of spectral diffusion is more important in our data since we work at much lower intensity than that associated with saturation.

In order to reduce the effects of intensity-related broadening in our data, we work at low intensities. Typical experimental values are 0.5-3.0 W/cm², for both pump and probe beams. The probe intensity is kept lower than the pump intensity for most experiments.

Intensity (W/cm ²)	Spectral diffusion amplitude (meV)
2500	60
65	2
25	< 2

Table 5-1: Data taken by Empedocles, *et al.*⁷³ for intensity dependence of the spectral diffusion of a single CdSe nanocrystal. Integration time was one minute.

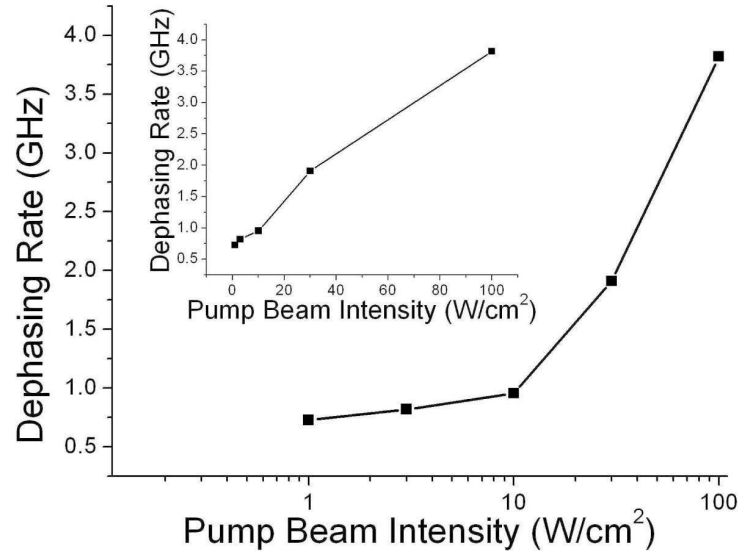


Figure 5-9: QD power broadening as a function of pump beam intensity. Data taken by Phedon Palinginis. Modulation frequency is 100 kHz. Note the use of logarithmic scale. The inset shows the same data on a linear scale.

Temperature dependence

Temperature plays a crucial role in dictating not only the number of phonons present in the QD system, but also whether acoustic phonons have a discrete or continuous spectrum. Exciton-phonon interactions are explicitly temperature dependent, and the temperature dependence of the ZPL itself indicates coupling strength. Therefore, temperature is a particularly important parameter for the measured dephasing rate. However, a broadened ZPL is not a feature of the simplest electron-phonon model, referred to as the Huang-Rhys or independent boson model. In the Huang-Rhys model the interaction strength is denoted with a parameter called S .

$$S(\lambda) = \frac{fq^2}{\pi\hbar\omega_l^3} \int \frac{d^3k |M_{\lambda,\lambda}(k)|^2}{k^2} \quad (5.11)$$

$M_{\lambda,\lambda}(\vec{k})$ was defined in Equation 5.9. The frequency spectrum of phonons is independent of k , where k is the phonon quasimomentum. That is,

$$\omega(\vec{k}) = \omega_l = \left(\frac{\epsilon_0}{\epsilon_\infty} \right)^{1/2} \omega_0, \quad (5.12)$$

where $\epsilon_{0/\infty}$ is the static/high-frequency dielectric constant and ω_0 is the reststrahl frequency (the limiting value of the frequency of a TO mode dispersion curve as $\vec{k} \rightarrow 0$).

Considering the case of the ZPL, \vec{k} must be zero. $S(0)$ is easily calculated using the above expression, and by using the definition of $M_{\lambda,\lambda}(\vec{k})$ mentioned earlier. $S(0) = 0$, indicating that in this simple model there is no electron-phonon coupling strength at the position of the zero-phonon line. We observe broadening of the ZPL, however, strongly suggesting non-zero coupling strength, so the simple model is not sufficient to explain the data.

In their paper on calculating a new microscopic approach to understanding optical transitions in QDs, Muljarov, *et al.*⁸³ use a modified independent boson model to find that the ZPL broadens due to emission and absorption of virtual phonons. These virtual transitions are between state $|b\rangle$ and higher lying exciton energy levels. The energy of the exciton does not change, making this a pure dephasing process. They assert that virtual transitions are the major mechanism of phonon-induced dephasing in single QDs. This is reasonable as long as exciton level distances are much larger than the typical energy range of the acoustic phonons coupled to the QDs. The broadening is exclusively due to off-diagonal elements of the exciton-phonon interaction Hamiltonian.

The ratio of zero-phonon transitions to non-zero-phonon transitions should decrease with increasing temperature. That is, the optical absorption becomes more and more dependent on phonon-assisted transitions as the number of phonons increases, and the spectrum of phonons expands from discrete to continuous with temperature. This can be seen by comparing the relative heights of the LO-phonon sidebands to that of the ZPL in Figure 5-10, and the acoustic phonon sidebands to the ZPL in Figure 5-11. Above liquid helium temperatures there is enough thermal energy to excite many phonons and the probability of a zero-phonon transition occurring is close to zero.

Finally, we present the dependence of the ZPL on the temperature (see Figure 5-12). The expectation is that the dephasing rate rises monotonically with temperature. The temperature dependence is clearly nonlinear. This is in opposition to the temperature-dependent behavior of the ZPL in bulk material and in QWs. At low temperatures it is expected to rise linearly, in keeping with the bulk material and QWs.

One way to explain, and fit, the nonlinear dependence on temperature is to appeal to a two-phonon Raman process where absorption and emission of a discrete phonon simultaneously occur. The temperature dependence of the homogeneous broadening is given by⁸⁸

$$\Gamma_{one\ phonon}(T) \propto \sinh^{-2}(\hbar\omega/2k_B T). \quad (5.13)$$

$\hbar\omega$ is the energy of the lowest confined phonon mode. To account for the two phonon modes involved, we can predict the experimentally observed dephasing, γ , with the sum of contributions from two phonon modes, plus the radiative dephasing:⁸⁹

$$2\gamma(T) = A \sinh^{-2}(E_a/2k_B T) + B \sinh^{-2}(E_b/2k_B T) + 2\Gamma_{rad} \quad (5.14)$$

where $\Gamma_{rad} = 16\mu\text{eV}$, $E_a = 0.67\text{meV}$, $E_b = 1.5\text{meV}$, $A = 3\mu\text{eV}$, and $B = 4.7\mu\text{eV}$. The curve in Figure 5-12 shows the fit based on this expression. It corresponds well with observationally obtained data. However, it is important to remember that this is just a numerical fit and does not necessarily imply that the model underlying the above expression is correct.

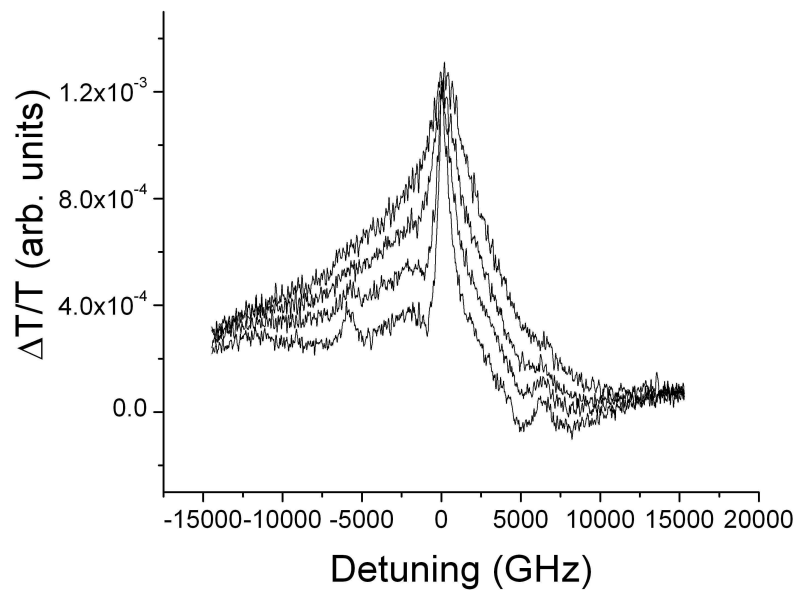


Figure 5-10: The phonon pedestal expands and the LO phonon sidebands broaden as the temperature rises. Similarly, acoustic phonon sidebands disappear with rising temperature although they are not visible on this scale. These spectra, from lowest to highest pedestal intensity, are taken at $T = 10, 20, 40,$ and 60 K respectively. The modulation frequency is 2 kHz and the pump is at 635 nm .

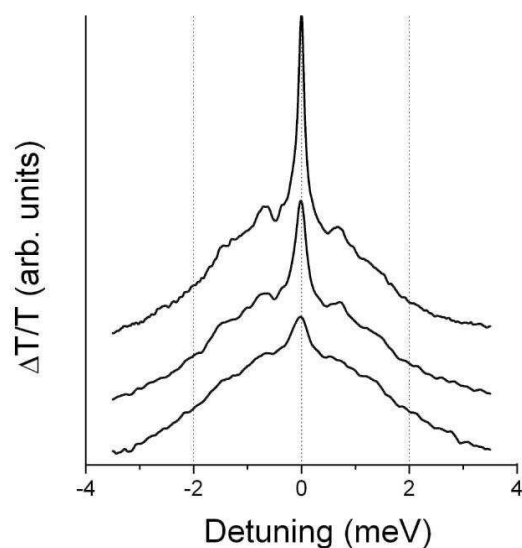


Figure 5-11: The ZPL width expands as the temperature increases. In order of increasing peak height, these spectra were taken at 23, 12, and 4 K respectively. The spectral weight of the ZPL shrinks relative to the acoustic phonon sidebands as temperature rises.

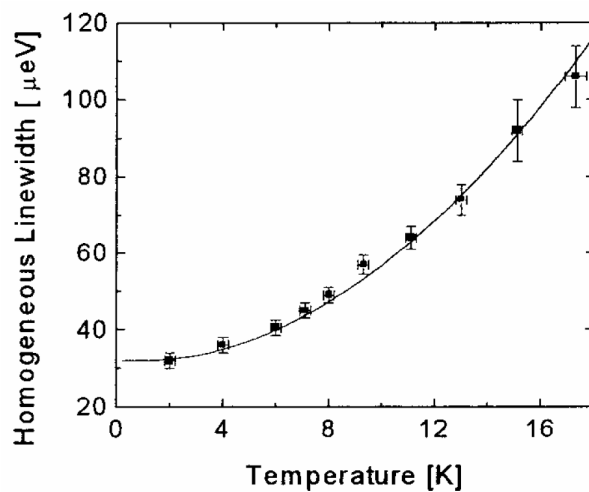


Figure 5-12: Temperature dependence of the dephasing rate of colloidal quantum dots. The line is a fit to the data using Equation 5.14. Data taken by Phedon Palinginis. Nanocrystal average diameter is 9 nm and the modulation frequency is 100 kHz. Graph from Reference 89.

Self-assembled versus chemically precipitated quantum dots

For comparison's sake, it is instructive to examine the temperature and spectral diffusion dependences of the dephasing rate in self-assembled CdSe QDs. Self-assembled CdSe/ZnSe QDs with a PL peak at 565 nm, produced via molecular beam epitaxy, were supplied to our group by collaborators. Figures 5-13 and 5-14 display the temperature dependence and spectral diffusion dependence, respectively, of self-assembled QDs. The temperature dependence shows a slightly different shape than for chemically precipitated dots; it is also clearly nonlinear, similar to chemically precipitated dots. Physical differences include the shape, size, and size dispersity of the two types of dots. The dots in the self-assembled sample are only 2.5-3 monolayers thick, and disk-shaped. They are grown on a 2 μm thick ZnSe layer, which itself is grown on a GaAs substrate,

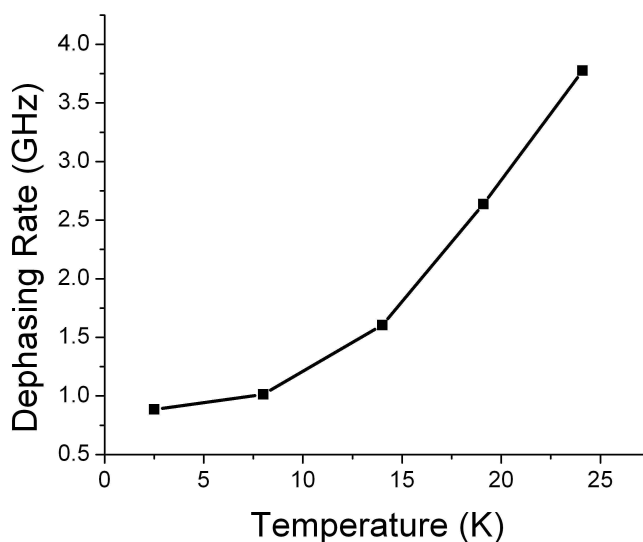


Figure 5-13: Temperature dependence of the dephasing rate of self-assembled CdSe/ZnSe QDs. Data taken by Phedon Palinginis. The modulation frequency is 3 MHz.

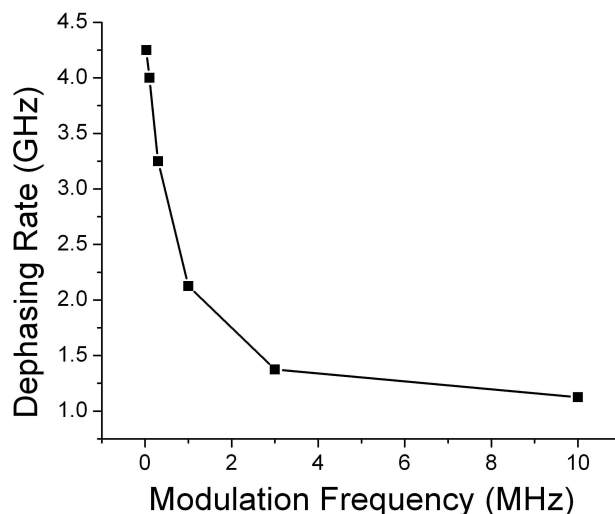


Figure 5-14: Spectral diffusion effects in self-assembled CdSe/ZnSe QDs. T=10 K. and capped with a 50 nm layer of ZnSe after they have formed. One expects lower surface strain on the dots due to better lattice matching between CdSe and ZnSe (7%) than between CdSe and ZnS (12%). The dot densities are on the order of $10\text{-}100/\mu\text{m}^2$.

Spectral diffusion susceptibility in self assembled dots is seen (Figure 5-14) to be similar to that in precipitated dots. The self-assembled dots are more uniform than chemically precipitated dots, so it is possible to find and measure the width of the ZPL even at high modulation frequencies. The rate decreases as the modulation frequency is increased, as before. However, the final decoherence rate measured is about $3.5 \mu\text{eV}$ (0.85 GHz), which is nearly the same as the lowest rate found for nearly spherical QDs.⁹⁰ The rate is also comparable to that found in InGaAs QDs.⁹¹

Material matters: PbS QDs vs. CdSe/ZnS QDs

In addition to CdSe/ZnS core/shell QDs, we have also studied PbS QDs via SHB. These dots were supplied to us by collaborators (Frank Wise's group at Cornell). The PbS QD sample we used experiences the lowest excitonic absorption at 791 nm. We performed SHB experiments at two different pump frequencies: 789.4 and 803.1 nm. The experiments revealed a broad acoustic phonon pedestal, but no sharp ZPL. The pedestal moved with the pump frequency, as expected. The lack of a sharp ZPL indicates a very fast dephasing time in the PbS dots. This is verified by unpublished photon-echo experiments performed by our collaborators. Their time-resolved experiments reveal only a fast decay component on the order of 100 fs or faster; the signals are at the limit of the instrument response. They found no slow decay component of the signal; a slow decay would be indicative of a ZPL.

Different time-resolved photoluminescence studies of ligand-capped PbS QDs reveal an extraordinarily long lifetime, on the order of 1 μs .⁹² At the same time, it has been found that the absorption bleaches quickly (<1 ns).⁹³ The surprising quickness of decoherence (despite long lifetimes) indicates unusually strong exciton-phonon interactions, possibly related to the high confinement energy experienced by the excitons.

We attribute the disappearance of the ZPL in the PbS QDs to the extremely strong exciton-phonon interaction in the material. The parameter of merit in this discussion is the Huang-Rhys parameter, S , discussed earlier. S describes the intensity ratio between the ZPL and the corresponding higher phonon sidebands in absorption, luminescence, or

Raman experiments. The parameter is equal to the interaction energy between excitons and phonons in units of the phonon energy. S is known to increase with increasing quantum confinement.⁹⁴ S for electron-phonon interactions *inside a QD* is given by the following expression:⁹⁵

$$S = \frac{2\pi}{\hbar\omega_{LO}} \left(\frac{1}{\epsilon_{\infty}} - \frac{1}{\epsilon_0} \right) \sum_k \frac{2}{R^3 j_{l+1}^2(kR)k^2} |v(k,l,m)|^2 \quad (5.15)$$

where R is the nanocrystal radius, and ω_{LO} could be replaced by the characteristic

frequency of any given phonon mode. $j_l(x)$ is the spherical Bessel function and

$$v(k,l,m) = \int j_l(kr) Y_l^m(\theta, \phi) \rho(r) dr, \text{ where } \rho(r) = |1P_e|^2 - |1S_e|^2.$$

S can be numerically calculated by using infinite boundary conditions and Bessel functions for $1S_e$ and $1P_e$. S scales approximately as $1/R$.

The quantum confinement in the two types of dots is different. While the exciton Bohr radius is 5.6 nm in CdSe, it is 20 nm in PbS. Excitons in PbS undergo *considerably* higher confinement energies at a given QD size than in CdSe QDs.⁹⁶ This is a predictable observation, based on the small band gap (0.4 eV) exhibited by bulk PbS. The confinement energies experienced by excitons in PbS QDs are several times the band gap energy in PbS QDs, versus about half the band gap energy in CdSe QDs.

Prior experiments have found that S values for 3 nm-wide PbS QDs could be segregated by type, with $S_{\text{acoustic}}=0.01-0.1$, and $S_{\text{optical}}=0.01-0.7$, depending on the l mode. The larger values of S are for lower values of l .⁹⁷ Reported values for CdSe QDs similarly exhibit a range from 0.035 to 1.3,^{73,98} and 0.2 for QDs embedded in glass or

organic matrices.⁷³ The 0.035 value is for epitaxially grown dots, 3 monolayers thick and 10 nm wide, coated with ZnS.⁹⁸ The other two values (1.3 and 0.2) are for colloidal dots, diameter 4.3 nm, with a ZnS shell.⁷³ $S_{\text{absorption}} = 0.2$ while $S_{\text{emission}} = 0.5$ for CdSe QDs of diameter 10 nm.⁹⁹ We take the value 0.2 for S in the case of CdSe/ZnS QDs embedded in polymer. The value for PbS most cited in the literature is 0.7, for a size of 3 nm. S only increases as dot size shrinks. A dependence of size versus S value may be inferred based on the data presented in Reference 100. We find the size of the PbS QD sample studied to be ~ 1.8 nm in diameter. Therefore, S for our PbS QD sample is, in all likelihood, more than 1.0. Based on the comparison of S for the two types of sample, PbS and CdSe/ZnS, we can state that exciton-phonon interactions in the PbS sample are considerably stronger than in the CdSe/ZnS samples.

We offer a possibility for the mechanism of stronger exciton-phonon interactions, and thus a higher S value, in PbS QDs. The extremely fast dephasing rate inferred from our results may be due to the so-called *external heavy atom effect*. Compounds containing atoms with particularly large Z -numbers (heavy atoms) respond to a spin-orbit coupling enhancement produced by the heavy atom. The enhanced spin-orbit interaction can increase the rate of a spin-forbidden process, thereby increasing the dephasing rate of excitons via an increase in the decoherence rate. The effect takes place due to the behavior of electrons in the presence of a heavy atom. The outermost electrons of such atoms are less tightly bound than in lighter atoms due to charge screening: the inner s-orbital electrons are attracted so strongly to the nucleus that they form a contracted, tight shell. The d- and f-orbitals are expanded and destabilized in response. Therefore the spin-

orbit interaction is much stronger for electrons associated with Pb atoms than it is for atoms associated with Cd. The heavy atom effect is known to reduce fluorescence quantum yield (QY) and the fluorescence lifetime, while increasing the phosphorescence QY and decreasing the phosphorescence lifetime.

Next, we examine the experimental results found for nanorods and compare them to the results for CdSe/ZnS quantum dots. Expected differences between exciton dephasing in sphere and rod morphologies are reviewed in the introduction to the next chapter.

CHAPTER 6

EXPERIMENTAL RESULTS FOR NANORODS AND CONCLUSIONS

In the previous chapter, we explored whether the size of the QD has an effect on the lowest achievable dephasing rate, and found that it did not. The size of the QD explicitly sets the phonon sideband energy we measure, as seen in Chapter Five. However, in terms of the ZPL, we need to ask if the size of the QD changes the coupling strength of the virtual transitions that cause broadening in the first place. In the theory of Muljarov, *et al.*,⁸³ the Hamiltonian describing virtual transitions is dependent on the wavefunctions of both electron and hole, and an integral over the radial component of the radius of the dot. Both wavefunctions are spherical, and their r dependence goes as e^{-r} . Integrated from 0 to R , the r -dependent parts of the two wavefunctions together returns $(-2)^{-1} (e^{-2R} - 1)$. This function, when graphed, is almost entirely flat across the range of R that we are concerned with. Therefore, it is reasonable that the lowest dephasing rate measured for each size of QD, after spectral diffusion has been minimized to the best of our abilities, should not vary from size to size.

We now consider whether shape plays a role in exciton dephasing. This is the first study of semiconductor nanorods using the SHB technique. We find that shape does promote different dephasing behavior. In fact, certain details in all the parameterizations that we investigate (modulation frequency, excitation intensity, and temperature) are

different than QDs in the case of nanorods. The material remains the same: CdSe/ZnS core/shell structures, with a further layer of trioctylphosphine oxide affixed to the ZnS. The nanorods explored in the present study have an aspect ratio of 9:1 (length \sim 21 nm, diameter \sim 2.4 nm). The length is nearly a factor of four longer than the Bohr radius of an exciton in bulk CdSe, but the rod is not yet sufficiently long to be considered a strictly 1-D system (a quantum wire). We find evidence of possible charge localization and migration within the rod structure.

CdSe/ZnS nanorods feature a Stokes shift of 50 nm between the exciton absorption and PL resonances at room temperature. The Stokes shift is predicted by Equation 5.5 and is proportional to S . S is inversely proportional to R (the radius of the nanostructure; see Equation 5.15). This indicates that as size decreases S increases, which we expect to cause a larger Stokes shift. This provides the first indication that excitons in nanorods may be undergoing some localization behavior. The diameter of the nanorods is only 2.4 nm, considerably less than the smallest diameter of QDs examined. PL of excitons in nanorods remains more red than expected for such a size, so we propose that the exciton is not strongly confined and has the ability to both migrate and elongate in the direction of the rod, which could explain a PL of 600 nm, as opposed to a PL near 500 nm for a QD of diameter 2.4 nm or a PL near 1260 nm for a QD of diameter 20 nm. There is a resonance shift of 10 nm from room temperature to 10 K (the PL peak occurs at 610 nm at room temperature, and 600 nm at 10 K), a smaller shift value than for CdSe/ZnS QDs. The amount of shift in QDs is different for every size, but averages to \sim 30 nm for our samples.

Given that nanorods have a large permanent dipole moment, it is worth asking whether pure dephasing in nanorods is qualitatively different than in quantum dots of the same material. The permanent dipole moment conceivably skews all polar interactions taking place in the rod morphology, but would not affect deformation potential coupling. Stronger polar interactions are expected to take place parallel to the long axis of the nanorod. A strong electric dipole moment may also act to elongate the exciton with more strength than simple geometric confinement can provide.

One somewhat puzzling observation is that acoustic phonon sidebands are not consistently visible in nanorod SHB spectra. We hypothesize that either a sufficiently large number of phonon modes participate, or the participating modes are directed along the long axis of the nanorods, such that the sidebands are broadened beyond recognition. For example, phonons traveling along the direction of the long-axis of the rod may have reached the continuous spectral range due to the relatively large distance and lack of confinement in that direction.

Spectral diffusion

Nanorods behave similarly to quantum dots under the influence of spectral diffusion. Effects of spectral diffusion can be suppressed by performing the SHB measurement at high modulation frequencies. As with QDs, the ZPL amplitude and width are both reduced at high modulation frequencies. The reasons are the same: the width is reduced due to removing a certain spectral range of spectral diffusion, and the amplitude is

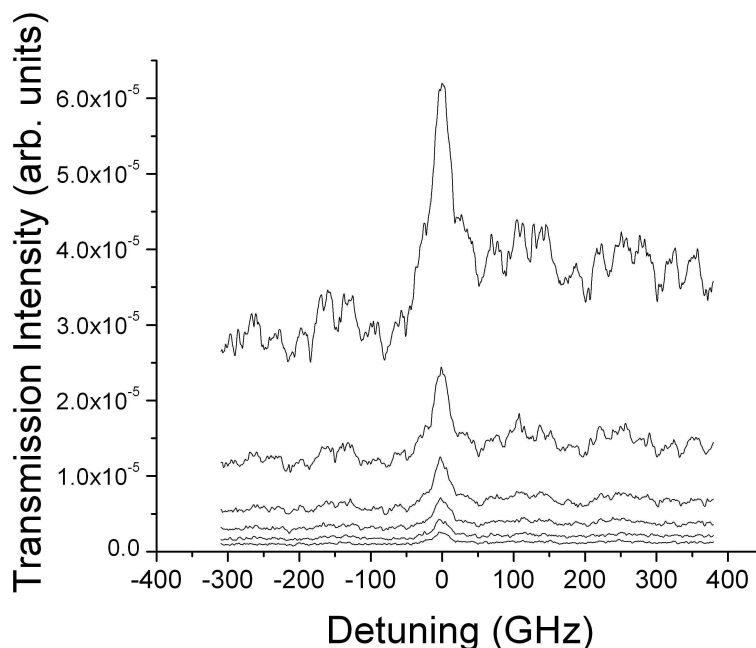


Figure 6-1: Nanorod ZPL in the SHB response observed at, for decreasing peak intensity, modulation frequencies of 1, 20, 40, 60, 80, and 100 kHz, respectively. For each datum, $T = 8$ K, pump intensity = 3 W/cm^2 , and probe intensity = 1 W/cm^2 .

reduced due to the effects of the long-lived dark state, which remains in play in nanorods (recall Chapter Two). The final decoherence rate we can achieve is comparable to, but higher than, the rate measured in QDs (see Figure 6-2). The QDs yield a minimum homogeneous linewidth (half of the SHB linewidth) of $6 \mu\text{eV}$, which corresponds to a decoherence rate of 0.75 GHz , as discussed previously. Our findings for nanorods include a minimum homogeneous linewidth of $38 \mu\text{eV}$, or a decoherence rate of $\sim 4.4 \text{ GHz}$. This is a slightly different finding than a previously published result that found the decoherence rate of nanorods to be less than in QDs.³⁶ The technique used in the referenced paper cannot account for low levels of spectral diffusion, and lacks the level of spectral resolution that we can achieve with SHB. The measured level of so-called

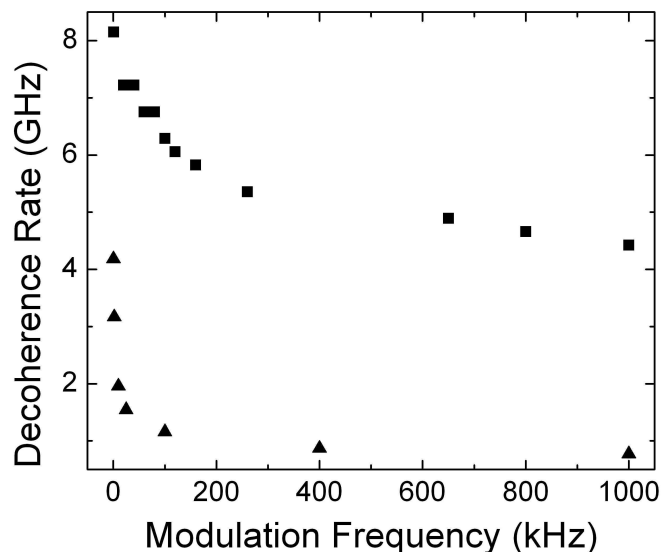


Figure 6-2: Decoherence rate versus modulation frequency for both nanorods (squares) and quantum dots (triangles). $T = 8$ K, pump intensity = 3 W/cm^2 , and probe intensity = 1 W/cm^2 .

spectral wandering in nanorods was found to be less than 7.2 GHz, showing spectral diffusion in nanorods to be small compared to spherical QDs in their study.

The relative effect of spectral diffusion that we measure on the exciton dephasing rate of nanorods (54%) is less than in spherical nanocrystals (75%). This result meets the expectation that as 0-D structures morph into 1-D structures the spectral diffusion should decrease to zero. Our findings for the relative change in linewidth due to spectral diffusion do match the aforementioned previously published result.³⁶

We observe that the effects of spectral diffusion in nanorods are greatly reduced in approximately the same frequency range as for QDs. The measurements for the decoherence rate in nanorods maintain a slight downward slope for over a greater frequency range than for QDs, indicating susceptibility to higher-frequency components of spectral diffusion.

It should be emphasized that due to our inability to measure the ZPL beyond a modulation frequency of about two MHz, it is unclear whether spectral diffusion at even higher frequencies takes place. At least some of the linewidth beyond the radiative width may be attributable to further spectral diffusion effects.

Power broadening

Nanorods undergo power broadening as do QDs. The broadening rate is more gradual than for QDs, as can be seen in Figure 6-3. A monotonic increase in the dephasing rate is both expected and observed. Figure 6-4 shows the same data plotted on a log scale. The trends for QDs and nanorods may be converging at very high intensity values.

Nanorods experience intensity-induced spectral diffusion, which acts as a power broadening, just as QDs do. We still excite the nanorods at excitation intensities well

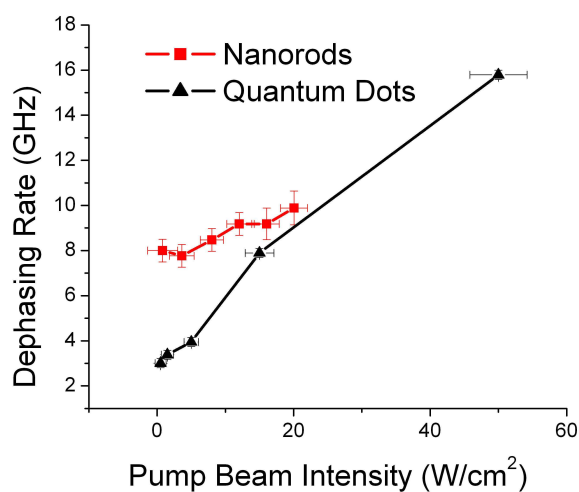


Figure 6-3: Dephasing rate versus pump beam intensity. Nanorods (squares) broaden at a more gradual rate than spherical nanocrystals (triangles). Modulation frequency = 1 kHz, $T = 8$ K, probe intensity = 1 W/cm^2 .

below the saturation intensity. The absorption cross section for nanorods is the same order of magnitude as QDs. Therefore, we conclude once again that the intensity-induced spectral diffusion plays the main role in the intensity dependence we observe for nanorods. It is reasonable that the intensity dependence of the two morphologies should begin to converge. The volumes of the two systems are similar. The energy density in the form of excitations contained in the spheres or rods becomes comparable in the limit of very high intensity, and the blinking events associated with this charging causes the observed increase in dephasing rate.

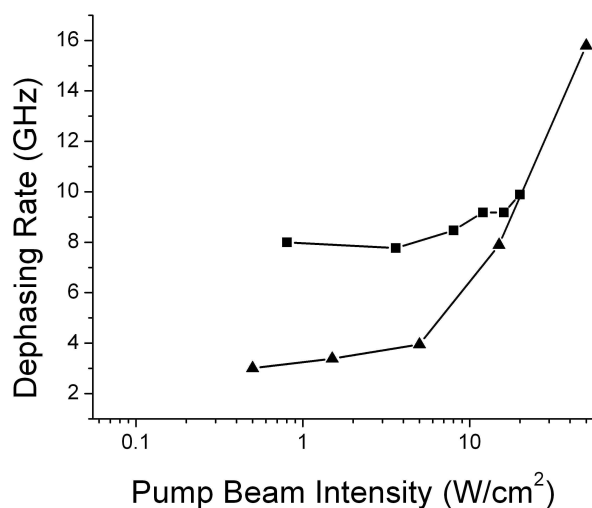


Figure 6-4: The pump beam intensity dependence for CdSe/ZnS nanorods (squares) and quantum dots (triangles) displayed on a log plot. Conditions are the same as in Figure 6-3.

Temperature dependence

As with spherical nanocrystals, the dephasing rate in nanorods is strongly affected by temperature. The dephasing rate rises rapidly with temperature, indicating a significant contribution to the decoherence of excitons from electron-phonon interactions (see Figure

6-5). Since the relative contribution of the ZPL to the SHB response decreases with increasing temperature, a deteriorating signal-to-noise ratio prevents us from obtaining data at temperatures above 25 K.

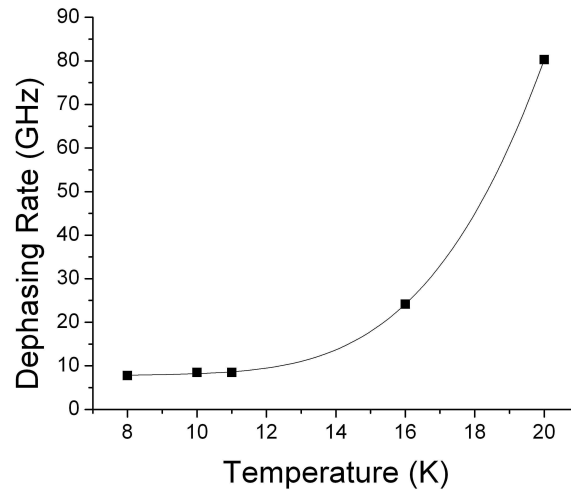


Figure 6-5: Temperature dependence of dephasing rate in nanorods. Modulation frequency = 1 kHz, pump intensity = 3 W/cm^2 , probe intensity = 0.3 W/cm^2 . The line is a fit described by Equation 5.14.

Virtual transitions remain the most likely source of the temperature-dependent ZPL linewidth. The data points can be fit by the same equation used for QDs, Equation 5.14. E_a , E_b , and Γ_{rad} remain the same as in that case (.67 meV, 1.5 meV, and $16 \mu\text{eV}$, respectively, but the parameters A and B are now 44.9 and $40.7 \mu\text{eV}$, respectively, an order of magnitude larger than in the QD case. (NB: it is easy to obtain unphysical quantities fitting this function, and care should be taken.) Remember that this is a numerical fit, and the physical model of the interaction with two phonon energies is not necessarily correct.

Conclusions

We find that exciton-phonon interactions account for the majority of exciton dephasing that takes place in CdSe/ZnS quantum dots and nanorods. This is the first study²¹ of the dephasing rate of CdSe/ZnS nanorods with spectral diffusion effects minimized, and at high spectral resolution compared to the limited earlier experiments.³⁶ Suppressing the effects of spectral diffusion reduces the measured linewidth dramatically, but does not allow that linewidth to closely approach the expected radiative linewidth in either morphology. Temperature and excitation intensity must both be small in order to obtain the lowest linewidth possible. The minimum decoherence rate in nanorods is observed to be larger than in QDs. However, the relative effect of spectral diffusion on the measured linewidth is smaller in nanorods than it is in quantum dots. This behavior is expected as a symptom of the transition from 0-D to 1-D semiconductor nanostructures.

Temperature dependence of the SHB response indicates strong exciton-phonon interactions in the nanorod and quantum dot structures. Excitation intensity dependence derives from either saturation (due to excitation of the absorption tails of non-resonant nanocrystals) or intensity-dependent spectral diffusion processes. A measurement timescale-dependence is an indication that low frequency spectral diffusion dominates the SHB response at long integration timescales. Nevertheless, at the highest modulation frequency used, the lowest decoherence rate obtained for both morphologies exceeds the expected radiative (lifetime) rate of excitons in CdSe, ~ 0.016 GHz, by a large factor.

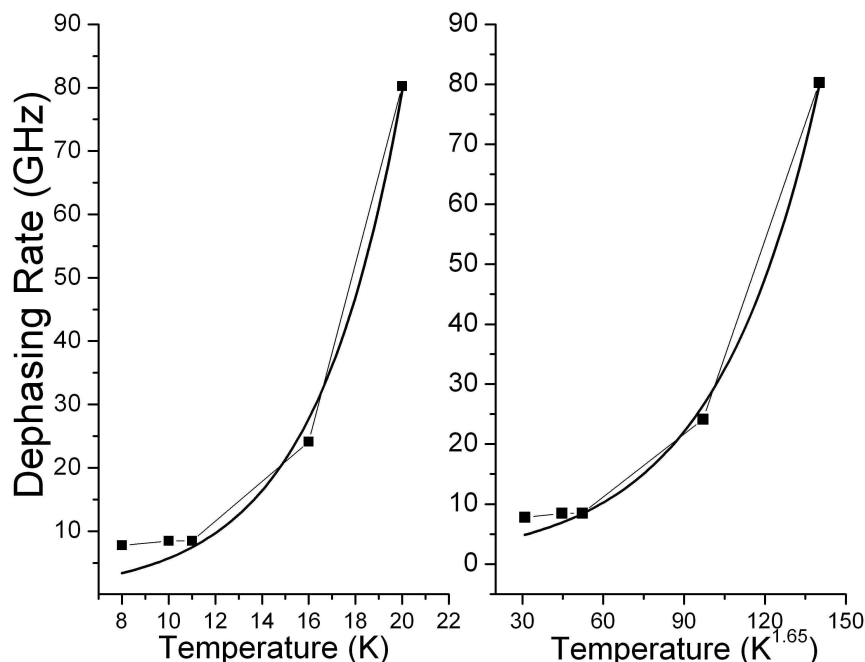


Figure 6-6: The same temperature data given in Figure 6.5 for nanorods. The fit on the left is a standard exponential fit. The fit on the right is a standard exponential fit for a temperature dependence of $T^{1.65}$ (see the text). The thin lines are guides.

The question remains: what causes decoherence in excess of the radiative dephasing rate? Decoherence mechanisms in nanocrystals are still poorly understood. For spherical nanocrystals, decoherence rates obtained at high modulation frequency are comparable to those obtained in self-assembled quantum dots, and these rates consistently exceed the expected radiative rate.^{90,91} The linewidth of the ZPL in nanorods is also much greater than the expected radiative linewidth, and in excess of the linewidth of QDs as well. In addition to not being able to quantify any spectral diffusion taking place at frequencies above two MHz, the ways in which electron-phonon interactions contribute to the linewidth of the ZPL are still debated.⁸³

We propose a mechanism to help explain the additional decoherence of excitons in nanorods as compared with spherical quantum dots. This is the exciton localization and migration model discussed briefly earlier. In comparison to spherical nanocrystals, excitons in nanorods can become localized by fluctuations in the 1-D confinement potential. The fluctuations might arise from imperfect nanorod growth leading to crystal lattice defects or surface fluctuations, or strain at the CdSe-ZnS boundary caused by the 12% lattice mismatch of the two materials. Migrations of excitons among different localization sites with local potential minima can take place via absorption or emission of acoustic phonons. The phonon-assisted migration process persists and can be highly effective even at very low temperature, as shown in earlier studies of localized excitons in GaAs/AlGaAs quantum wells.¹⁰¹

The expected temperature dependence of a phonon-assisted migration process has the form $\exp(BT^\alpha)$, at least in multiple quantum well structures. B is positive and independent of the temperature, although it is expected to depend on the excitation energy and details of the nanostructure boundaries. α is estimated to be between 1.6 and 1.7.¹⁰² The temperature dependence of the nanorods is plotted again in Figure 6-6. The first plot is a generic exponential fit to the data, and takes the form $0.41\exp(0.263T)$. The fit is not especially close. When the data is replotted with an x-axis of $T^{1.65}$, and subsequently refitted with an exponential, the fit is closer. This variety of temperature dependence supports but is not conclusive about the model of acoustic phonon-assisted migration as a plausible source of decoherence in our nanorod system.

A greater source of confidence for the proposed mechanism is the dimension-dependent behavior of the dephasing rate. The dephasing rate in nanorods follows trends and behaves more like a 0-D exciton (implying confinement) than a 1-D exciton. For example, the effects of spectral diffusion for a nonlocalized, true 1-D exciton should be essentially zero and certainly less than for a fully confined exciton, as discussed in Chapter Four. The *relative* contribution of spectral diffusion is less than for QDs, but only by one third of the value for QDs. We speculate that if localization were not taking place, the relative contribution of spectral diffusion to the decoherence rate would be dramatically lower than in QDs.

Excitons undergoing phonon-assisted migration are subject to dephasing due to elastic scattering from potential fluctuations, as well as the dephasing discussed previously that is due to exciton recombination and exciton-phonon scattering.¹⁰² Between hops to new locations within the nanostructure the localized exciton is confined by a local minimum of the potential. Migration requires absorption or emission of an acoustic phonon to compensate for the energy difference between sites. There are two mechanisms for migration. In the first, sites must be nearby to one another, on the scale of an excitonic wavefunction, since it is the overlap of the excitonic wavefunction with a different local energy minimum is the cause of the migration itself. In the second, the inter-site distance is much greater than the localization length, and the intersite dipole-dipole interaction mediates the interaction.¹⁰³ A model for exciton states in a random potential, assuming transport over relatively large distances and exciton-phonon interaction that is confined to phonons of long wavelength, is detailed in an early

paper.¹⁰⁴ Strong quantum confinement is not considered in the model. Additionally, recall that the nanorods demonstrate a permanent electric dipole. This overall dipole could deeply affect both of the mechanisms mentioned here, in likelihood affecting the second mechanism most strongly.

Further evidence for migration is the blinking behavior of quantum wires. A recent report¹⁰⁵ indicates that for a fraction of the number of 1.3 μm -long wires studied, different portions of the CdSe quantum wires blink. The blinking is observed to change location within the wire structure. The statistics investigating whether correlations exist between blinking in different parts of a rod had not been completed at the time of the report. Localized blinking behavior indicates localized excitons, which is indirect support of exciton localization and migration taking place in the nanorods.

Thus, phonon-assisted migration is a likely mechanism for decoherence in 1-D nanorods above that seen in QDs. In principle, improved nanorod synthesis could overcome this dephasing mechanism.

CHAPTER 7

SUMMARY AND OUTLOOK

We have shown that CdSe/ZnS core/shell nanorods feature faster dephasing than CdSe/ZnS core/shell quantum dots. A mechanism for faster dephasing in the nanorod morphology is exciton localization and phonon-assisted migration within the rod structure. While this mechanism can account for the faster decoherence time in nanorods, it remains to be experimentally tested. External evidence for the validity of this mechanism comes from the study of blinking behavior of long CdSe quantum wires.¹⁰⁵ Most wires observed blink as a unit along the entire length of the wire. However, some wires blink from discrete regions, and the blinking moves with time. This seems to support our exciton localization and migration model. It also suggests that an appropriate way to try to reduce the large decoherence rate in nanorods is to concentrate on better synthesis methods that may reduce potential energy fluctuations along the length of the rods.

Second, we observe that the relative effects of spectral diffusion on the dephasing rate in nanorods is less than in quantum dots. For both morphologies the dephasing rate drops by nearly 4 GHz over a modulation frequency range of 1 kHz-1MHz. However, due to the higher overall decoherence rate observed in nanorods, the amount of dephasing attributable to spectral diffusion at low frequency is only 54%, while in quantum dots it is 75%. The lower relative effect of spectral diffusion in nanorods may be due to the larger

size of the nanorod structure. Spectral diffusion is caused by a conformational change that modifies the transition energy of the whole structure. It is possible that the size of the nanorod is such that it takes a much larger change to modify the transition energy appreciably. There is also the consideration of the nearly 1-D excitons that form in the nanorods, and the types of perturbations that could affect the potential well that confines them.

Finally, we note that nanorods are closer to being radiative lifetime-limited than quantum dots. This is largely due to the difference in expected radiative lifetime in the two morphologies. In quantum dots the radiative lifetime is about 10 ns, leading to a dephasing rate of about 0.016 GHz (or a homogeneous rate, more often quoted, of about 0.03 GHz). The lowest decoherence rate measured in quantum dots is 0.75 GHz. This is 47 times larger than the radiative rate.

In nanorods, the radiative lifetime has been calculated to be about 0.8 ns, yielding a rate of 0.2 GHz. The lowest decoherence rate measured in nanorods is 4.4 GHz. While this value is considerably larger than for quantum dots, it is only a factor of 22 larger than the radiative rate. This leads to the conclusion that nanorods are closer to being radiative lifetime-limited. If the decoherence rate of nanorods can be shrunk to a value close to that of quantum dots, then the nanorods would display a decoherence rate only a factor of ~ 5 away from the lifetime rate.

In conclusion, while lifetime-limited dephasing has not yet been observed in CdSe/ZnS core/shell quantum dots or nanorods, the study of decoherence effects ascribed to spectral diffusion and electron-phonon interaction is fundamentally important. The

understanding of dephasing processes, and the ability to observe the homogeneous linewidth of an optical transition in the absence or near-absence of extraneous dephasing, opens the door to many applications including optical communications networks and information processing. Greater control of the synthesis of these nanostructures may yield systems with decoherence rates even lower than those observed in the course of the studies presented here, bringing the above applications and others not yet anticipated even closer to fruition.

BIBLIOGRAPHY

- ¹ J. K. Jaiswal, H. Mattoussi, J. M. Mauro, and S. M. Simon, *Nature Biotechnology* **21** (1), 47 (2003).
- ² X. Michalet, F. Pinaud, T. D. Lacoste, M. Dahan, M. P. Bruchez, A. P. Alivisatos, and S. Weiss, *Single Molecules* **2** (4), 261 (2001).
- ³ X. H. Gao, W. C. W. Chan, and S. M. Nie, *Journal of Biomedical Optics* **7** (4), 532 (2002).
- ⁴ E. U. Rafailov, A. D. McRobbie, M. A. Cataluna, L. O'Faolain, W. Sibbett, and D. A. Livshits, *Applied Physics Letters* **88** (4) (2006).
- ⁵ Y. Sugimoto, K. Inoue, N. Ikeda, S. Ohkouchi, Y. Tanaka, Y. Nakamura, H. Nakamura, H. Sasaki, K. Ishida, and K. Asakawa, *Ieee Journal of Selected Topics in Quantum Electronics* **11** (5), 1055 (2005).
- ⁶ P. G. Eliseev, H. Li, A. Stintz, G. T. Liu, T. C. Newell, K. J. Malloy, and L. F. Lester, *Applied Physics Letters* **77** (2), 262 (2000).
- ⁷ M. Pelton and Y. Yamamoto, *Physical Review A* **59** (3), 2418 (1999).
- ⁸ P. K. Basu, *Theory of optical processes in semiconductors : bulk and microstructures*. (Clarendon Press, Oxford University Press, Oxford, New York, 1997).
- ⁹ M. J. Kelly, *Low-dimensional semiconductors : materials, physics, technology, devices*. (Clarendon Press, Oxford University Press, Oxford, New York, 1995).
- ¹⁰ Y. Zhou, L. P. Liu, C. Etsion, Y. Abranyos, A. Padilla, and Y. C. Chen, *Applied Physics Letters* **84** (16), 3025 (2004).
- ¹¹ A. Rosen, P. J. Stabile, D. W. Bechtle, W. Janton, A. M. Gombar, J. McShea, A. Rosenberg, P. R. Herczfeld, and A. Bahasadri, *Ieee Transactions on Electron Devices* **36** (2), 367 (1989).
- ¹² M. Larsson, Linkoping University, 2005.
- ¹³ A. R Peaker and H. G Grimmeiss, *Low-dimensional structures in semiconductors : from basic physics to applications*. (Plenum Press, New York, 1991).

- ¹⁴ K. R. Brown, D. A. Lidar, and K. B. Whaley, *Physical Review A* **65** (1) (2002).
- ¹⁵ T. A. Brun and H. L. Wang, *Physical Review A* **61** (3), art. no. (2000).
- ¹⁶ J. Schrier and K. B. Whaley, *Physical Review B* **72** (8) (2005).
- ¹⁷ P.C. Ku, F. Sedgwick, C.J. Chang-Hasnain, P. Palinginis, T. Li, H. Wang, S.W. Chang, and S.L. Chuang, *Optics Letters* **29** (19), 2291 (2004).
- ¹⁸ M. Phillips and H. Wang, *Phys. Rev. Lett.* **89** (18), 186401 (2002).
- ¹⁹ S. Sarkar, P. Palinginis, P. C. Ku, C. J. Chang-Hasnain, N. H. Kwong, R. Binder, and H. Wang, *Physical Review B* **72** (3) (2005).
- ²⁰ P. Palinginis, S. Tavenner, M. Lonergan, and H. Wang, *Phys. Rev. B* **67** (no. 20), 201307 (2003).
- ²¹ S. Tavenner-Kruger, Y.S. Park, M. Lonergan, U. Woggon, and H. Wang, *Nano Letters* (accepted) (2006).
- ²² Website of Competence Centre for the Application of Nanostructures in Optoelectronics, (Bundesministerium für Bildung und Forschung, Berlin, 2006).
- ²³ H. C. Chen, C. W. Wang, S. W. Lee, and L. J. Chen, *Advanced Materials* **18** (3), 367 (2006).
- ²⁴ H. J. Kim, J. Y. Chang, and Y. H. Xie, *Journal of Crystal Growth* **247** (3-4), 251 (2003).
- ²⁵ D. Bimberg, N. N. Ledentsov, M. Grundmann, N. Kirstaedter, O. G. Schmidt, M. H. Mao, V. M. Ustinov, A. Y. Egorov, A. E. Zhukov, P. S. Kopev, Z. I. Alferov, S. S. Ruvimov, U. Gosele, and J. Heydenreich, *Japanese Journal of Applied Physics Part 1-Regular Papers Short Notes & Review Papers* **35** (2B), 1311 (1996).
- ²⁶ M. Hines and P. Guyot-Sionnest, *J. Phys. Chem. B* **100**, 468 (1996).
- ²⁷ M. J. Lee, *Metals and Materials International* **9** (1), 83 (2003).
- ²⁸ Taleb Mokari and Uri Banin, *Chem. Mater.* **15**, 3955 (2003).
- ²⁹ R. J. Qi, Y. J. Zhu, G. F. Cheng, and Y. H. Huang, *Nanotechnology* **16** (11), 2502 (2005).
- ³⁰ C. S. Carr and D. F. Shantz, *Chemistry of Materials* **17** (24), 6192 (2005).

- ³¹ Y. W. Jun, J. W. Seo, S. J. Oh, and J. Cheon, *Coordination Chemistry Reviews* **249** (17-18), 1766 (2005).
- ³² X. G. Peng, L. Manna, W. D. Yang, J. Wickham, E. Scher, A. Kadavanich, and A. P. Alivisatos, *Nature* **404** (6773), 59 (2000).
- ³³ Z. A. Peng and X. G. Peng, *Journal of the American Chemical Society* **123** (7), 1389 (2001).
- ³⁴ M. Nirmal and L. Brus, *Accounts of Chemical Research* **32** (5), 407 (1999).
- ³⁵ A. Shabaev and A. L. Efros, *Nano Letters* **4** (10), 1821 (2004).
- ³⁶ N. Le Thomas, E. Herz, O. Schops, U. Woggon, and M. V. Artemyev, *Physical Review Letters* **94** (1), 016803 (2005).
- ³⁷ A. Shabaev and A. Efros, *Bulletin of the American Physical Society* **49** (1), J11 (2004).
- ³⁸ W.U. Huynh, J.J. Dittmer, and A.P. Alivisatos, *Science* **295** (5564), 2425 (2002).
- ³⁹ C. F. Klingshirn, *Semiconductor optics*. (Springer, Berlin, New York, 1995).
- ⁴⁰ M.L. Cohen and J.R. Chelikowsky, in *Springer series in solid-state sciences ; 75*, 1989 (Springer-Verlag, Berlin, New York, 1989).
- ⁴¹ D. J. Norris and M. G. Bawendi, *Physical Review B* **53** (24), 16338 (1996).
- ⁴² M. Nirmal, D. J. Norris, M. Kuno, M. G. Bawendi, A. L. Efros, and M. Rosen, *Physical Review Letters* **75** (20), 3728 (1995).
- ⁴³ U. Bockelmann and T. Egeler, *Phys. Rev. B* **46** (23), 15574 (1992).
- ⁴⁴ A. I. Ekimov, F. Hache, M. C. Schanneklein, D. Ricard, C. Flytzanis, I. A. Kudryavtsev, T. V. Yazeva, A. V. Rodina, and A. L. Efros, *Journal of the Optical Society of America B-Optical Physics* **11** (3), 524 (1994).
- ⁴⁵ L. E. Brus, *Journal of Chemical Physics* **80** (9), 4403 (1984).
- ⁴⁶ Phedon Palinginis, *Dissertation, University of Oregon*, 2004.
- ⁴⁷ J.M. Luttinger, *Physical Review* **102** (4), 1030 (1956).

- ⁴⁸ Peter Y. Yu and Manuel Cardona, *Fundamentals of semiconductors : physics and materials properties*, 3rd, rev. and enlarged ed. (Springer, Berlin, New York, 2001).
- ⁴⁹ G.K. Woodgate, *Elementary Atomic Structure*, Second ed. (Clarendon Press, Oxford, 1992).
- ⁵⁰ R.S. Knox, *Theory of Excitons*. (Academic Press, New York, 1963).
- ⁵¹ H. T. Grahn, in *Semiconductor physics* (World Scientific, Singapore, London, 1999).
- ⁵² A. L. Efros, M. Rosen, M. Kuno, M. Nirmal, D. J. Norris, and M. Bawendi, *Physical Review B* **54** (7), 4843 (1996).
- ⁵³ A. L. Efros and A. V. Rodina, *Physical Review B* **47** (15), 10005 (1993).
- ⁵⁴ J. T. Hu, L. S. Li, W. D. Yang, L. Manna, L. W. Wang, and A. P. Alivisatos, *Science* **292** (5524), 2060 (2001).
- ⁵⁵ D. Katz, T. Wizansky, O. Millo, E. Rothenberg, T. Mokari, and U. Banin, *Physical Review Letters* **89** (19) (2002).
- ⁵⁶ X. Y. Wang, J. Y. Zhang, A. Nazzal, M. Darragh, and M. Xiao, *Applied Physics Letters* **81** (25), 4829 (2002).
- ⁵⁷ D. Steiner, D. Katz, O. Millo, A. Aharoni, S. Kan, T. Mokari, and U. Banin, *Nano Letters* **4** (6), 1073 (2004).
- ⁵⁸ P. C. Sercel and K. J. Vahala, *Physical Review B* **44** (11), 5681 (1991).
- ⁵⁹ B. O. Dabbousi, J. Rodriguez-Viejo, F. V. Mikulec, J. R. Heine, H. Mattoussi, R. Ober, K. F. Jensen, and M. G. Bawendi, *J. Phys. Chem. B* **101** (46), 9463 (1997).
- ⁶⁰ A. Creti, M. Anni, M.Z. Rossi, G. Lanzani, G. Leo, F. Della Sala, L. Manna, and M. Lomascolo, *Physical Review B* **72** (12), 125346 (2005).
- ⁶¹ L. Manna, E.C. Scher, and A.P. Alivisatos, *Journal of Cluster Science* **13** (4), 521 (2002).
- ⁶² L. Manna, L.W. Wang, R. Cingolani, and A.P. Alivisatos, *Journal of Physical Chemistry B* **109** (13), 6183 (2005).
- ⁶³ E.C. Scher, L. Manna, and A.P. Alivisatos, *Philosophical Transactions of the Royal Society London, Series A* **361** (1803), 241 (2003).

- ⁶⁴ X. Fan, University of Oregon, 2000.
- ⁶⁵ M. Kuno, J. K. Lee, B. O. Dabbousi, F. V. Mikulec, and M. G. Bawendi, *J. Phys. Chem.* **106**, 9869 (1997).
- ⁶⁶ X. Peng, M. C. Schlamp, A. V. Kadavanich, and A. P. Alivisatos, *J. Am. Chem. Soc.* **119**, 7019 (1997).
- ⁶⁷ S.L. Cumberland, K.M. Hanif, A. Javier, G.A. Khitrov, G.F. Strouse, S.M. Woessner, and C.S. Yun, *Chem. Mater.* **14** (4), 1576 (2002).
- ⁶⁸ C. R. Kagan, C. B. Murray, and M. G. Bawendi, *Phys. Rev. B* **54**, 8633–8643 (1996).
- ⁶⁹ S. V. Gaponenko, *Optical properties of semiconductor nanocrystals.* (Cambridge University Press, Cambridge, UK ; New York, NY, USA, 1998).
- ⁷⁰ Marlan O. Scully and Muhammad Suhail Zubairy, *Quantum optics.* (Cambridge University Press, Cambridge ; New York, 1997).
- ⁷¹ S. V. Goupalov, R. A. Suris, P. Lavallard, and D. S. Citrin, *IEEE Journal of Selected Topics in Quantum Electronics* **8** (5), 1009 (2002).
- ⁷² M. Grundmann, J. Christen, N.N. Ledentsov, J. Böhrer, D. Bimberg, S.S. Ruvimov, P. Werner, U. Richter, U. Gösele, J. Heydenreich, V.M. Ustinov, A.Yu. Egorov, A.E. Zhukov, P.S. Kop'ev, and Z.I. Alferov, *Phys. Rev. Lett.* **74** (20), 4043–4046 (1995).
- ⁷³ S.A. Empedocles, D.J. Norris, and M.G. Bawendi, *Phys. Rev. Lett.* **77** (18), 3873–3876 (1996).
- ⁷⁴ S. Asaka, H. Nakatsuka, M. Fujiwara, and M. Matsuoka, *Phys. Rev. A* **29** (4), 2286–2289 (1984).
- ⁷⁵ V.I. Prokhorenko and A.R. Holzwarth, *J. Phys. Chem. B* **104** (48), 11563 (2000).
- ⁷⁶ C.B. Duke and G.D. Mahan, *Phys. Rev.* **139**, A1965 (1965).
- ⁷⁷ Y. Masumoto and T. Takagahara, *Semiconductor quantum dots : physics, spectroscopy, and applications.* (Springer, Berlin ; New York, 2002).
- ⁷⁸ Pierre Meystre and Murray Sargent, *Elements of quantum optics*, 3rd ed ed. (Springer, New York, 1999).

- ⁷⁹ John David Jackson, Classical electrodynamics, 3rd ed ed. (Wiley, New York, 1999).
- ⁸⁰ T. Takagahara, J. Lumin. **70**, 129 (1996).
- ⁸¹ Walter A. Harrison, Solid State Theory. (McGraw-Hill, New York, 1970).
- ⁸² A.A. Gusev, M.M. Zehnder, and U.W. Suter, Phys. Rev. B **54** (1), 1 (1996).
- ⁸³ E.A. Muljarov, T. Takagahara, and R. Zimmermann, Phys. Rev. Lett. **95**, 177405 (2005).
- ⁸⁴ A. Biebricher, M. Sauer, and P. Tinnefeld, Journal of Physical Chemistry B **110** (11), 5174 (2006).
- ⁸⁵ Z. Wang, K. Reimann, M. Woerner, T. Elsaesser, D. Hofstetter, J. Hwang, W. J. Schaff, and L. F. Eastman, Physica E-Low-Dimensional Systems & Nanostructures **32** (1-2), 562 (2006).
- ⁸⁶ I. S. Osad'ko, Physics-Uspekhi **49** (1), 19 (2006).
- ⁸⁷ D. E. Gomez, J. van Embden, and P. Mulvaney, Applied Physics Letters **88** (15) (2006).
- ⁸⁸ M. Ikezawa and Y. Masumoto, Phys. Rev. B **61** (19), 12662 (2000).
- ⁸⁹ P. Palinginis and H. Wang, App. Phys. Lett. **78** (11), 1541 (2001).
- ⁹⁰ P. Palinginis, H. Wang, S.V. Goupalov, D.S. Citrin, M. Dobrowolska, and J.K. Furdyna, Phys. Rev. B **70**, 073302 (2004).
- ⁹¹ P. Borri, W. Langbein, S. Schneider, U. Woggon, R. L. Sellin, D. Ouyang, and D. Bimberg, Physical Review Letters **87** (15), 157401 (2001).
- ⁹² Jamie H Warner, Elizabeth Thomsen, Andrew R Watt, Norman R Heckenberg, and Halina Rubinsztein-Dunlop, Nanotechnology **16** (2), 175 (2005).
- ⁹³ F. Huang, A. Filin, P. Rao, and P. Persans, presented at the APS March Meeting, Indiana, 2002 (unpublished).
- ⁹⁴ M. Bissiri, G.B. Hoeger von Hoegersthal, A.S. Bhatti, M. Capizzi, and A. Frova, Phys. Rev. B **62** (7), 4642 (2000).
- ⁹⁵ M. Shim and P. Guyot-Sionnest, Phys. Rev. B **64**, 245342 (2001).

- ⁹⁶ F.W. Wise, *Acc. Chem. Res.* **33** (11), 773 (2000).
- ⁹⁷ T.D. Krauss and F.W. Wise, *Phys. Rev. Lett.* **79** (25), 5102 (1997).
- ⁹⁸ F. Gindele, K. Hild, W. Langbein, and U. Woggon, *Phys. Rev. B* **60**, R2157 (1999).
- ⁹⁹ D.J. Norris, Al. L. Efros, M. Rosen, and M.G. Bawendi, *Phys. Rev. B* **53** (24), 16347 (1996).
- ¹⁰⁰ R.S. Silvaa, A.F.G. Montea, P.C. Moraisa, A.M. Alcaldeb, F. Quc, and N.O. Dantas, *Brazilian Journal of Physics* **36** (2A), 394 (2006).
- ¹⁰¹ T. Takagahara, *Phys. Rev. B* **32**, 7013 (1985).
- ¹⁰² H. Wang, M. Jiang, and D.G. Steel, *Phys. Rev. Lett.* **65** (10), 1255 (1990).
- ¹⁰³ T. Takagahara, *J. Lumin.* **44**, 347 (1989).
- ¹⁰⁴ E. Cohen and M.D. Sturge, *Phys. Rev. B* **25** (6), 3828 (1982).
- ¹⁰⁵ J.J. Glennon, R. Tang, R.A. Loomis, and W.E. Buhro, presented at the Materials Research Society Spring Meeting, San Francisco, 2006 (unpublished).
- ¹⁰⁶ R.G. Neuhauser, K.T. Shimizu, W.K. Woo, S.A. Emedocles, M.G. Bawendi *Phys. Rev. Lett.* **85**, 3301 (2000)

APPENDIX A

NANOCRYSTAL SYNTHESIS

The purpose of this appendix is to provide the reader with detailed (although not entirely complete) instructions for the growth of CdSe/ZnS core/shell spherical nanocrystals. Recipes for the stock solutions are given, as are the procedures for the fabrication of the nanocrystals. The format is pedantic, and some material may be found in duplicate in Chapter Three as well. It is recommended that the student not familiar with air-free or organo-metallic synthetic procedures consult with an expert before beginning. The materials are dangerous, and the procedures may be delicate in places. This document is not intended to be the sole source of information for a budding nanocrystal-grower. Nevertheless, I have included all the important points for achieving high quality crystals, and sufficient directions for a properly prepared physics student. Enjoy, and good luck.

Safety notes:

- For all procedures, wear nitrile gloves and substantial eye protection (in the form of chemistry goggles or eyeglasses), and be sure to keep the hood sash down in front of yourself as far as is practical to work with. In addition, be sure that the sash is below the line demarking

most effective airflow range. Note that nitrile gloves do NOT protect well against chloroform.

- Me_2Cd and Me_2Zn are very reactive with air and water. More specifically, the oxygen in air and water readily reacts with these materials and can cause rapid oxidation (burning) and explosion. It is very important that all materials which come into contact with the $\text{Me}_2\text{Cd/Zn}$ be dry and under a nitrogen or other inert atmosphere.
- Take care to treat all the substances with respect. Nearly every one of them is actively toxic and some are considered possible or known carcinogens.
- Clean up after yourself and be sure use proper waste disposal procedures. Items which have come into contact with the synthesis materials need to be either cleaned thoroughly, with the waste going into the proper receptacle, or disposed of in a specially-marked container labeled with the contaminating substance.

Recipe for cadmium selenide (CdSe) stock solution

Materials

24 mL trioctylphosphine, which I will call TOP

0.2 g selenium

0.25 mL dimethyl cadmium, which I will call Me_2Cd

dry nitrogen Schlenk line at about two to three psi of pressure; needle attachment

4 dry 20 or 18 gauge cannulae (to be referred to as cannulae A, B, C, D)

25 mL glass graduated cylinder

about 10-20 mL acetone for cleaning

about 15 mL tertiary butyl alcohol for cleaning

about 10 mL methanol for cleaning

rubber septum to fit top of graduated cylinder

round-bottom glass storage flask with a sidearm

rubber septum to fit top of storage vessel

teflon stopper with vicon o-ring to isolate sidearm from air

15 mL pear flask with a mark denoting 0.25 mL

rubber septum to fit top of pear flask

sonicator

plastic weighing dish

weighing paper to make funnel for Se

spatula

plastic syringe body and septum to fit outlet for cleaning

sufficient solvent and waste beakers

nitrile gloves

multiple syringes and long Luer-lock needles

copper wire for securing septa on all glassware

Directions

1. Prepare cleaning stations.
 - a. Fill plastic syringe with acetone. Place rubber septum over outlet to prevent leaking. Prepare and label waste beaker for acetone.
 - b. Warm tertiary-butyl alcohol until melted. Prepare clean and waste beaker.
 - c. Prepare clean and waste beakers for methanol.
 - d. Prepare clean and waste beakers for bleach.
2. Weigh out dry selenium into plastic dish using a spatula to transfer the material. Form weighing paper into funnel, insert it into the storage flask, and gently encourage the Se powder into the flask with the spatula.
3. Place rubber septa firmly into graduated cylinder and storage flask. Screw teflon stopper into the sidearm and do not close all the way. Attach tube from sidearm to the bubbler and to the Schlenk line (there is a "T" in the tube).
4. Purge N₂ line (with needle attachment) with nitrogen, followed by the bottle of TOP and canula A, and then the graduated cylinder and canula B, and finally the storage flask through the bubbler. See Figure A-1.

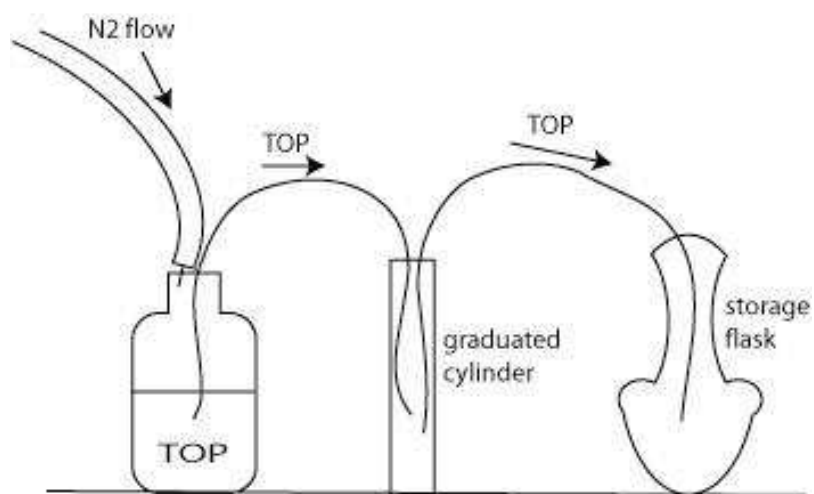


Figure A-1: Schematic of the TOP transfer cascade.

5. Push full amount of TOP into graduated cylinder.
6. Remove canula A, move N₂ line to cylinder, clean canula A with acetone by sticking it into the syringe of acetone (through septum) and pushing acetone through it into the waste beaker. Then pull more solvent from clean acetone beaker and repeat twice more.
7. Push 4.5 mL TOP from cylinder to flask.
8. Sonicate TOP and Se together until Se is dissolved in the TOP (swirling by hand speeds up the process). Stop sonication when complete.
9. Opening the Me₂Cd can and removing the Me₂Cd is slightly complex.
 - a. Tightly clamp pear flask and place rubber septum on top; secure with wire.
 - b. Hold metal top of Me₂Cd can securely with a wrench as you twist out the top screw with the lever wrench (which should be wired to the can

while the can is in storage). Then, screw on the brass piece with a fresh rubber septum held on securely with a hose clamp.

- c. Purge headspace inside brass piece and canula C.
 - d. Purge pear flask and cannula D.
 - e. Install lever on can and open valve by moving lever up.
 - f. Push canula C straight down to bottom of can (right in the middle ; otherwise it will hit the walls of the valve and stick).
 - g. Transfer full amount of Me_2Cd to pear flask.
 - h. Pull canula C up above the level of the valve and close the valve with the lever.
 - i. Transfer Me_2Cd to storage flask with canula D. If too much was transferred use a cool 0.5 mL gastight syringe instead to transfer the proper amount.
 - j. Pull out canula C, and clean with tertiary-butyl alcohol (t-ba), followed by methanol. There is a chance the t-ba will freeze in the canula. Should this occur, heat in the oven to melt to liquid again and continue the cleaning process.
 - k. Clean pear flask by very slowly adding t-ba with an additional outlet needle in the septum until no more gas evolves, then rinse with methanol.
10. Transfer rest of TOP to flask.
 11. Clean things that were exposed to TOP with acetone.

12. Close teflon stopper on flask. Switch bubbler line for N₂ line. Open stopper, remove septum, cap flask securely, close stopper securely, and finally wrap flask in foil to prevent light degradation of the solution.

Note that the CdSe stock solution has a short shelf-life; it is good for a few weeks while the ZnS solution can last up to a few months. Avoid selecting the cloudy patches that develop in the CdSe solution when you remove some with a needle for nanocrystal growth.

Recipe for zinc sulfide (ZnS) stock solution

Materials:

20.5 mL trioctylphosphine, which I will call TOP

0.52 mL hexamethyldisilathiane, which I will call (TMS)₂S

3.5 mL dimethyl zinc, which I will call Me₂Zn

dry nitrogen line at about two to three psi of pressure; needle attachment

2 dry 20 or 18 gauge cannulae (to be referred to as canula A and canula B)

25 mL glass graduated cylinder

about 10-20 mL acetone for cleaning

about 100 mL bleach for cleaning

about 10 mL tertiary butyl alcohol for cleaning

rubber septum to fit top of graduated cylinder

round-bottom glass storage flask with sidearm

rubber septum to fit top of storage vessel

teflon stopper with vicon o-ring to block sidearm from air

bubbler

plastic syringe body and septum to fit outlet for cleaning

baking dish or other large container for cleaning

sufficient solvent and waste beakers

nitrile gloves

glass stirring rod

one 1 mL disposable syringe and one disposable 20 g needle for $(\text{TMS}_2)\text{S}$ transfer

one 5 mL disposable syringe and one 6 inch 18 or 20 g Luer-lock needle for Me_2Zn

transfer

Directions:

13. Prepare cleaning stations.
 - a. Fill plastic syringe with acetone. Place rubber septum over outlet to prevent leaking. Prepare and label waste beaker for acetone.
 - b. Pour bleach into baking dish. Tilt dish so bleach sits in a narrow pool on one side of it. Place extra, clean gloves inside hood, along with stirring rod and waste bag.
14. Place rubber septa firmly into graduated cylinder and storage flask. Screw teflon stopper into the sidearm and do not close all the way. Attach a tube from the sidearm to the bubbler and Schlenk line.

15. Purge N₂ line with nitrogen, followed by the bottle of TOP and canula A, and then the graduated cylinder and canula B. Purge the storage flask by closing the bubbler, applying vacuum and N₂ three times, and then turning off the N₂ flowing in and opening the bubbler. Place the end of canula B into the septum at the top of the storage flask. Refer back to Figure A-1 for TOP transfer scheme. Push full amount of TOP into graduated cylinder.
16. Remove canula A, move N₂ line to cylinder, clean canula A with acetone by sticking it into the syringe of acetone (through septum) and pushing acetone through it into the waste acetone beaker. Then pull more solvent from clean acetone beaker and repeat twice more.
17. Push 5 mL TOP from cylinder to flask.
18. As soon as open (TMS)₂S desiccator, DO NOT REMOVE HANDS FROM HOOD until initial cleanup is complete. (This material is referred to as “the stinky stuff” for a reason.)
 - a. Open desiccator and baggie.
 - b. Clamp bottle securely, flat on floor of hood.
 - c. Set gently blowing N₂ line over mouth of bottle but not too far in; be sure no splashes occur. Use disposable 1 mL syringe and 20 gauge disposable needle to pull out full amount of (TMS)₂S. Transfer into flask and gently drip material into flask without allowing the liquid to touch the sides.
 - d. Check gloves for splashes. Remove and put in bleach if any are found.

- e. Close bottle, unclamp, replace in baggie and then desiccator.
 - f. Dump needle, syringe, and gloves into bleach container. Put on new gloves. Stir items in bleach until they are good and soaked.
19. Purge Me₂Zn bottle. Purge 5 mL syringe and 6 inch needle with N₂. Draw full amount of Me₂Zn into syringe, transfer to flask, cap Me₂Zn bottle, add Me₂Zn to contents of flask without touching the sides with the liquid. Rinse needle and syringe with tertiary butyl alcohol, then bleach, then acetone.
20. Push the rest of the TOP in to the flask. Remove and rinse canula B with acetone.
21. Switch Schlenk-line to N₂. Remove septum from flask, cap flask securely, close stopper securely, and finally wrap flask in foil to prevent light degradation of the solution.

Synthesizing nanocrystals

Now we get to put the stock solutions together to make nanocrystals using organo-metallic synthesis. The rate of growth is controlled by temperature and monomer density of the stock materials. Nanocrystal formation and growth is a nucleation process and requires a minimum energy to get started, which we provide with a high-temperature growth medium. Our emphasis has been to grow larger, rather than smaller, nanocrystals which fluoresce more to the red. The reason for this has been to be sure the absorption curve of the nanocrystals is accessible to the lasers we have in the lab.

If one simply injects all the core materials at once the nanocrystals grow quickly at first, and then the growth rate slows down due to monomer exhaustion. The dominant

nanocrystal size growth is now dominated by Ostwald ripening, which is a thermodynamic competition between the growth of larger crystals and the dissolution of smaller (less stable) crystals.⁶⁷ To grow bigger, large nanocrystals must cannibalize smaller crystals. This is a slow process. Xudong Fan found that four equal injections of stock solution several minutes apart reduced the growth time of nanocrystals considerably.⁶⁴ I have found an even faster growth method. Instead of a few large injections, I inject one quarter or less of the material quickly, and then inject the rest of the stock solution dropwise with one drop every ten seconds. The total process takes about 20 minutes, while Dr. Fan's process took up to several hours and sometimes required overnight growth with frequent monitoring.

We usually have a particular fluorescence wavelength in mind when we set out to grow a batch of nanocrystals. In order to get close to that value we can change the timing of stock solution injection, change the amount of solvent we grow the crystals in (in this case, trioctylphosphine oxide) in order to change the monomer density, or change the temperature. We can monitor the size of the nanocrystals as they grow using a UV-vis spectrometer, which irradiates the sample in the ultraviolet through visible range and collects the absorption spectrum. (Taking small samples for characterization is called "taking aliquots.") As the crystals grow larger the peak moves to the red. While engaged in experiments with the nanocrystals it is important to remember that absorption and emission are offset by an (approximately) 30 nm Stoke's shift, and photoluminescence will be to the red (longer wavelength side) of absorption.

And now, the recipe.

Materials

either 8 g or 12.5 g trioctylphosphine oxide, which I will call TOPO

1.2 mL CdSe stock solution

2.7 mL ZnS stock solution

lots of dry methanol

lots of syringes and Luer-lock needles

3-arm round-bottom flask

glass-encased stirbar

magnetic stirrer

two glass arms with rubber septa to fit

condenser and Schlenk line adaptor

temperature controller(s) and monitor, with probe

vacuum grease and glassware clips for joints

Bunsen burner

storage tube or flask with sidearm

test tube(s) with lip and septum

centrifuge

16 gauge copper wire

pliers and wirecutters

Directions

1. Start with dry, very clean glassware. It is imperative that the glassware be exceptionally clean. Normally, it will have been washed, soaked in a base bath overnight, rinsed thoroughly, and baked in a hot oven until dry. Set up vacuum trap on the Schlenk line.
2. Smash up TOPO in its jar and measure out 12.5 grams (yields smaller nanocrystals due to less concentrated solution) or 8 grams (yields larger nanocrystals due to more concentrated solution).
3. Set up the following: a 3-arm round-bottom flask (100 mL size is good) in heating mantle with no sand on top of a stirring apparatus, with only one arm (with septum wired to its end, other end greased and clipped to the flask) in. In the middle line hook up a condenser with a connection to the Schlenk line and a bubbler on top; hook up cold water in and out lines. Wire the septum to the second arm but do not grease or clip the end. Set this arm in the third hole in the top of the flask. Clamp the flask and the condenser separately.
4. Degas and remove water vapor by pulling a vacuum, heating all the glassware carefully with a Bunsen burner, and then gently backfilling with nitrogen gas, and repeating. Leave under gently flowing nitrogen. If a clip catches on fire be sure to replace it as the burning will loosen its grip.
5. Insert the temperature probe in the clipped arm, so that it reaches nearly to the bottom of the flask.

6. Remove the unclipped arm and drop in a *glass*-coated magnetic stirbar. (Teflon doesn't stand up to hot TOPO as well as glass.)
7. Make a waxed paper funnel in the open hole side of the flask and very carefully dump in the TOPO. Be sure ahead of time that the nitrogen is flowing slowly enough that the TOPO will not be blown back out, and that it is still flowing quickly enough that the inside of the flask is air-free. Then: grease, insert, and clip the second arm.

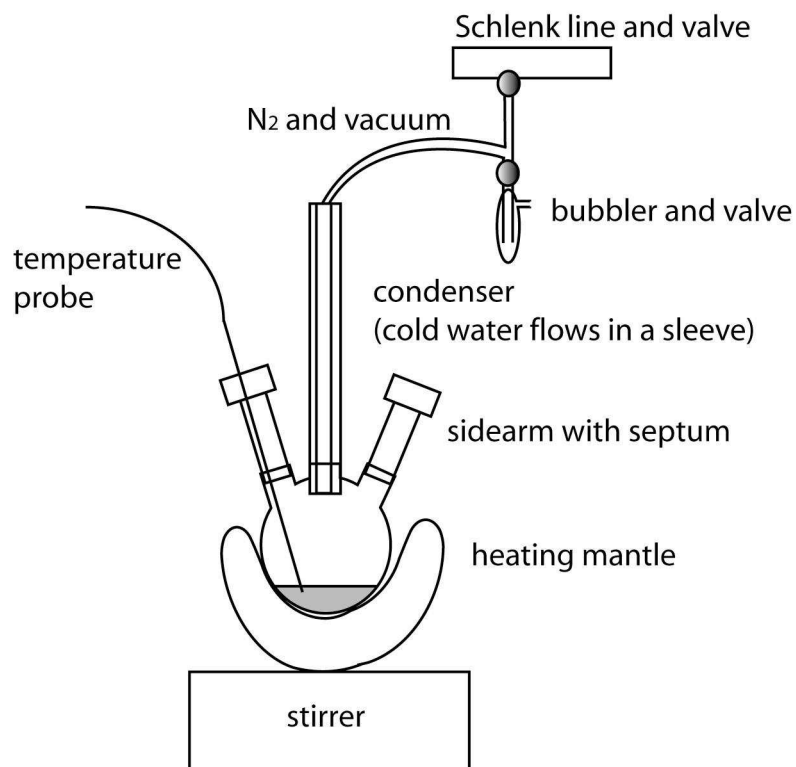


Figure A-2: Schematic of synthesis glassware and other equipment.

8. Plug in the heating mantle and set the power supply for about 210°C (between 50 and 70% of full power, if using a power supply without temperature-setting controls).
9. Turn on stirring. When the temperature is about 30°C, or the TOPO is about half melted, close the bubbler and go to vacuum slowly. There is an option to either pour sand into the heating mantle or not at this point. I have, over time, opted for “not” since I have faster temperature control that way. Be sure the temperature is steady at 210°C and that the vacuum is quiet and most importantly that the liquid is refluxing well. That is, it is boiling and recondensing quickly. If you have to go to a higher temperature for this to happen you may have a vacuum leak. (This is acceptable up to about 250°C.)
10. Let reflux steadily for 1.5 to 2 hours. NOTE: if at any point in this stage the liquid turns yellow, stop everything and clean up. The TOPO has been contaminated by vacuum grease (or something else) and no good nanocrystals will be able to form in it.
11. Prepare rinses ahead of time as they are needed very quickly after the stock solution injections take place. Also purge a Schlenk line to each of the stock solution flasks so that when the stoppers and caps of the storage flasks are opened nitrogen will flow out.
 - a. CdSe rinse: one beaker of tertiary-Butyl alcohol and one beaker of methanol. The last steps are to clean with soap and deionized water and to aspirate needles and cannulae with acetone and dry in a hot oven.

- b. ZnS rinse: one beaker of bleach, one of water, and one of methanol. The final steps are the same as for the CdSe rinse.
12. Apply nitrogen gas slowly, open the bubbler, and turn the temperature controller power up to achieve a temperature of 320°C. Wait for reasonable temperature stability.
 13. Prepare a medium-sized syringe and long Luer-lock needle from the oven. It is sometimes useful to use needle-nosed pliers to screw the needle onto the syringe due to the heat.
 14. Put the CdSe stock solution flask under nitrogen gas by opening the stopcock a bit, and then open the cap so N₂ flows out the top into the hood. Purge the needle and syringe in the flowing nitrogen.
 15. Take 1.2 mL CdSe solution, protect under nitrogen, and push needle through septum on one arm of reaction flask and all the way down to just above the stirring TOPO. Close CdSe storage flask.
 16. For large crystals, inject about one quarter of the material quickly and the rest dropwise for approximately 20 minutes (with about 10 seconds between drops), and perform a very small (several drops worth) fast injection at the very end to tighten the size distribution of the nanocrystals. For smaller crystals, do equi-volume larger injections for a total of one to four injections, depending on how small you are aiming for. The injections should be about five minutes apart. Note that any addition of material lowers the temperature of the solution. After the last injection lower the temperature to 280°C and monitor the size as the crystals

grow over time. If you find at the end of the injections that the crystals are too small, take a small amount of fresh stock solution and inject it dropwise until the size is correct. Track the size by taking aliquots (small samples) with a fresh, hot needle, placing it in a cuvette of tertiary-Butyl alcohol that you have already taken the spectrum of, and take a UV-vis spectrum of the absorption. As the crystals grow larger the absorption peak moves to lower energy (redder absorption).

17. Clean needles and syringes with the CdSe rinse in the order listed above.
18. When ready to cap the crystals, take 2.7 mL ZnS stock solution (similar to CdSe procedure) and inject dropwise over the course of 5 minutes. Clean needle with the materials listed above, and with particular repetition of the water rinse step.
19. Lower the temperature to 100°C (switch to automatic temperature controller if you haven't already), and allow the solution to stir at this temperature 1.5-2 hours in order to let both the interface of the two layers and the core of the crystals anneal.
20. Prepare a 20 mL disposable syringe with 20 mL of dry methanol (be sure it is dry; it is listed on the bottle as anhydrous).
21. Turn heating mantle off, water off, leave nitrogen on, and temperature probe on, and lower heating mantle away.
22. When the temperature reaches 60°C inject the dry methanol. Resupport glassware with stir-base, turn off stirrer. Let all sit and cool until precipitation

takes place; this can take up to 12 hours. Eventually there will be a red-brown precipitate coating the bottom and a clear liquid above it.

23. Prepare a purged storage flask (you might as well do it now) and a purged test tube with a lip and an upside-down septum wired onto it. Make sure the test tube is the same size as the counter-weight test tube in the centrifuge, and that the counter-weight has some mineral oil in to match the mass of the real test tube full of chloroform.
24. Take as much methanol off the nanocrystal aggregate sludge in the reaction flask as possible without stirring up the nanocrystals. Use a large syringe. Discard the methanol.
25. Remove the remaining nanocrystal and methanol slurry from the reaction flask and put it in the test tube (be sure to provide an outlet needle in the septum for displacement of nitrogen gas, and remove it when the liquid nearly fills the tube). This may take several transfers and the tube will certainly fill up before you run out of slurry.
26. Centrifuge the tube two to three minutes at a “reasonable” rpm. There was no gauge on the old centrifuge I used so I do not know how fast the spin rate actually was. Spin until the nanocrystals have compacted into the bottom of the tube and the liquid above is clear.
27. Remove excess methanol from the tube while protecting under N_2 . Put in more slurry from the reaction flask. Repeat centrifuging and methanol removal until

reaction flask is empty, the last of the nanocrystals has been compacted, and the last of the excess methanol has been removed from the test tube.

28. Draw seven to eight mL of dry chloroform (again, it is labeled ‘anhydrous’) from its bottle, inject into the test tube, and swirl until all nanocrystals are in solution. Watch for the last of the compact pellet to disappear from the very bottom of the tube.
29. Remove all liquid from test tube and put it into the storage flask under nitrogen gas. Cap well, wrap in foil to prevent light degradation, and store in a cool place. Nanocrystals stored at room temperature or below survive years provided they are not contaminated by oxygen and not exposed to strong light.

This nanocrystal solution can be checked for size and size distribution using the UV-vis spectrometer, or via the width of its photoluminescence spectrum. (See Chapter Three for more details.) If further size selection is thought necessary in order to reduce the size distribution, reprecipitation with methanol and the subsequent centrifugation and redispersal with chloroform two or three more times is recommended. A competing amount of the two solvents is recommended. (For example, two mL chloroform to four mL methanol.) Smaller crystals stay suspended in the methanol and remaining chloroform longer than large crystals so slightly shorter centrifugation times will allow more small crystals to be removed from the batch.

Lastly, clean the glassware by rinsing with chloroform and then scrubbing with soap and water, and then leave fully submerged in a base bath up to one day (more than 2 hours). Rinse each piece for at least one minute under running tap water and then rinse

three times with deionized water, and then dry them in a hot oven. This will leave the glassware clean enough to use for the next batch of nanocrystals. If you think that too much vacuum grease is getting into the glassware during the cleaning process, rinse the glassware with hexanes after the chloroform rinse. Lint-free tissues also work wonders for removing excess grease.

See Chapter Three for comments on characterization, and Appendix B for nanorod synthesis procedures.

APPENDIX B

NANOROD SYNTHESIS

In this Appendix, nanorod synthesis will be described. Since it is very similar to the synthesis laid out in Appendix A there are many fewer details listed in this section. It is expected that a person choosing to synthesize nanorods will have already familiarized themselves with the nanocrystal procedures. The safety concerns are the same as listed in those procedures.

Ingredients in CdSe nanorod stock solution

6.7 mL TOP

0.18 g Se

0.165 mL Me₂Cd

Synopsis of nanorod synthesis (based on nanocrystal synthesis)

1. Reflux 4.02 g TOPO together with 0.327 g n-Hexylphosphonic acid (temperature will be 210-218 °C under ideal conditions).
2. Raise temperature to 360 °C (I have found 290 °C to also be successful).
3. Add 2 mL CdSe nanorod stock solution quickly.
4. Lower temperature to 290 °C.
5. Add 1.1 mL more CdSe nanorod stock solution (or a different amount depending on desired size) dropwise and slowly.

6. Anneal at this temperature for 30 minutes.
7. Lower temperature to 120 °C.
8. Add 1.04 g n-Hexyldecylamine via a funnel (remove one sidearm septum for this task).
9. Let cook at this temperature for 20 minutes.
10. Raise temperature to 190 °C.
11. Add 7.5 mL ZnS stock solution dropwise and more quickly than the core material (this step takes about five minutes).
12. Lower temperature to 100 °C.
13. Let anneal for a minimum of one hour.
14. The rest of the process is the same as listed above for nanocrystals, except that the solution *must* be washed with MeOH a minimum of twice. If it is insufficiently washed, the nanorods in chloroform will cause any polystyrene they are dispersed in for optical measurements to turn milky white and scatter an unacceptable amount of incident laser light. (It takes one day for the full polymer degradation process to occur.) A further note: after the result of the second wash has been centrifuged but before the extra materials are removed, there may be four layers present: The very top is a very viscous acid layer tinted brown or red with nanorods. Next is a methanol layer, sometimes white and scattering from suspended small particles. Next is chloroform tinted very darkly with nanorods. Lastly, on the bottom, is a soft sludge of very dense nanorods in chloroform. The acid layer must be removed before the methanol layer (using surface tension and

pressing against the inside wall of the tube using a large-bore syringe needle is the best way to do this). The methanol layer is then removed. The two bottom layers may stay. When mixed, sometimes a little bit of extra separation occurs. In this case use the bottom layer.